ALICE TPC Upgrade Activities for LHC Run 3 and Beyond: ”SAMPA ASIC Tests with GEM Detector Prototype”

Kristian P. Engeseth

Master Thesis

Department of Physics and Technology
University of Bergen

September 2015

Abstract

The Time Projection Chamber (TPC) signal readout of the ALICE detector is being upgraded to accommodate the higher collision rates and -energies during LHC Run 3 in 2018. Due to the increased collision rates, the TPC drift time of about 100 µs will be 5 times longer than the average time between interactions, rendering the presently employed gating of the TPC wire-chambers insufficient. Therefore, a Gas Electron Multiplier (GEM) based system will be replacing the wire-chambers. In addition, the front-end electronics need to be replaced to match the new readout chamber technology and increased data rates. This will be done by the new SAMPA chip which combines the functionality of the previous PASA (PreAmplifier ShAper) and ALTRO (ALICE TPC ReadOut) chips currently used as front-end electronics.

The focus of this work has been twofold: (1) Characterizing a SAMPA Chip 1 analog prototype for use in the upgraded ALICE TPC signal readout. (2) Construct and characterize a GEM detector prototype for use with the SAMPA Chip 1.

A fully differential buffer has been designed and mounted on the Chip 1 carrier board for ADC readout capabilities. The buffer performed well and the ADC readout was successful.

The power consumption of the SAMPA Chip 1 failed to reach the requirement of 6 mW per channel, achieving no better than ~9 mW per channel at the nominal supply voltage. Results from the gain and pulse shape stability showed linear gain and a stable pulse shape, with some deviations for low and high input charges as a result of poor signal-to-noise ratio and the amplifier saturating, respectively. The crosstalk measurement showed scattered results, but none of the carrier boards achieved the requirement of less than 0.2 %. The best crosstalk results averaged ~0.3 %, while the worst exceeded 1 %. Simulated noise for the SAMPA Chip 1 doesn't fulfill the requirement of 385 ENC at 12 pF capacitance. When corrected for stray capacitances on the carrier boards, the measured noise coincided to some extent with the simulated values. The high noise levels seem to originate from the inside the SAMPA ASIC.

A GEM detector has been designed and produced in close collaboration with the group stationed at the Wigner Research Institute in Budapest, Hungary. Testing of the GEM detector has been done at the Wigner Institute using both Fe-55 and Sr-90 radioactive sources, measuring the energy resolution of the detector and calibrating its gain. The gain was set to ~2000 and the energy resolution was measured to be ~8 %, which is below the 12 % requirement.

Further testing of the prototype detector has been conducted in Bergen, establishing its gain for different gas mixtures and measuring the signal-to-noise ratio of

the SAMPA Chip 1 for MIPs. This work has been done in close collaboration with Ganesh Jagannath Tambave, whose main focus has been on the signal readout and data acquisition of the SAMPA Chip 1. The signal-to-noise ratio measured to be 27:1, the requirement being 38:1. Increasing the drift gap of the detector will increase the signal-to-noise ratio.

Acknowledgement

The work of this thesis has been carried out within the Microelectronics group at the Department of Physics and Technology at the University of Bergen from August 2014 through September 2015.

I would like to thank my supervisors Kjetil Ullaland and professor Dieter Röhrich for guidance and support throughout this work.

A great thanks goes to professor Dezsö Varga for letting me come to Budapest and conduct tests in his lab at the Wigner Institute. Thanks also to the SAMPA design team in Sao Paulo, Brazil.

Further I would like to thank Ganesh Jagannath Tambave for excellent counsel and teamwork during measurements and other practical work.

A special thanks goes to my father Svein-Atle Engeseth for first-class help with the analog electronics part of my work.

Thanks to Arild Velure for providing invaluable documents and insight regarding the inner workings of the hardware used in my thesis. Thanks also to my fellow student Mads Risberg for creating an inspiring working environment and helpful discussions.

Bergen, September 2015

Kristian P. Engeseth

Contents

Abstract **i**

Acknowledgement **iii**

Acronyms **vii**

1 Introduction **1**
1.1 Large Hadron Collider (LHC) . . . 1
1.2 ALICE Experiment . . . 4
1.3 ALICE TPC Upgrade . . . 5
1.4 Upgraded ALICE TPC Readout System . . . 5
1.5 Primary Objective . . . 6
1.6 Outline . . . 7
1.7 About this Work . . . 7

2 SAMPA ASIC **9**
2.1 ALICE TPC Requirements - SAMPA Chip . . . 9
2.2 SAMPA Schematic . . . 11
2.3 SAMPA Carrier Board and Buffer Design . . . 12
2.3.1 Buffer Design Parameters . . . 12
2.3.2 Buffer Design . . . 13
2.3.3 SAMPA Carrier Board . . . 15

3 GEM Detectors **19**
3.1 What is a GEM Detector? . . . 19
3.2 Constituents . . . 20
3.3 Main Physical Processes . . . 21
3.3.1 Photoelectric Effect . . . 22
3.3.2 Inelastic Scattering From Atomic Electrons . . . 23
3.3.3 The Bethe-Bloch formula . . . 23
3.3.4 Electron Avalanche . . . 24
3.4 Gain . . . 24
3.5 Function . . . 26
3.6 Gas Choice . . . 27
3.6.1 Noble gases . . . 27

3.6.2 Quenchers . . . 27
3.7 Discharges . . . 28
3.7.1 Discharge Testing . . . 28
3.8 GEM Prototype Chamber [$10 \times 10\ cm^2$] . . . 30
3.8.1 Enclosure . . . 31
3.8.2 Anode Plane . . . 31
3.8.3 Resistor Chain . . . 32
3.8.4 Measurements . . . 37

4 SAMPA Tests **41**
4.1 Pulse Shape Generator . . . 43
4.1.1 Power Consumption . . . 43
4.1.2 Gain and Pulse Shape Stability . . . 45
4.1.3 Crosstalk . . . 50
4.1.4 Noise . . . 54
4.2 SAMPA Tests With GEM Detector Prototype . . . 60
4.2.1 Gain Calibration Using Fe-55 . . . 60
4.2.2 Energy Resolution Using Fe-55 . . . 61
4.2.3 Signal-To-Noise Ratio Using Sr-90 . . . 64
4.3 Conclusion . . . 69

5 Summary and Conclusion **71**

A Pulse Shape Stability **73**

B Noise in Charge-Sensitive Preamplifiers **77**

C DAQ Settings for the Discrete Component Preamplifier **79**

D Crosstalk Results **81**

E Schematic and PCB Design **89**

F Number of Primary Ionizations in Ne-CO_2-N_2 (90-10-5) **95**

G Pulse Area Calculation **97**

Acronyms

ADC Analog-to-Digital Converter

ALICE A Large Ion Collider Experiment

ALTRO ALICE TPC ReadOut

CRU Common Readout Unit

FEC Front End Card

FEE Front End Electronics

GBT GigaBit Transceiver

GEM Gas Electron Multiplier

IC Integrated Circuit

LHC Large Hadron Collider

MIP Minimum Ionizing Particle

MPW Multi Project Wafer

NCB New Carrier Board

OCB Old Carrier Board

PASA PreAmplifier ShAper

SNR Signal-to-Noise Ratio

VI Virtual Instrument

Chapter 1

Introduction

Particle accelerators are used to recreate conditions similar to those of the very early universe. They do this by colliding particles at very high energies to explode them into their subatomic constituents, which are detected using different types of detectors. The Large Hadron Collider (LHC) is an example of one such particle accelerator.

1.1 Large Hadron Collider (LHC)

The Big Bang theory explains the history and future of the universe. It is a scientific model which helps to explain how the universe was developed over time. The figure 1.1 shows the history and expansion of the universe as we think it occurred, with the Big Bang happening at time zero and the universe as we know it today 13.8 billion years later. Initially the universe was very hot (10^{32} Kelvin) and no particles existed, but over time it started to cool down as well as expand, and the sub-atomic particles were created. To understand the different phases of the evolution of the universe the Large Hadron Collider (LHC) has been built. In particular, two phases indicated in figure 1.1 at times 10^{-10} s and 10^{-4} s are being recreated by colliding very high energetic (TeV) proton-proton and heavy ion (Pb) beams, respectively.

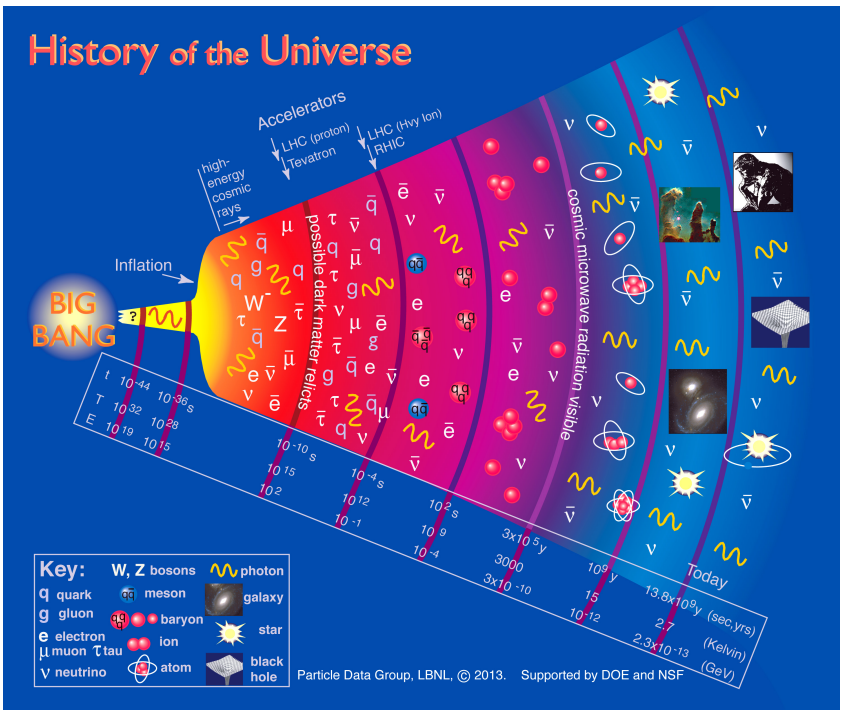

Figure 1.1: Evolution of the universe after the Big Bang. Using particle accelerators, we can recreate conditions similar to those of the very earliest moments of the universe [9].

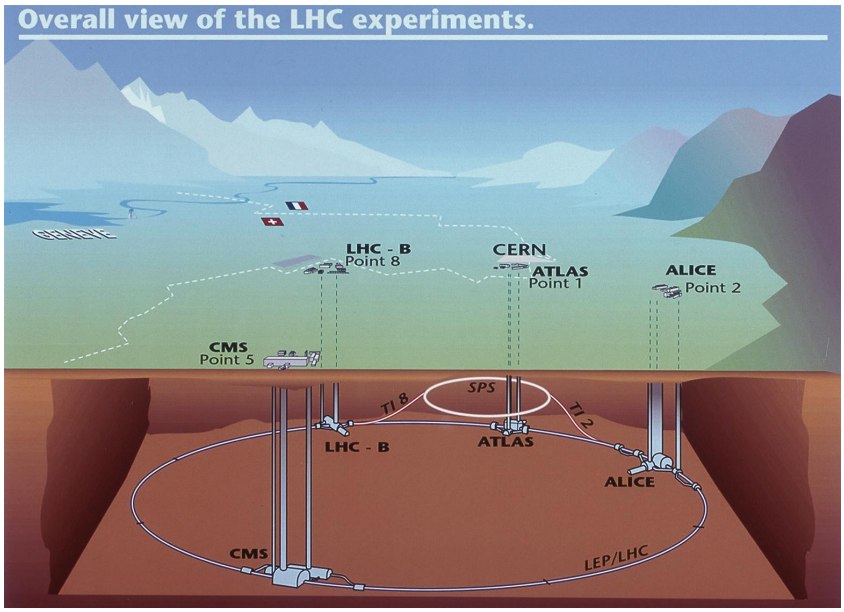

Figure 1.2: A picture showing the LHC and the four main experiments which take place along the collider. [4]

The Large Hadron Collider (LHC) is the world's largest and most powerful particle accelerator, achieving center-of-mass energies of 13 TeV (protons and heavy ions, e.g. Pb). It was built by the European Organization for Nuclear Research (CERN) from 1998 to 2008. As the name suggests, it is a large collider of hadrons (particles made up of quarks). The LHC itself is a massive machine that lies in a 27 km long circular tunnel roughly 100 meters below ground at the French-Swiss border. Inside the tunnel there are two parallel beam lines which intersect at four locations. Particles are accelerated in opposite directions inside the beam lines and are steered to collide at these points. Four experiments take place at these intersections, ATLAS[1], ALICE[2], CMS[3] and LHCb[4]. Figure 1.2 shows the experiments and their location along the LHC. This thesis is mainly focused on the upgrade activity of the ALICE Experiment for 2018 which is discussed in the following section.

[1] A Toroidal LHC Apparatus
[2] A Large Ion Collider Experiment
[3] Compact Muon Solenoid
[4] Large Hardron Collider beauty

1.2 ALICE Experiment

ALICE (A Large Ion Collider Experiment) at the LHC studies high-energy heavy-ion experiments (Pb-Pb nuclei). The goal of the experiment is to characterize strongly interacting matter at extreme energy densities. In this manner one can recreate the phase of the early universe as proposed in the theory of The Big Bang, as discussed in the previous section. These energy densities are expected to be high enough to produce a Quark-Gluon Plasma[5] (QGP).

During the Pb-Pb collisions various types of particles are created, and to detect and characterize them, ALICE employs a huge detector system which is shown in figure 1.3. The Inner Tracking System (IPS) is the detector closest to the beam-pipe and detects the decay of short-lived heavy particles. It consists of six cylindrical layers of silicon detectors using three different detector technologies. Surrounding the ITS is the Time Projection Chamber (TPC) which is the main tracking detector in ALICE. It consists of a large circular gas volume (90 m^3) divided in two by a 100 kV central electrode. The end caps are equipped with MultiWire Proportional Chambers (MWPCs) which are used to record the trajectories of particles traversing the detector. This gives a 3 dimensional image of the particle's trajectory. In LHC Run 3 the MWPCs will be replaced by GEMs. The Transition Radiation Detector (TRD) is located outside the TPC. It is used to detect electrons and positrons using transition radiation, which is X-rays that are emitted when the particles traverse many layers of thin materials. The Time-Of-Flight (TOF) detector calculates the velocity of a charged particle by measuring the flight time over a given distance of the particle's trajectory. The mass of the particle can then be calculated given that its momentum is known. There are several other detectors, such as EMCAL and PHOS for photon detection, Muon filters etc. There are also solenoid and dipole magnets used to bend the trajectory of the high energetic charged particles inside the detector.

In 2010-2011, ALICE has performed Pb-Pb ion collisions at center-of-mass energy of 2.76 TeV per nucleon pair and integrated luminosity[6] (L_{int}) of 0.16 nb^{-1}. To increase the luminosity (collect more data, and therefore achieve better statistics), some subdetector systems (TPC, Muon etc.) of the ALICE experiment will be upgraded in two phases, namely Run 2 and Run 3, after the two long shutdowns of the LHC in 2015 and 2018, respectively. Run 2 and Run 3 aim to reach L_{int} of 1 nb^{-1} and 10 nb^{-1}, respectively. The Run 2 has started in June 2015 and the world's highest collision energies for proton-proton beams have been achieved (6.5 Tev per beam). The heavy-ion collisions at these record energies are planned to start in December 2015.

[5] A deconfined phase of matter in which the strongly interacting quarks and gluons no longer are confined inside hadrons[12].

[6] Luminosity is the ratio of the events detected (N) in a certain time (t) to the interaction cross-section (σ). The unit is barn [b] and is defined as $10^{-28}m^2$.

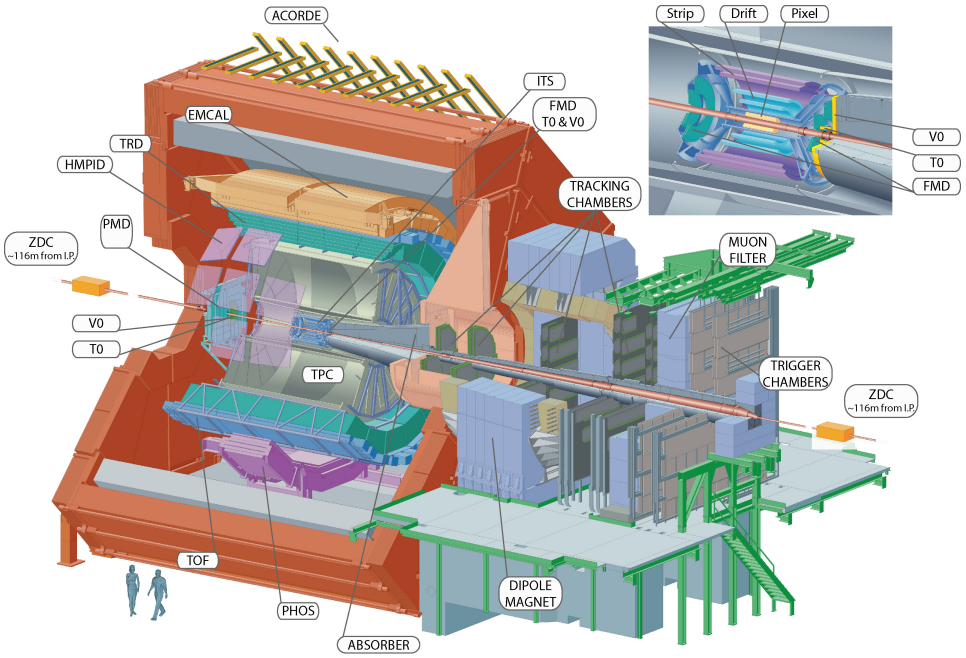

Figure 1.3: A schematic view of the ALICE experiment [1].

1.3 ALICE TPC Upgrade

To achieve high luminosity during LHC Run 3, the Pb-Pb collision rate is expected to be 50 kHz (compared to 3.5 kHz in Run 1 and Run 2). To cope with this high collision rate, the present ALICE TPC and its readout system need to be upgraded. In this context, the present Multi-Wire Proportional Chamber based TPC (Time Projection Chamber) will be replaced with a GEM (Gas Electron Multiplier) based TPC. The GEM based readout chambers are proven technology for operation in high-rate environments. Moreover, the Front-End Electronics (FEEs) and the readout system will also be replaced from the present triggered readout to continuous readout. The upgraded GEM based TPC with continuous readout will match the expected increased data-rates (1 TByte/s) for Run 3.

1.4 Upgraded ALICE TPC Readout System

The signal readout system of the ALICE TPC will be upgraded to continuous readout (no hardware trigger) before LHC Run 3 in 2018. In the continuous TPC readout, the signals from the GEM detector pads will be processed using the Front-End Cards (FECs), see figure 1.4. On the FECs five custom-made SAMPA ASICs will process the data from their 160 readout channels (32 channels each). The SAMPA contains most of the Front-End Electronics such as a charge-sensitive preamplifier, shaper, 10 bit 10 MHz digitizer and digital signal processing part. The data from the SAMPA will then be multiplexed and transmitted using GigaBit Transceivers (GBT) via optical links to a Common Readout Unit (CRU). The CRU is an interface to the online

computer farm and the trigger and detector control system. In the ALICE TPC upgrade there will be 3400 FECs, each containing 5 SAMPA ASICS. Each SAMPA has 32 channels, giving the FECs a total of ~500.000 channels. All this data is sent to the CRU at a rate of 1 TB/second. The first version of the SAMPA chip has been produced in 2014.

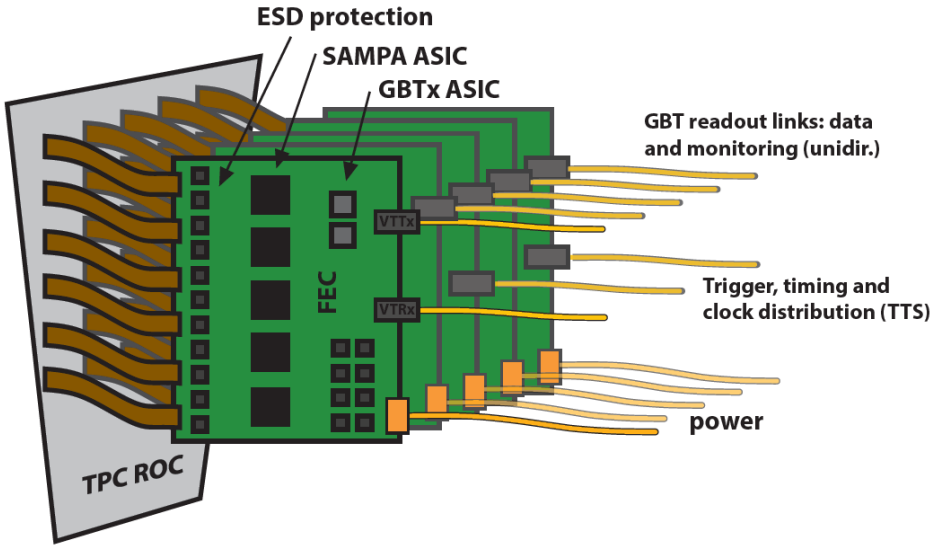

Figure 1.4: The location of the Front End Cards (FECs) in relation to the TPC Readout Chamber (ROC). The SAMPA ASICs are located behind the ESD protection[11].

1.5 Primary Objective

The main purpose of this thesis has been to characterize the analog part of the SAMPA chip which is to be used for signal readout in the upgraded ALICE Time Projection Chamber (TPC) during Run 3 of the LHC in 2018. A preliminary prototype of the SAMPA ASIC has been produced in 2014 on a Multi Project Wafer[7] (MPW) and is currently in the test-phase. The analog part of the SAMPA is called Chip 1, and its characterization, including power consumption, pulse shape stability, crosstalk and noise performance, will be performed in this thesis. These results are presented in chapter 4.

The particle detection of the ALICE TPC will also be upgraded to a Gas Electron Multiplier (GEM) based system which is to be used in conjunction with the SAMPA ASIC. To be able to test the SAMPA Chip 1 under similar conditions to which it will face in the ALICE TPC, a GEM detector is needed. A focus of this thesis has therefore been to design and construct a GEM detector prototype for Chip 1 testing using real

[7] Because Integrated Circuit (IC) fabrication is extremely expensive Multi Project Wafer services are offered in which a number of different IC designs from various teams are incorporated on the same silicon wafer to reduce costs.

GEM signals. This work has been done in collaboration with the Hungarian research group stationed at the Wigner Institute in Budapest, and the results are presented in section 3.8.

1.6 Outline

This thesis is divided into five chapters, including the current one. Chapter 2 gives a brief introduction to the SAMPA ASIC and continues with the design and construction of a differential buffer which is needed for signal readout using an ADC. Chapter 3 introduces GEM detectors and explains the main physical processes which lead to the signal detection. It also reviews the construction of the GEM detector prototype and the calculations needed for the resistor chain. A few measurements of the prototype chamber conducted in Budapest conclude the chapter. In chapter 4 the SAMPA Chip 1 test results are presented for signals created using both a pulse shape generator and the GEM detector prototype. Lastly, the thesis is summarized and concluded in chapter 5.

1.7 About this Work

During the early stages of my work, I was fortunate enough to be invited by professor Dezsö Varga to visit the Wigner Institute in Budapest, Hungary. When I arrived in Budapest I assisted the Hungarian research group in the construction of a prototype GEM detector. Together we constructed the first version, but a flaw in the spacers separating the GEM foils spoiled the performance of the detector. Therefore a set of new spacers had to be designed and implemented. High voltage tests confirmed that the second version performed flawlessly. Before bringing the prototype detector to Norway, I designed and constructed a resistor chain which enabled the detector to be powered from a single high voltage power supply.

When the SAMPA chip arrived from production at CERN, testing of the prototype detector could be done in conjunction with the Chip 1. This work was done in close collaboration with Ganesh Jagannath Tambave, whose main focus was on signal readout and data acquisition using an ADC. Oscilloscope measurements confirmed that the prototype GEM detector worked well when connected to the SAMPA Chip 1.

I also designed a fully differential buffer to accommodate ADC readout, since the SAMPA Chip 1 couldn't drive the 50 Ω load of the ADC. The PCB design of the buffer's carrier board put emphasis on improving crosstalk and noise performance, since these were known to be poor. A challenging practical task was to solder the very small SOT-23 IC packages to the carrier boards. Fortunately, the use of soldering flux and excellent equipment made the task manageable. Tests confirmed that the SAMPA Chip 1 worked well when connected to the ADC through the buffer.

Chapter 2

SAMPA ASIC

The increased collision rates and -energies during LHC Run 3 in 2018 require the signal readout of the ALICE Time Projection Chamber (TPC) to be upgraded. Since the expected interaction rates for Run 3 are ~50 kHz for Pb-Pb collisions, the TPC drift time of about 100 µs will be 5 times longer than the average time between interactions[11]. Therefore, the presently employed TPC wire-chambers will be replaced by Gas Electron Multipliers (GEMs). In addition, the front-end electronics (FEEs), currently consisting of the PASA (PreAmplifier ShAper) and ALTRO (ALICE TPC ReadOut) chips, will be replaced by the new SAMPA ASIC (Application Specific Integrated Circuit) to match the new readout chamber technology and increased data rates.

The upgrade to the SAMPA ASIC will go in two steps, MPW1 and MPW2. The MPW1 consists of three prototype chips meant for concept testing. They only have a few channels each (1-5) and are meant for test purposes to improve the SAMPA chip produced on MPW2, which will have 32 channels and incorporate all electronic components (preamplifier, ADC and digital signal processing). Listed below are the three prototype chips which combined make up MPW1.

- Chip 1: Analog chip (preamplifier, shaper and bias), 5 channels.
- Chip 2: ADC and SLVS (Scalable Low-Voltage Signaling), 1 channel.
- Chip 3: Combination of Chip 1 and Chip 2 and digital signal processing (DSP) capabilities/filters, 3 channels.

2.1 ALICE TPC Requirements - SAMPA Chip

The ALICE TPC requirements for the SAMPA chip are documented in the Technical Design Report (TDR) of the ALICE TPC upgrade and are listed in table 2.1[11]. This thesis focuses on the characterization of the analog part of the SAMPA chip (Chip 1), which corresponds to PASA (PreAmplifier/ShAper). The parameters measured in this thesis are power consumption, noise, Signal-to-Noise Ratio (S:N / SNR), and

crosstalk. A few additional tests will also be done to check for pulse shape stability and gain linearity.

		RUN 1 (measured)	RUN 3 (requirement)
Signal polarity		Pos	Neg
Detector capacitance (range)	(pF)	12 - 33.5	12 - 33.5
S:N ratio for MIPs (IROC)		14:1	20:1
(OROC 6 x 10 mm^2 pads)		20:1	30:1
(OROC 6 x 15 mm^2 pads)		28:1	30:1
MIP signal	(fC)	1.5 – 3	2.1 – 3.2
System noise (at 18.5 pF, incl. ADC)		670 e	670 e
PASA conversion gain (at 18 pF)	(mV/fC)	12.74	20 (30)
PASA return to baseline	(ns)	< 550	< 500
PASA average baseline value	(mV)	100	100
PASA channel-to-channel baseline variation	(mV)	18	18
PASA shaping order		4	4
PASA peaking time	(ns)	160	160 (80)
PASA crosstalk		< 0.1 %	< 0.2 %
PASA integrated non-linearity		0.2 %	< 1 %
ENC (PASA only, at 12 pF)		385 e	385 e
ADC voltage range (differential)	(V)	2	2
ADC linear range (differential)	(fC)	160	100 (67)
ADC number of bits		10	10
ADC sampling rate	(MHz)	10 (2.5, 5, 20)	10 (20)
Power consumption (analog & digital)	(mW/ch)	35	< 35

Table 2.1: The ALICE TPC requirements for the SAMPA chip during Run 3. The measured results come from the PASA chip used during Run 1.

2.2 SAMPA Schematic

A schematic view of the SAMPA ASIC is shown in figure 2.1. Each channel of the SAMPA consists of a Charge Sensitive Amplifier (CSA), signal shaping circuitry, ADC and DSP. The CSA amplifies the charge at the input and transforms it into a differential semi-Gaussian voltage signal. The SAMPA chip will be used for the upgraded TPC as well as for the muon chamber. Therefore, it features a positive (TPC) and negative (muon chamber) polarity option which enables it to amplify both type of signals. For TPC usage, the sensitivity can be set to either 20 or 30 mV/fC, while it is set to 4 mV/fC for muon chamber usage. The shaping circuitry aims to modify the pulse shapes coming from the preamplifier to give them a constant peaking time and pulse width by reducing the long tail of the signals. The pulse shapes coming from the shaping circuitry will have peaking times of 160 ns for TPC settings, and 300 ns for muon chambers, giving nearly the same pulse width of 500 ns for both detectors. Combined with the preamplifier, the shaping circuitry is called PASA (PreAmplifier/ShAper), a name reused from the chip used in Run 1 and 2.

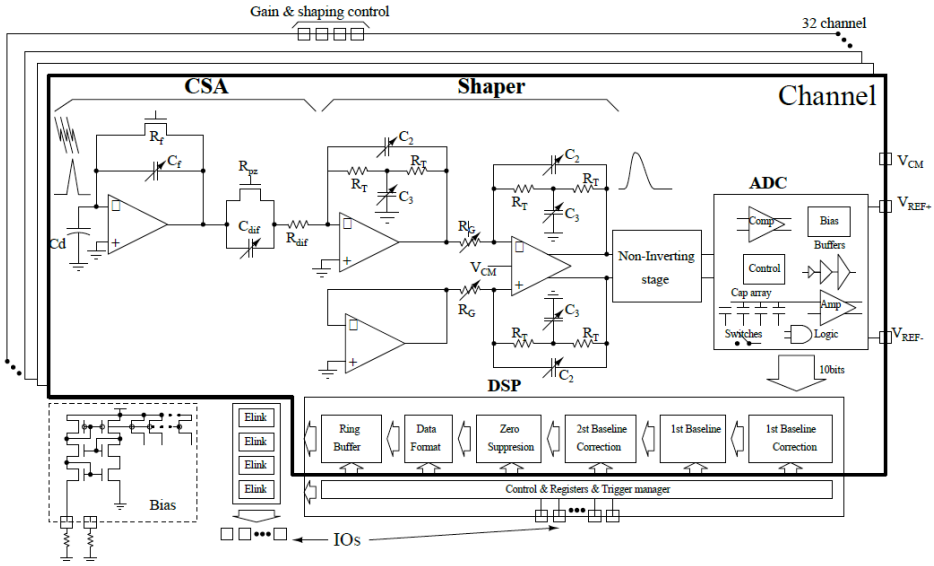

Figure 2.1: Block diagram of the SAMPA ASIC. Each channel (32 total) consists of a Charge Sensitive Amplifier (CSA), signal shaping circuitry, an Analog-to-Digital Converter (ADC) and a Digital Signal Processing (DSP) chain[11].

The ADC has 10 MHz sampling rate, 10 bit resolution and a dynamic range of 1.2 V. After digitization, a pipelined data processor removes a wide range of perturbations on the input signal related to non-ideal detector behavior, such as temperature variations of the electronics and noise. The signal is then compressed using zero-suppression; all data points below a programmable threshold are removed, except a specific number of samples around each peak. Four 320 Mb/s serial links conduct the data read-out continuously at a speed of up to 1.28 Gbps. Without data compression, the 552,900 readout channels of the GEM TPC would produce data at a rate of 7 TByte/s [11]. After compression the data rate will be 1 TByte/s.

2.3 SAMPA Carrier Board and Buffer Design

The data sheet of the SAMPA chip states that it is not designed for 50 Ω termination. Unfortunately the CAEN ADC we use for signal readout is 50 Ω terminated. Therefore a buffer was needed to shield the output of the SAMPA Chip 1 from the heavy load of the ADC.

Before the buffer design began, a little test was conducted to see how the SAMPA Chip 1 behaved while driving different loads. An input signal was injected into the chip and the output was connected to the oscilloscope with the input impedance set to 1 MΩ. Then the input impedance was changed to 50 Ω and the pulse shapes were inspected for any change. Figure 2.2 shows two screenshots, one with 1 MΩ termination (left) and one with 50 Ω (right). As expected the output signal was attenuated when driving 50 Ω. Notice the different voltage division scales which accentuates just how significant the attenuation is. As can be seen the negative channel suffers more attenuation than the positive one.

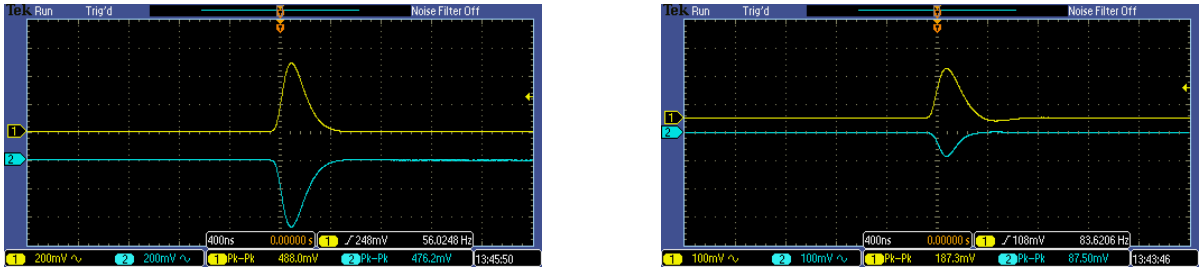

(a) (b)

Figure 2.2: The differential outputs of the SAMPA Chip 1 with 1 MΩ termination (a) and 50 Ω termination (b). The chip is not designed for 50 Ω termination which is clearly visible from the attenuated signal in (b).

2.3.1 Buffer Design Parameters

In order to efficiently shield the SAMPA Chip 1 from the ADC and not interfere with the signals generated by it, the buffer had the following design constraints:

- Low noise: Although the buffer is located behind the SAMPA chip, and therefore the buffer noise referred to the input of the SAMPA chip is lower by a factor of the gain of the SAMPA, it is always preferable to have the buffer interfere with the signal as little as possible.
- Must have both a differential input and output (fully differential).
- Must be able to drive a 50 ohm load.
- Must have minimum ± 1 V output swing.

Power consumption was not an issue since the buffer was only there for test purposes.

2.3.2 Buffer Design

A number of buffer designs were attempted using Veroboards and hole-mounted components, but none of them proved successful as they increased the total noise of the system too much. It was especially the interface between the two cards (the SAMPA PCB and the buffer card) that proved to be faulty, as the wires connecting them picked up a lot of ambient noise, even when placed inside the Faraday cage. Therefore it was decided to design a whole new PCB for the SAMPA chip with an embedded buffer using short leads and only surface mount devices[1]. In addition, the previous design of the SAMPA PCB was not particularly well implemented when it came to noise and cross-talk considerations, so the new design took emphasis on improving the PCB layout by shortening and separating neighboring leads.

A schematic view of the buffer design is shown in figure 2.3a. It uses a THS4503 fully differential amplifier which is unity gain stable and is designed to drive high speed data acquisition systems. Even though the schematic shows the use of a different amplifier (LMH6552), the one used in the final design was the THS4503. This could be done since the two amplifiers have the same footprint and pin configuration. The gain is set by the ratios of RF1/RG1 and RF2/RG2. CF1 and CF2 eliminate overshoot which was visible on the output during simulations of fast input signals. C_BUF_CM is a filtering capacitor for the output common mode voltage. The common mode setting pin (Pin 2) could have simply been shorted to ground, but having a component there makes the design more flexible by enabling the user to select a different common mode output voltage if desired. R20, R21 and C_BUF_LP provide a lowpass filter for the output of the buffer. This is done to reduce noise by filtering away any signals with a frequency greater than the bandwidth of the ADC. The values of 10 Ωand 1 pF are just examples, correct values were calculated later and used in the final design. Decoupling capacitors are not shown in the schematic since they make it look chaotic, but they are visible in the PCB layout picture (figure 2.3b).

The layout (PCB design) of the buffer can be found in figure 2.3b. It shows how the components are placed on the PCB and where the connecting wires go. As can be seen, the components are placed quite close to each other to decrease noise pick up and save space. Placing the components too close, however, makes it quite difficult to route the wires as there is very little space left for them to occupy. The red wires run on top of the PCB while blue ones run on the bottom. Vias provide connections between the top and bottom layers, and are visible as green circles in the figure. In addition to the components shown in the schematic (figure 2.3a), the decoupling capacitors (C40, C41, C50 and C51) are also visible. Notice how close the decoupling capacitors are to the amplifier. This is done as per recommendations of the amplifier's data sheet as it helps increase stability and reduce noise.

[1] Surface mount devices are electronic components (e.g. ICs, resistors and capacitors) which are mounted on the surface of a PCB instead of having legs that go through holes in the PCB, which is the case for hole mounted devices. This enables the components to be smaller and have better characteristics (e.g. lower noise and less parasitic capacitance).

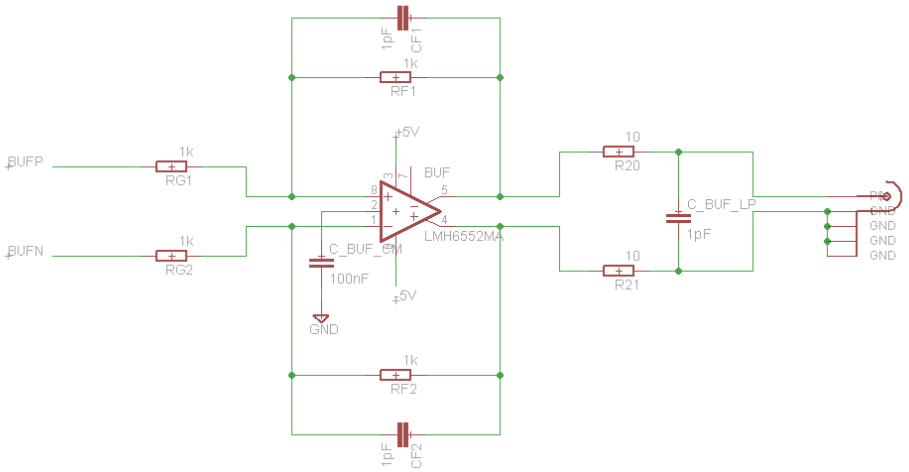

(a)

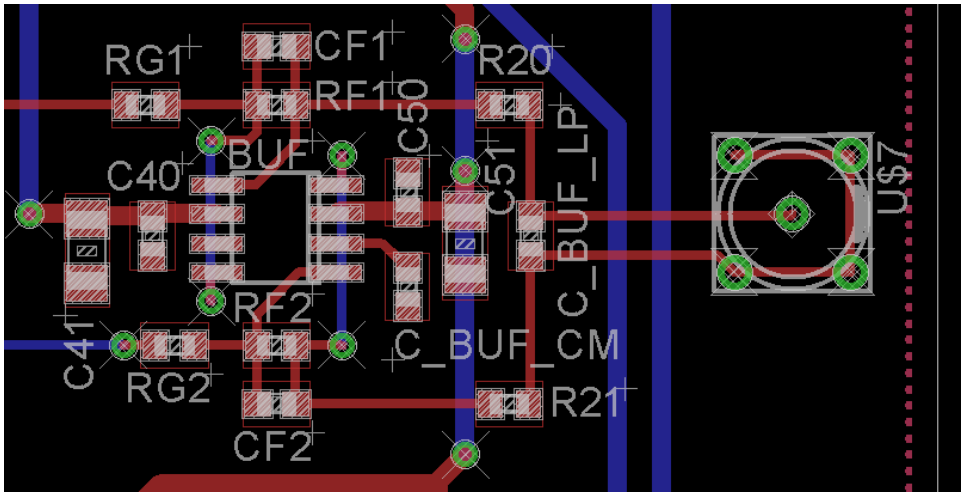

(b)

Figure 2.3: (a) The schematic of the buffer design. (b) The PCB layout of the buffer design. The complete schematic and PCB layout can be found in appendix E.

2.3.3 SAMPA Carrier Board

Four samples of the SAMPA Chip 1 (preamplifier and shaper) were available for testing. Two were mounted on the original carrier board which came from CERN, and two on the new PCB design with the embedded buffer. For convenience, the two original carrier boards will be referred to as "OCB1" ("Old Carrier Board"[2]) and "OCB2", while the two new designs featuring the embedded buffer will be referred to as "NCB1" ("New Carrier Board") and "NCB2". OCB1 and NCB1 are depicted in figures 2.4a and 2.4b, respectively.

In the old design (a) there are two power inputs, +5 V and V_{DD}. The SAMPA chip uses V_{DD} while the +5 V input is used to create three reference voltages, 450 mV, 600 mV and 750 mV. The reference voltages are controlled by the potentiometers at the top of the PCB. Three test pads located around the two black ICs (Integrated Circuits) below the potentiometers give easy access to measure the reference voltages while adjusting them. The input consists of the five bottom LEMO connectors on the left edge of the board, the two above are not used. The output is differential and has one positive and negative pin for each channel. Gain and rise time are selected according to table 2.2 by placing jumpers across the pins at the bottom of the PCB. The "ctrl inj" jumper is related to the two topmost LEMO connectors and is redundant. The configuration shown in the figure gives low gain (20 mV/fC) and 160 ns rise time. At the center of the PCB sits the SAMPA chip. A piece of kapton tape was placed across it to prevent the lid of the IC casing from falling off.

Configuration	**Jumper Label**						
	ctrl inj	cts 0	cts 1	cg 0	cg 1	cg 2	pol
30 mV/fC @ 160 ns, Neg	C	NC	C	C	C	C	NC
20 mV/fC @ 160 ns, Neg	C	NC	C	NC	C	C	NC
4 mV/fC @ 300 ns, Pos	C	NC	NC	C	C	NC	C

Table 2.2: Jumper settings for selecting gain and rise-time of the SAMPA Chip 1. The jumper labels are seen at the bottom of figure 2.4b.

[2] The term "Carrier Board" refers to a Printed Circuit Board (PCB) to which electronic components have been attached (e.g. soldered).

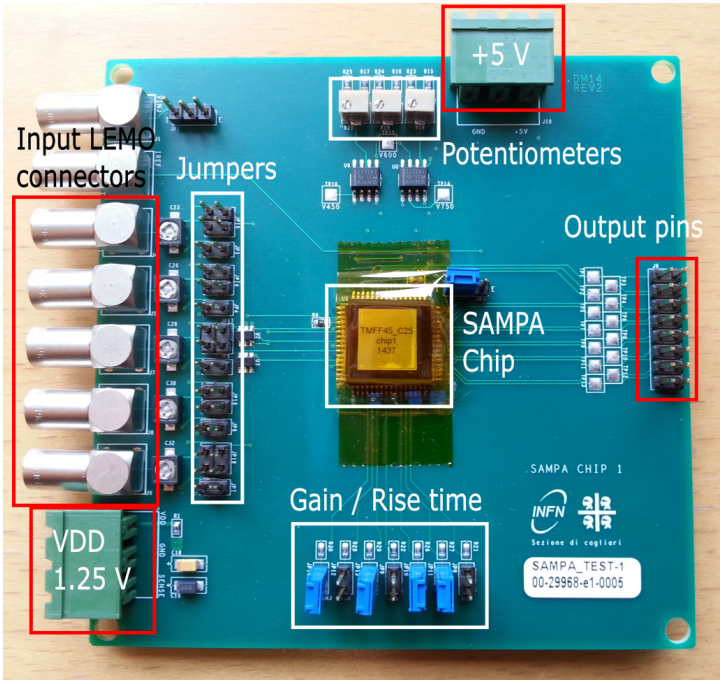

(a) OCB

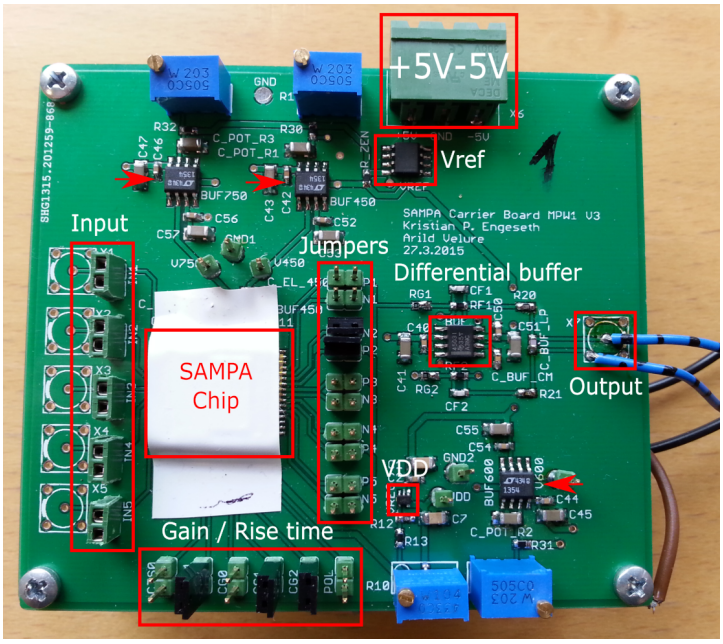

(b) NCB

Figure 2.4: (a) The Old Carrier Board (OCB) for the SAMPA Chip 1. (b) The New Carrier Board (NCB) for the SAMPA Chip 1.

The new design (b) does not feature two separate power inputs. Instead all operating voltages are made on-chip from a $\pm 5\ V$ power supply using voltage references and buffers. Vref is a 1.235 V reference voltage created from the +5 V power supply by a LM285DR voltage reference. Voltage dividers and buffers (LT1354) create the three reference voltages (400 mV, 600 mV and 750 mV) from Vref. The locations of the buffers are marked by the red arrows. V_{DD} is made from a voltage reference (TPS71701DCKR) which is located above the blue potentiometers at the bottom of the PCB (red square). The four blue potentiometers adjust the three reference voltages as well as V_{DD}. Test pads are located adjacent to the buffers to give easy access to the voltages while calibrating them. The jumpers to the right of the SAMPA chip select which of the five channels go through the differential buffer. This was done to eliminate the need of one buffer per channel, since they were quite expensive. The PCB was designed with flexibility in mind, therefore the input can either be injected through LEMO connectors (which are not mounted on the PCB in the picture) or through pin connectors marked with a red rectangle to the left of the SAMPA chip. As with the old carrier board the gain and rise time settings (table 2.2) are selected using the jumpers at the bottom om the PCB (below the SAMPA Chip 1). Because the two extra LEMO input connectors have been removed in the new design, it does not feature the "ctrl inj" jumper. The configuration shown in the figure gives low gain (20 mV/fC) and 160 ns rise time. Strips of tape were placed over the SAMPA chips to hinder the lid of the IC cover from falling off.

The ADC we use for signal readout comes with single-ended inputs from the factory. However, the user manual describes a procedure where one can modify them to become differential. Since this was possible, the output of the buffer in the new PCB design was designed to be differential so it would match the ADC input. This could be done since LEMO connectors can be used as differential signal carriers by connecting one of the signals to the inner wire and the other one to the shielding wire mesh (which is connected to ground if single-ended signals are used). Unfortunately, the modifications to make the ADC inputs differential proved unsuccessful, and single-ended signals had to be used instead. This had not been taken into account while designing the new PCB design, therefore, the new design does not incorporate single-ended output connectors which can be used as backup for the differential one. Hence, the signal readout had to be done using wires instead of LEMO connectors, as can be seen in figure 2.4b. By connecting two wires to the differential outputs and two more to ground, the output can be read out as two single-ended signals, one from each pair of wires (one pair consisting of a ground wire and the positive output of the differential signal, and the other of the negative one and ground).

The two designs are quite similar at the input, but if one looks closely it is obvious that the SAMPA chip of NCB is located closer to the input connectors than in OCB. This was done to shorten the input traces as the input is where a signal is most prone to noise. The traces in the new design were also separated as much as possible to reduce crosstalk.

The packaged SAMPA Chip 1 mounted on a carrier board is shown in figure 2.5a with the silicon chip visible in the center. Bonding wires connect the silicon chip to

the IC package, and the legs of the IC are soldered to the PCB. Figure 2.5b shows a closeup of the silicon chip and how the bonding wires are connected to it. The silicon chip is produced in a 130 nm CMOS technology and is roughly 3 mm long and 1.5 mm wide.

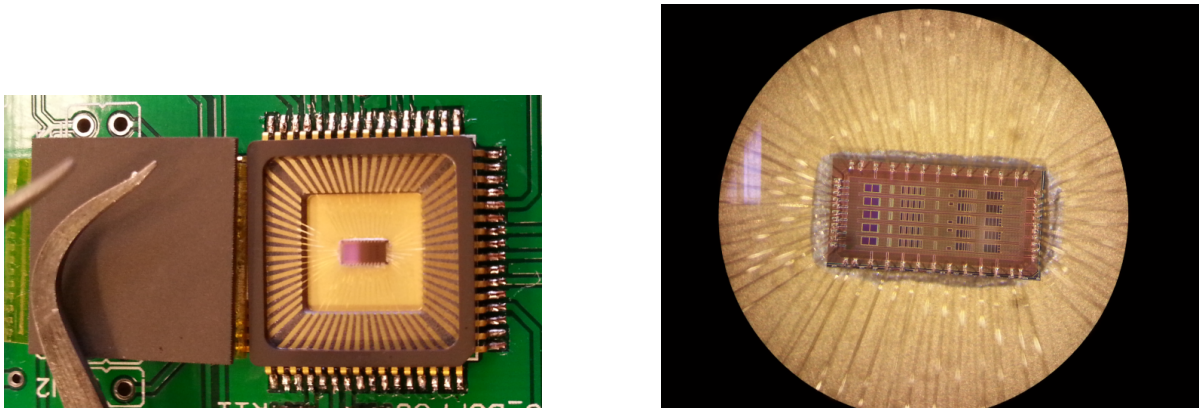

(a) (b)

Figure 2.5: (a) The packaged SAMPA Chip 1 mounted on a PCB. Bonding wires connect the silicon chip to the legs of the IC package which are soldered to the PCB. (b) A closeup of the SAMPA silicon Chip 1 showing where the bonding wires are connected.

Chapter 3

GEM Detectors

The particle-detection system of the ALICE TPC is currently based on wire-chambers. Before Run 3 of the LHC in 2018 it will be upgraded to a GEM-based (Gas Electron Multiplier) system to be able to handle the increased collision rates. Therefore, testing of GEM detectors has to be conducted to find the best setup and operating parameters before installing them in the ALICE TPC. For this purpose, a 10 by 10 cm GEM prototype (see section 3.8) was constructed in collaboration with the Hungarian group in their lab at the Wigner institute in Budapest. In addition to providing valuable information about GEM detectors, the prototype chamber could also be used to test the SAMPA Chip 1 under similar conditions to which it will be used in the ALICE TPC upgrade.

3.1 What is a GEM Detector?

A Gas Electron Multiplier (GEM) is a charge amplification device that was invented in 1996 by Fabio Sauli [14]. It consists of a thin insulating polymer foil which is coated with thin copper layers on either side. The foils are perforated with many tiny circular holes that are oriented in a hexagonal lattice. A closeup of a GEM foil is shown in figure 3.1, illustrating the size and orientation of the holes. The outer diameter is 70 µm and the hole pitch is 140 µm.

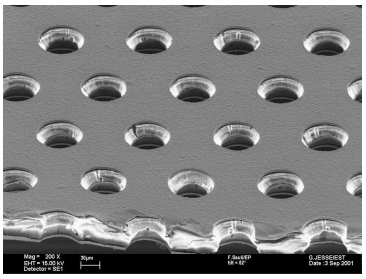

Figure 3.1: A closeup of a GEM foil showing the arrangement of the holes[15]. The diameter of the holes is 70 µm and the hole pitch is 140 µm.

3.2 Constituents

A GEM detector consists of three main parts, a cathode electrode, the GEM foil(s), and an anode for signal readout. The construction of a typical GEM detector is shown in figure 3.2. It consists of four GEM foils stacked on top of each other, separated by 2 mm. The anode readout plane is located below the GEM stack and the cathode electrode above. During operation the stack of foils is enclosed in an air-tight chamber which is filled with gas. High voltage is applied to the cathode and GEM foils, creating the electric fields labeled E_{drift}, E_{Ti} and E_{ind}. These refer to the drift-, transfer-, and induction fields, respectively, which are defined below:

- Drift field: The electric field between the cathode and the upper GEM foil.
- Transfer field(s): The electric field(s) between the GEM foils. If more than two foils are used, there will be more than one transfer field.
- Induction field: The electric field between the bottom GEM foil and the anode.

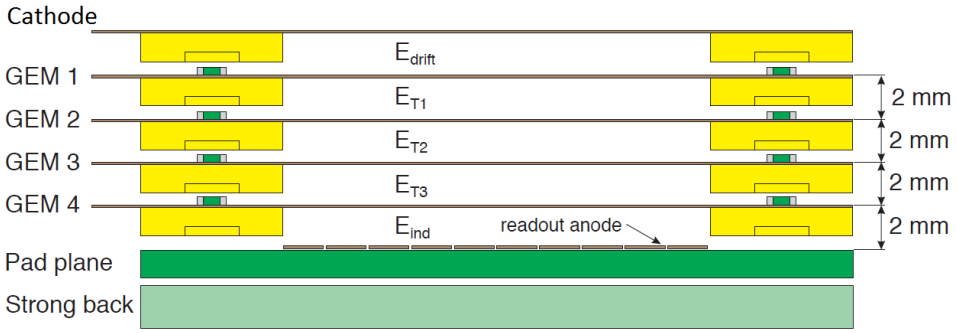

Figure 3.2: A typical GEM detector setup consisting of four GEM foils[11].

GEM foil

A typical GEM foil (the so-called standard design [16]) is constructed from a 50 µm thick kapton foil with a 5 µm thick copper electrode on either side. The foil is densely pierced with 70 µm in diameter holes with a pitch of 140 µm using a chemical etching process. A cross section of such a GEM foil is shown in figure 3.3. The white horizontal lines at the top and bottom of the foil are the copper planes. Due to the etching process the holes are not perfectly cylindrical, but rather double conical. This shape is a result of etching from both sides of the foil. If the foils were only etched from one side the resulting holes would be V-shaped. The GEM foils are produced at the CERN workshop using photo lithographic methods.

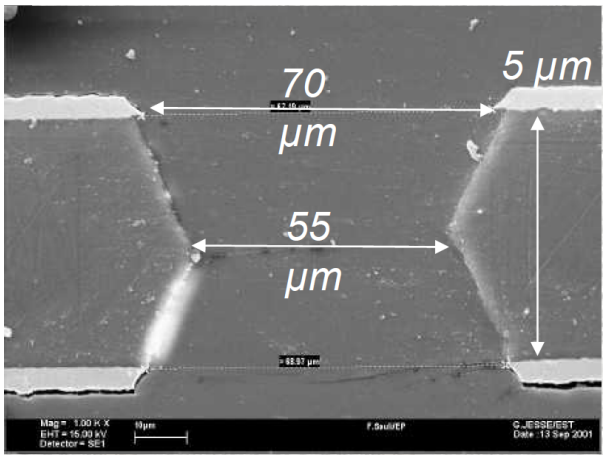

Figure 3.3: A closeup of the cross section of a GEM foil[15].

Cathode

The cathode electrode is used to create an electric field which attracts ionized electrons created by ionizing radiation to the first GEM foil. It can be constructed from either wires, wire-mesh, or metal film. The film type offers a very homogeneous electrical field, but cannot be used for discharge testing using α-particles since they don't penetrate the foil (see section 3.7). Wire and wire-mesh cathodes, however, are suitable this type of testing as they offer little obstacle to the α-particles, enabling them to reach the GEM foils and create discharges.

Anode

The anode of a GEM detector is used for signal readout. It is located below the bottom GEM foil and consists of a segmented copper plane where each segment is connected to a readout pin. As the anode acts as the "floor" of the detector, it needs to be strong so it can withstand mechanical stress due to handling. This can be done by adding a strong back-plane to it, as shown in figure 3.2.

3.3 Main Physical Processes

For the SAMPA Chip 1 testing with the GEM detector prototype an Fe-55 and a Sr-90 source were used. The Fe-55 source emits low energy photons (5.9 keV) which ionize the gas inside the detector as maximum ionizing particles. Due to their higher energy (2.28 MeV), the electrons emitted by the Sr-90 source interact with the detector gas as Minimum Ionizing Particles (MIPs). MIPs are discussed in section 3.3.3. The Fe-55 source is used to calibrate the gain of the detector and to obtain its energy resolution (see sections 4.2.1 and 4.2.2, respectively), while the Sr-90 is used for signal-to-noise ratio (SNR) calculations (see section 4.2.3).

3.3.1 Photoelectric Effect

For photon energies below ~0.5 MeV the photoelectric effect is the dominant process of attenuating electromagnetic radiation. Since the photons emitted by the Fe-55 radioactive source have 5.9 keV energy, they interact with the detector gas mainly through this process.

In the photoelectric effect a photon is completely absorbed in a collision with a bound electron. A free electron cannot absorb a photon and at the same time conserve its momentum, therefore it has to be bound such that the ionized atom can receive some of the momentum. Some of the photon's energy is therefore absorbed by the atom (E_A), some is used to overcome the electron's binding energy (E_b), and the rest becomes the electron's kinetic energy (E_k). With the photon energy being E_γ, the kinetic energy of the freed electron is given by equation 3.1.

$$E_k = E_\gamma - E_b - E_A \approx E_\gamma - E_b \tag{3.1}$$

The approximation can be done since $E_k/E_A \approx m/M < 1/1840$, where m is the electron mass and M is the mass of the atom.

The photoelectric effect is illustrated in figure 3.4. A photon is absorbed by a K-shell electron, which is ejected with kinetic energy E_k. The electron's binding energy is emitted either as characteristic X-ray radiation or as auger electrons[1].

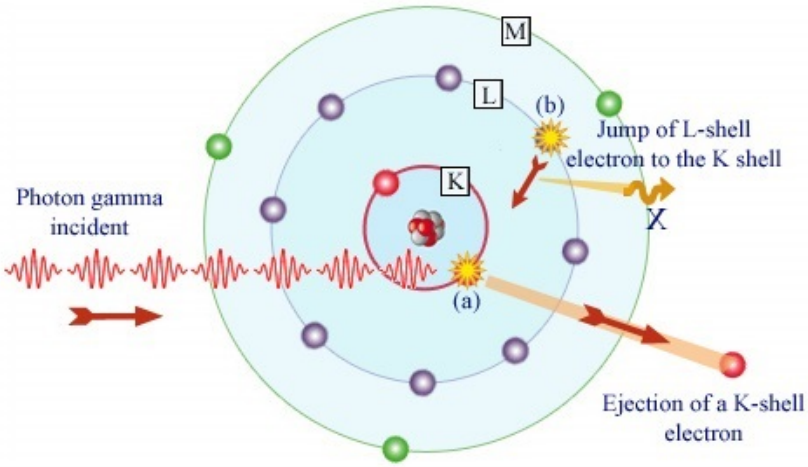

Figure 3.4: The photoelectric effect [5].

[1] Electrons which are ejected from the atom when an electron from a higher energy level fills the vacancy of a removed core electron.

3.3.2 Inelastic Scattering From Atomic Electrons

The electrons emitted by the Sr-90 source interact with the detector gas through inelastic scattering from atomic electrons, which lead to excitations[2] and ionizations[3]. Collisions that leave the incident atom excited or ionized are called *soft collisions* and *hard collisions*, respectively. After an ionization, the freed electron can have enough energy to further ionize other atoms. Such electrons are called δ-rays.

3.3.3 The Bethe-Bloch formula

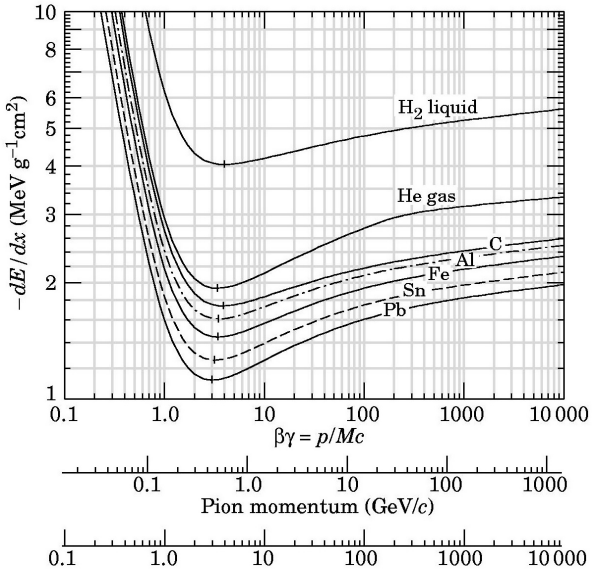

Figure 3.5: The Bethe-Bloch equation solved for numerous materials[2]. $\beta = \frac{v}{c}$ and $\gamma = \frac{1}{\sqrt{1-\beta^2}}$, where v is the particle velocity.

The mean rate of energy loss dE/dx for heavy charged particles (e.g. α or p^+) is described by the well known Bethe-Bloch equation. Sine the equation is rather cumbersome, it is not shown here. Instead, it is much more informative to view the graph of the function, which is shown in figure 3.5. The energy loss per unit distance is plotted as a function of particle momentum for various materials. It shows that fast particles (i.e. particles with higher energy) lose less energy per unit distance than slower particles. This is because faster particles have less time to interact with the electrons when passing through a material, thus losing less energy to ionization. The minimum value of $-\frac{dE}{dx}$ is found at approximately the same momentum for the various materials. Particles with momenta in this region are called *Minimum Ionizing*

[2] *Excitation* is a process in which an atom or a molecule receives outside energy, causing an electron to jump into an empty orbital of a higher energy shell.

[3] *Ionization* is a process in which an external particle collides with an outer-shell electron of an atom and knocks it out of orbit, resulting in an electrically charged atom.

Particles (MIPs). For protons the minimum ionizing region occurs at ~2-4 GeV/c. The rise in energy loss following the MIP point is due to relativistic effects.

3.3.4 Electron Avalanche

An electron avalanche is a process in which a free electron is accelerated by a strong electric field and subsequently collides with other atoms, thereby ionizing them and creating more electrons. The newly created electrons are subjected to the same electric field and further ionize more atoms, creating a chain reaction. Due to the higher mobility of electrons compared to ions (about 1000 times greater), the avalanche results in a liquid drop-like shape, with the electrons forming the front and the ions creating the tail. Figure 3.6 illustrates an electron avalanche. The figure to the left is photograph of an actual avalanche taken in a cloud chamber. To the right the avalanche is illustrated schematically, showing how the electrons and ions form the front and tail of the drop, respectively.

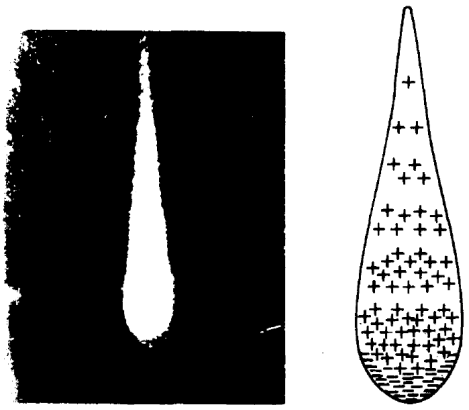

Figure 3.6: An electron avalanche forms a drop-like shape[13].

3.4 Gain

The gain of a GEM foil is the ratio of the number of electrons exiting the holes to the ones entering. For a single GEM foil this gain can be well above 10^3 [16], but this requires very high, and therefore unsafe, operating voltages (see section 3.7). However, since a GEM is a charge amplifier it can be used as a preamplifier for a another GEM, leading to the possibility of cascading several GEM foils to reach high gains without having to use unsafe operating voltages. A double or triple GEM setup will therefore allow high total gain at moderate voltages across the individual multipliers. The gain and discharge probability as a function of GEM voltage is shown in figure 3.7 for three GEM setups in the presence of a heavily ionizing background introduced through a ^{220}Rn α-source in the gas flow. The circular data points (green) are for a single-GEM setup (SGEM), the triangular ones (red) are for a double-GEM setup (DGEM), and the

square data points (blue) are for a triple-GEM setup. The solid lines show the gain, while the dotted ones show the discharge probability, both as a function of GEM voltage. As can be seen from the triple-GEM setup, for a given discharge probability, it offers significantly higher gain than both the single and double GEM and at lower GEM voltages.

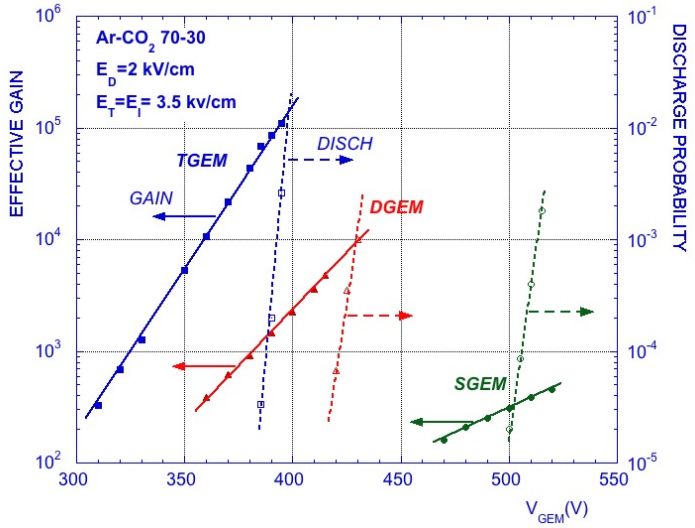

Figure 3.7: The gain and discharge probability as a function of GEM voltage for a single (SGEM), double (DGEM) and triple (TGEM) GEM setup in the presence of a heavily ionizing background [3].

The gain of a GEM detector is given in equation 3.2

$$G_{Eff} = \frac{I_{Anode}}{e * N_{Prim} * R}, \tag{3.2}$$

where I_{Anode} is the anode current, e is the electron charge, N_{Prim} is the number of primary ionizations[4] in the gas, and R is the rate of the incident ionizing particles. The experimental procedure of obtaining the anode current and pulse rate is discussed in section 4.2. An example of obtaining the number of primary ionizations in a gas is shown below:

[4] Primary ionization is the ionization produced by the primary particles, in contrast to total ionization, which includes the secondary ionization produced by delta-rays (secondary electrons which have obtained enough energy to produce further ionization).

3.5 Function

A GEM detector amplifies electrons through the electron avalanche process described in section 3.3.4. High voltage is applied to the GEM foils and cathode, creating the drift-, transfer- and induction fields. For GEM voltages of $\Delta_{U_{GEM}} = 200V$, electric fields of ~40 kV/cm are reached in the holes of the foil, and avalanche multiplication occurs if electrons drift into them. Ionizing particles traversing the detector dissipate their energy by exciting/ionizing the gas volume, creating electron-ion pairs. However, only the charge produced in the drift gap contributes significantly to the signal, since at least one amplification stage is missing for all other primary charge. The drift field causes the electrons to drift towards the topmost GEM foil where they enter the holes in the foil and are multiplied on their way through. The bigger electron cloud then drifts towards the second GEM foil (if more than one foil is used) under the influence of the first transfer field where the multiplication process is repeated. This is repeated for each GEM foil until the electron cloud is ejected into the induction field and drifts towards the anode plane where the charge is collected and read out by electronics. One of the big advantages of GEM detectors is this separation of the amplification region from the readout electronics. This limits the risk of damaging the fragile front-end electronics in case of discharges.

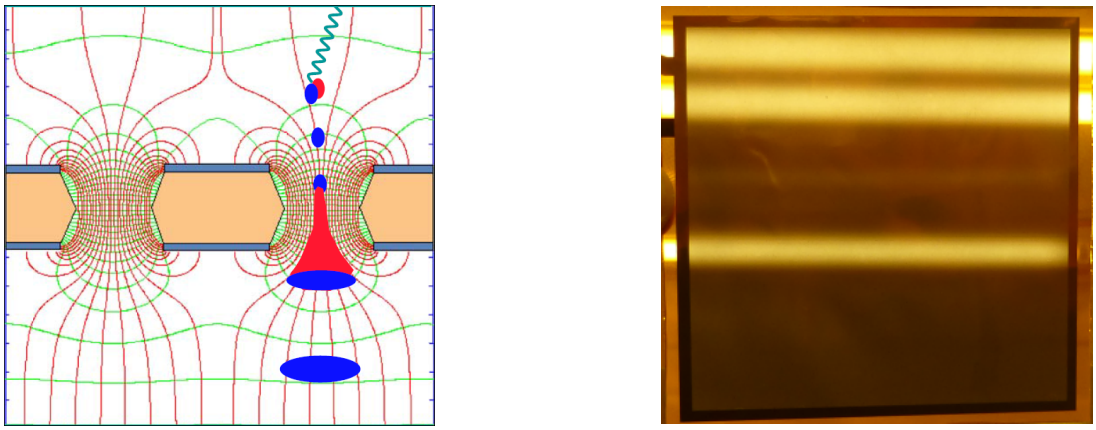

(a) (b)

Figure 3.8: (a) A simulation of the electric field lines in the holes of a GEM foil [15]. (b) An illustration of the optical transparency of a GEM foil.

A simulation of the electric field lines in a GEM hole is shown in figure 3.8a. Most of the field lines above the top electrode enter the holes and exit on the lower side. Therefore, most of the electrons drifting towards the foil will be caught by the electric field, undergo avalanche multiplication in the holes and exit on the lower side, leading to a high electrical transparency.

The optical transparency, however, is much lower and is given by equation 3.3.

$$Optical\ Transparency = \pi \frac{\sqrt{3}}{6} \left(\frac{d}{p}\right)^2, \tag{3.3}$$

where d is the diameter of the holes and p is the hole pitch. Inserting a diameter of 50 µm and a pitch of and 140 µm into the equation gives an optical transparency of 0.23. The transparency of such a foil is illustrated in figure 3.8b. As can be seen, it is not very transparent as it blurs the light from the fluorescent lights in the background.

Some of the field lines in figure 3.8a enter the kapton foil which leads to the deposition of electrons on the surface where the hole diameter is smallest. This additional charge increases the electrical field in the center of the hole, thus increasing the gain. Due to this phenomenon, called *charging up*, the gain of a GEM increases by ~20% when irradiated. A charge-up study is illustrated in figure 3.15.

3.6 Gas Choice

Electron multiplication is in principle possible in any gas or gas mixture, but for detector applications the choice of gas is restricted by specific requirements such as low operating voltage, high gain, and high stability. Because noble gases have properties that best suit these requirements, they are often the main component in most detector gases. Free electrons are easily captured by oxygen or water vapor molecules, forming negative ions. Therefore, it is important to keep the oxygen/water contamination of the detector gas to a minimum.

3.6.1 Noble gases

Gas multiplication (electron avalanche) occurs at lower electrical fields in noble gases than in gases composed of complex molecules [16]. This, and the fact that noble gases are inert (they do not chemically react with other materials), make them the main component in most detector gas fillings.

To be able to generate enough primary charge to detect minimum-ionizing particles, high specific ionization[5] is necessary. The specific ionization increases with the atomic number of the gas atom, so larger atoms like xenon and krypton offer the best properties. However, since xenon and krypton are expensive, the natural choice for detector gas is argon.

3.6.2 Quenchers

An incoming charged particle will create both excited and ionized gas atoms inside the detector. The ionized electrons generate the charge which is used to detect the particle, but the exited atoms do not contribute to this charge. However, exited noble gases can only return to their ground state through the emission of a photon. If these photons have energies greater than the ionization energy of the copper electrodes in the detector, they create new electrons through the photoelectric effect (see section

[5] Specific Ionization is the average number of ion pairs generated by ionizing particles per unit length of path.

3.3.1). Since these electrons do not originate from the incoming ionizing particle, they should not be amplified by the detector.

The minimum energy of a photon emitted by argon is 11.6 eV (the excitation energy), which is well above the ionization energy of copper (7.2 eV). A quencher gas is therefore required to absorb the photons emitted by the exited argon atoms. CO_2 is an example of such a quencher gas, and is often a small part of the detector gas mixture. Although it has significantly lower quenching efficiency than organic gases (e.g. isobutane), it shows no signs of aging (polymer deposits on the electrodes which change the detector characteristics) and is non-flammable.

3.7 Discharges

The occurrence of discharges (sparks) is a limiting factor in all micro pattern gas detectors at high gain, especially under the influence of heavily ionizing particles. It occurs if the total charge in the avalanche exceeds the Raether limit[6] of between 10^7 and 10^8 electron-ion pairs[16]. A discharge that remains localized to the multiplier foil is called a *non-propagated discharge*. However, it may occur that the discharge propagates through the induction gap to the anode plane, causing what is called a *propagated discharge*. In most cases the discharges are non-propagating, but the probability for a discharge to propagate rises with the strength of the induction field. If a propagated discharge occurs, a very large current is delivered to the anode plane, since the full capacitance between the GEM foil and the readout plane is discharged, possibly damaging the front end electronics.

It is important to prevent a discharge from becoming continuous (multiple discharges following in rapid succession), because this can melt the kapton foil and fuse the two copper electrodes together, permanently destroying the GEM foil. This is done by placing protective resistors between the HV input and the GEM foils which limit the current that recharges the foils after a discharge, prolonging the time it takes to recharge them. This gives the electron-ion pairs created by the initial spark time to recombine into neutral atoms before the foils are recharged and a new spark can occur.

3.7.1 Discharge Testing

To be able to test the protection circuitry for the front end electronics (FEE) during a discharge, one has to be able to provoke discharges. There are two common ways of doing this:

- Using Radon gas. A thorium source which decays into radon is placed within the gas supply of the chamber. The radon gas emits α-particles which create sparks when they traverse the holes in the GEM foils.

[6] The Raether limit is the physical limiting value of the multiplication factor (M) or gas gain in an ionization avalanche process (Townsend avalanche)

- Using an α-source. An α-source is placed either outside or inside of the GEM chamber. If it is placed outside, the cover and cathode of the detector have to be made so the α-particles can penetrate them and reach the GEM foils. This can be done by creating a small window (e.g. $1 \times 1\ cm^2$) in the cover of the detector which is thinner than the surrounding material, allowing the α-particles to penetrate it, and by using a wire-mesh cathode. This enables the α-particles access to the GEM foils where they can create sparks.

  If the α-source is located inside the detector one has no way of controlling when the discharges occur. Since the inside of a GEM chamber has to be very clean, one cannot simply open it to remove the source - this has to be done in special clean-rooms. Therefore, it is very inconvenient to place the α-source inside the detector.

3.8 GEM Prototype Chamber [$10 \times 10\ cm^2$]

The GEM stack of the prototype detector consists of a cathode foil, three GEM foils and an anode readout plane. The foils are separated by spacers and are held in place by four threaded plastic pillars which are glued to the anode plane. A photograph of the detector prototype during construction is shown in figure 3.9. High voltage leads (red and blue wires) connect the foils to a resistor chain which is powered by a HV power supply. The cathode is the only foil which has not been mounted in the figure, all three GEM foils have been placed with the first one visible at the top. It is preferable to have a large drift gap since it increases the distance over which the incoming particles dissipate their energy, increasing the primary signal charge. Therefore, a few more spacers where needed before the cathode was installed to make the drift gap as large as possible, the limiting factor being the hight of the chamber. The maximum drift gap was found to be 7 mm.

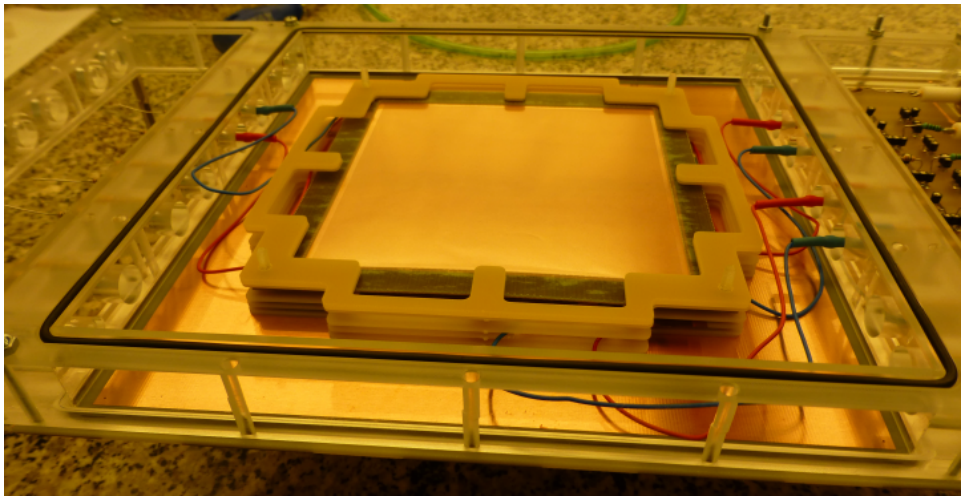

Figure 3.9: The prototype detector during construction.

During the first assembly process small plastic washers were used to separated the foils, but this proved unsuccessful because the foils tended to sag and warp, causing inconsistent spacing. To fix this problem, a special set of spacers were designed which support the foils over a much larger area, minimizing the warpage. Figure 3.10 illustrates one such spacer. The spacers had to be carefully designed so they wouldn't hinder the gas flow through the detector or interfere with the electron flow during operation. The fins marked by the red arrows support the middle of each side of the GEM foils. The spacers measure 144 mm at the widest point and the distance between the mounting holes visible in each corner is 117 mm center to center. They were made in two thicknesses, 0.8 and 2.0 mm, to enable very accurate spacing between the foils.

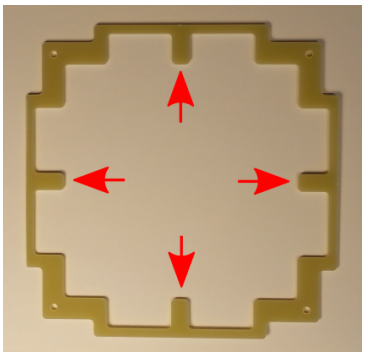

Figure 3.10: An example of the type of spacer used to separate the GEM foils and cathode in the prototype GEM detector.

3.8.1 Enclosure

Since the GEM stack has to be in a very pure gaseous atmosphere, it has to be enclosed in a gas tight container. The container used in the prototype detector is a frame machined out of a block of transparent plastic (see figure 3.9). Special grooves were machined around the top and bottom circumference of the frame where the GEM stack would be enclosed. O-ring seals (black rubber) snugly fit inside the grooves and make the GEM chamber air-tight once the top cover is bolted on. High voltage leads (red and blue wires) are connected to air-tight connectors which penetrate through the chamber wall and connect to the HV power supply. A total of 7 HV connectors were needed for the 3 GEM system (1 for the cathode, and 6 for the top and bottom of each GEM foil), but two more holes were drilled in the frame to accommodate a 4th GEM foil in case a quadruple GEM system was needed. The unused holes were also fitted with O-rings and HV connectors to make the chamber air-tight.

3.8.2 Anode Plane

The anode plane of the prototype detector is made from a PCB board and is shown in figure 3.11. The PCB laminate gives the structure rigidity while the copper layer acts as the anode electrode. The copper layer is segmented into pad sizes corresponding to the ones that will be used in the ALICE TPC upgrade. The $4 \times 7.5\ mm^2$ pads are used in the Inner Readout Chambers (IROCs) while the $6 \times 10\ mm^2$ and $6 \times 15\ mm^2$ pads are used in the Outer Readout Chambers (OROCs). It also features one large pad ($30 \times 30\ mm^2$) which can be used for function testing and gain calibration.

The pads to the right in the figure are arranged in clusters of three. The rings around the clusters are used to determine the position of the radioactive source while calibrating the detector. Since the whole detector is quite thick and opaque, it is difficult to accurately place the radioactive source directly above a pad. By comparing the signal amplitudes of the pads and rings while positioning the source, one can determine where it is pointing. If the signal amplitude of the ring is greater than from the pads, the source is not pointing directly at the pad and adjustments can be made.

Pins on the other side of the PCB are connected to each pad/section of the anode

electrode. The red dots highlight where some of the vias are placed which connect the pads to the pins. The holes though the PCB laminate which the vias created had to be sealed before operating the detector. This was done by placing a small drop of glue over each hole.

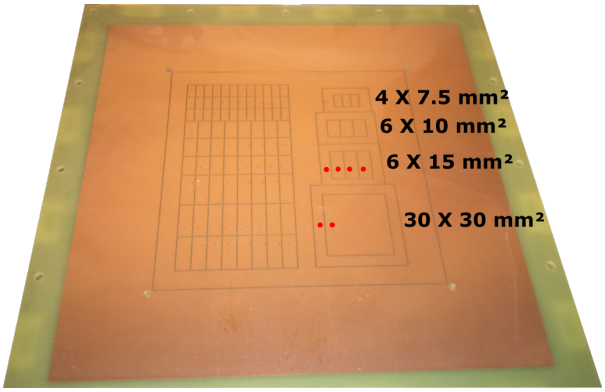

Figure 3.11: The Anode plane of the prototype GEM detector.

3.8.3 Resistor Chain

A resistor chain was designed so that the prototype GEM detector could be powered from a single High Voltage Power Supply (HVPS). The purpose of the resistor chain is to divide the power supply voltage so that each element in the detector receives the correct operating voltage. The ratios of the resistors in the chain determine the voltages.

A schematic view of the resistor chain is shown in figure 3.12. R1 and C create a low-pass filter which reduces the noise coming from the HV power supply. R2 and the 10 MΩ resistors (R) are protective resistors used to limit the current surge in case of a discharge (see section 3.7). This hinders continuous sparks (multiple discharges taking place in rapid succession) from occurring as a result of the GEM foils being charged up too fast. R3 through R9 set the voltages across each element in the GEM chamber. UG1 through UG3 refer to the voltages across each GEM foil. UD, UT1, UT2 and UInd refer to the voltages which set the drift-, transfer- and induction fields. Since the cathode is at the lowest potential in a GEM detector, the voltages are referred with the positive sign (+) closest to ground potential. The voltages with the blue color are referred to ground, that is why they lack the plus/minus (+/-) labels. They are used to define the red voltages, e.g. $UG3 = UG3B - UG3T$

The voltage across each element in a resistor chain is simply the ratio of the resistor value to the total resistance in the chain, $R_{Total} = \sum_{i=1}^{9} R_i$. The resistances labeled "R" in the schematic don't affect the total resistance since the GEM currents are negligible. Two simple voltage divisions give the expressions for U_{G1T} and U_{G1B} in equations 3.4

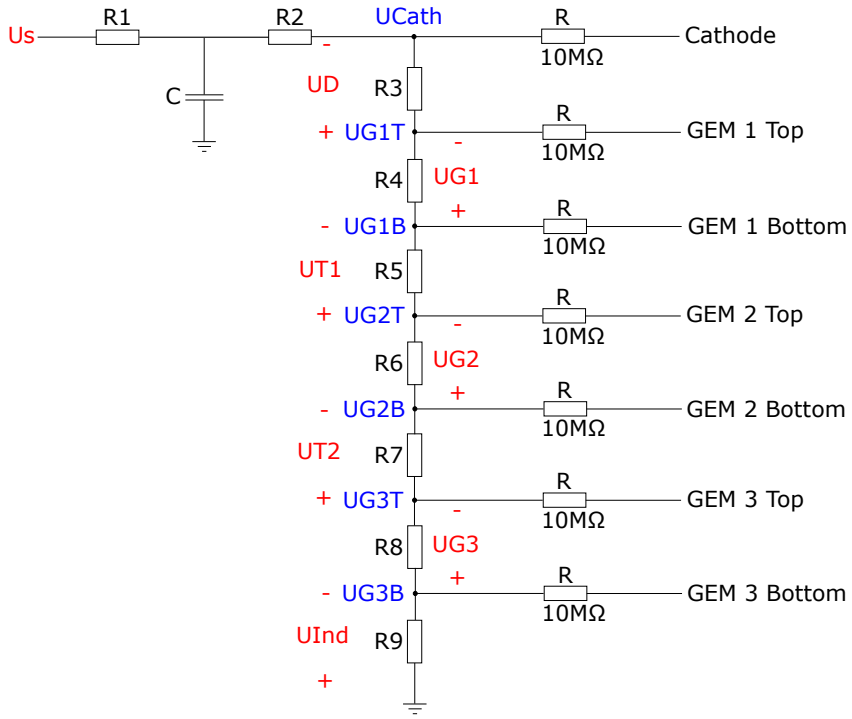

Figure 3.12: A schematic view of the resistor chain used in the prototype GEM chamber.

and 3.5, respectively.

$$\frac{U_{G1T}}{U_S} = \frac{\sum_{i=4}^{9} R_i}{R_{Total}} \tag{3.4}$$

$$\frac{U_{G1B}}{U_S} = \frac{\sum_{i=5}^{9} R_i}{R_{Total}} \tag{3.5}$$

By subtracting equation 3.5 from 3.4, an expression for the voltage across the first GEM foil is found, as shown in equation 3.6.

$$-\frac{U_{G1}}{U_S} = \frac{U_{G1T}}{U_S} - \frac{U_{G1B}}{U_S} = \frac{R4}{R_{Total}} \tag{3.6}$$

The minus sign comes from the definition of U_{G1} in figure 3.12.

The expression in equation 3.6 is valid for any of the other voltages in the resistor chain also, the only parameter that changes is the resistor name in the numerator. I.e., to find the voltage across any of the resistors in the chain, simply divide the value of said resistor by the total resistance in the chain, and multiply this number by the supply voltage.

Selecting the HV settings

In order to minimize ion backflow[7] , the electric field configuration of the GEM stack as well as the gain sharing among the amplification stages have been optimized in the ALICE TPC upgrade TDR for a quadruple GEM system. The optimized parameters are listed in table 3.1. Ion backflow of less than 1 % can be achieved with a quadruple GEM system at these voltage settings[11].

Parameter	Voltage	Electric Field
Drift field		0.40 kV/cm
$\Delta U_{GEM\ 1}$	270 V	
Transfer field 1		4.0 kV/cm
$\Delta U_{GEM\ 2}$	250 V	
Transfer field 2		2.0 kV/cm
$\Delta U_{GEM\ 3}$	270 V	
Transfer field 3		0.1 kV/cm
$\Delta U_{GEM\ 4}$	340 V	
Induction field		4.0 kV/cm

Table 3.1: Typical HV settings for a quadruple GEM system achieving ~2000 gain in Ne-CO_2N_2 (90-10-5)[11].

The operating voltages for the prototype GEM detector were chosen so they would largely coincide with the typical HV settings shown in table 3.1. Since only three GEM foils were used in the prototype detector, the voltages had to be increased compared to the quadruple system. Moreover, during the initial testing of the detector Ar-CO_2 (80-20) was used instead of Ne-CO_2N_2 (90-10-5), further increasing the required operating voltages. Tests had shown that GEM voltages of roughly 310 V resulted in ~2000 gain in Ar-CO_2 (80-20) for the triple GEM system. The drift field was chosen equal to that suggested in the TDR (400 V/cm) followed by a high first transfer field of 3 kV/cm. The second transfer field was given a low value of 400 V/cm, and finally the induction field was given a high value of 3 kV/cm. The selected HV settings for the GEM detector prototype are summed up in table 3.2.

E_{Drift}	U_{G1}	E_{T1}	U_{G1}	E_{T2}	U_{G1}	E_{Ind}
400 V/cm	310 V	3 kV/cm	310 V	0.4 kV/cm	310 V	3 kV/cm

Table 3.2: The selected HV settings for the prototype GEM detector.

[7] Ion backflow (IB) is the ratio of cathode to anode current, $IB = \frac{I_{Cathode}}{I_{Anode}} = \frac{1+\epsilon}{G_{eff}}$, where ϵ is the number of ions drifting back into the drift region from the amplification region per incoming electron[11].

Calculating the resistor chain

Once the operating voltages of the prototype detector were established the resistor chain could be designed. The design was based on the schematic shown in figure 3.12 and the following procedure was used to calculate the resistor values.

1. The GEM-, drift-, transfer-, and induction voltages needed in the detector are calculated in table 3.3. The second column contains the selected electric field values from table 3.2. Together with the distances shown in the third column, the corresponding voltages which create these fields are calculated in the last column. By adding all the voltages in the last column, one can calculate that the total voltage required by the HV power supply is ~2600 V. This is, however, not entirely accurate since the voltage drops across R1 and R2 (see figure 3.12) are not included, but it gives a rough idea of the required voltage.

	Electric Field [V/cm]	Spacing [mm]	Voltage [V]
Drift Field	400	7.0	280
GEM 1			310
Transfer field 1	3000	2.1	630
GEM 2			310
Transfer field 2	400	2.1	84
GEM 3			310
Induction Field	3000	2.25	675
SUM			≈ 2600

Table 3.3: The calculated voltages the resistor chain has to provide.

2. Knowing that the total voltage across the resistor chain would be in the range of 3 kV, it would be reasonable to choose resistor values that added up to roughly 100 MΩ as not to overload the HV power supply. ~3 kV across 100 MΩ requires a current of roughly 30 µA, and a power consumption in the range of 900 mW.

3. A current of 30 µA was chosen as a basis to calculate the values in the resistor chain. Dividing the voltage across each field/foil by this current gives the resistor values. This is done in table 3.4. R1 and R2 are not calculated in the table, since their values are not important. They only act as filtering and protection resistors, respectively.

4. Once the resistor values had been calculated, the closest match found in the E12 series[8] were selected. Resistors from other series (e.g. E24 or E96) which would have provided a closer match to the calculated values were not available. However, due to the flexible design of the chamber's HV input, it was possible

[8] In the E12 series, each decade is divided into 12 steps. The size of every step is $10^{\frac{1}{12}} = 1.21$, which means that each value is 1.21 times greater than the last.

	R3	R4,6,8	R5	R7	R9
Voltage [V]	280	310	630	84	675
Current [μA]	30	30	30	30	30
Resistance [MΩ]	9.3	10.3	21.0	2.8	22.5

Table 3.4: The calculated resistor values for the resistor chain.

to connect resistors in series and parallel to come closer to the correct values. Table 3.5 shows what resistor values were selected. Resistors are shown with the ”plus” (+) sign if they are in series, and the ”parallel” sign (||) if they are connected in parallel.

	R3	R4,6,8	R5	R7	R9
Resistance [MΩ]	$4.7 + 4.7 = 9.4$	10	22	$5.1 \| \| 6.8 = 2.9$	22

Table 3.5: The selected values for the resistor chain.

5. R1 and R2 were both given the values of 6.8 MΩ so that the total resistance in the chain became ~100 MΩ. Since the resistances across the GEM foils are 10 MΩ, the GEM voltages thus become 1/10 of the supply voltage. This is very convenient when calibrating the detector gain as no calculator is needed to obtain the GEM voltages for a given supply voltage.

3.8.4 Measurements

An Fe-55 energy spectrum recorded with the prototype GEM detector is shown in figure 3.13. The gain of the detector during this measurement was roughly 2200 and the gas used was Ar-CO_2 (80-20) at a flow rate of 8 l/h.

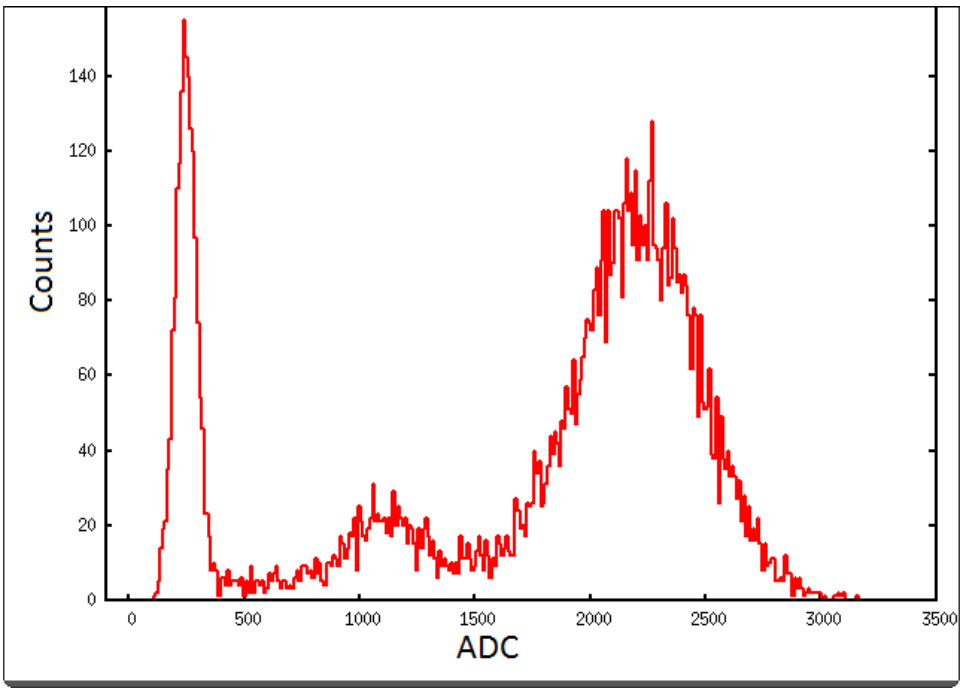

Figure 3.13: An Fe-55 energy spectrum in Ar-CO_2 (80-20) recorded using the prototype GEM detector.

An overnight gain scan of the GEM detector prototype is shown in figure 3.14. It shows how the relative gain of the detector varies as a function of time. The test was conducted over a time span of 16 hours during which the peak position of the energy spectra from the Fe-55 source were recorded and plotted. No temperature recording was done to see how it affected the gain, but the test was conducted in a lab with stable working conditions. Small temperature variations may however have occurred because of centralized heating which was turned down during the night. As the plot shows, the maximum gain variation was roughly 2 % which suggest that the prototype detector has very stable gain, especially when considering the possibility of temperature variations.

A charge-up study (see section 3.5) of the prototype GEM detector was done to see how the gain changed as a function of time when irradiated. Before the measurement was done the detector had been powered off and removed from irradiation for many hours since the discharging process is very slow. The results from the measurement are shown in figure 3.15. The relative gain of the detector is plotted as a function of time. A plateau was reached after roughly 3-4 hours, by which time the gain had increased by 13 %.

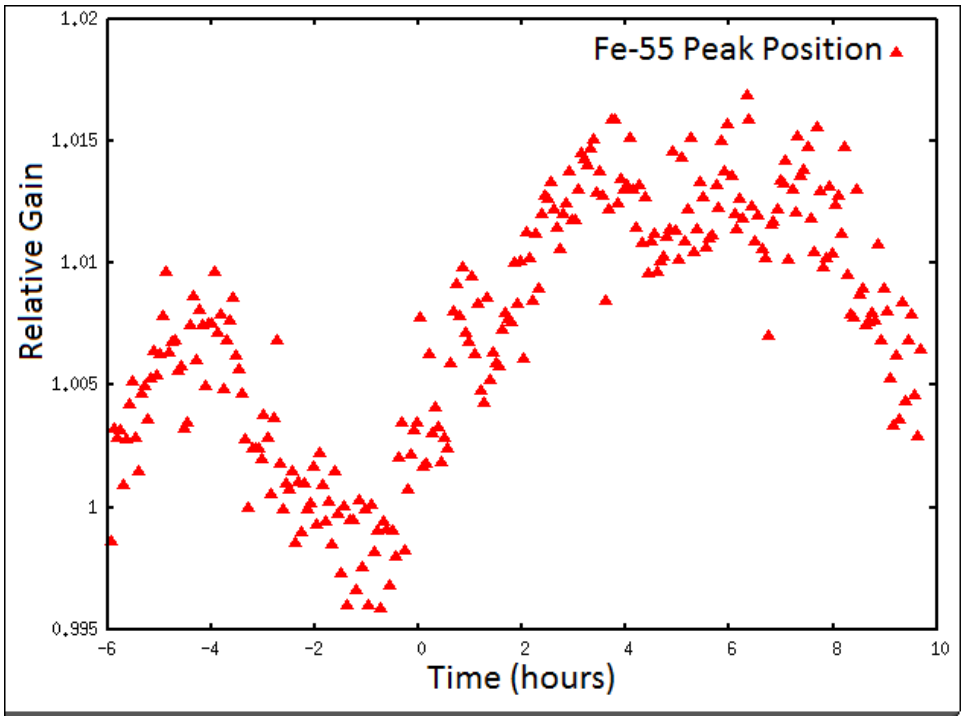

Figure 3.14: An overnight gain scan of the prototype GEM detector. It shows a maximum gain variation of ~2 %.

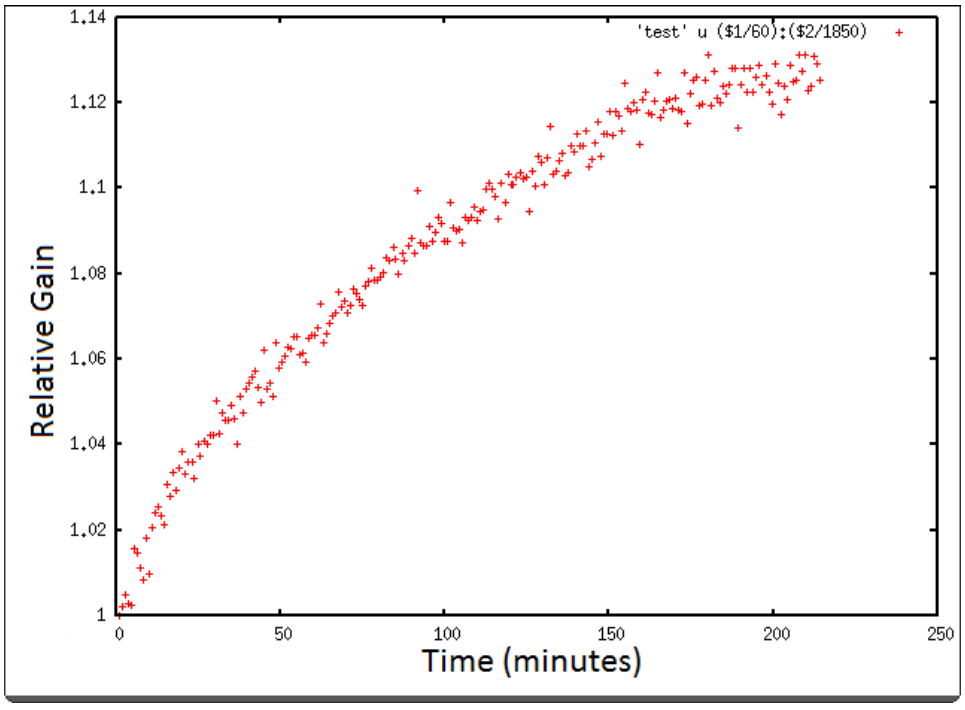

Figure 3.15: A charge-up study of the prototype GEM detector showing how the gain varies as a function of time when the GEM foils are irradiated.

A comparison of the energy spectra for Sr-90 and Fe-55 in Ne-CO_2-N_2 (90-10-5) is shown in figure 3.16. Since the Sr-90 electrons are minimum ionizing particles (MIPs) they create far less primary charge in the drift gap than the Fe-55 photons. This difference is illustrated by the peak positions of the two graphs, the Sr-90 peak is hardly distinguishable from the noise while the Fe-55 peak is clearly visible and located way above the noise level. The detector gain during this experiment was roughly 2500 and the flow rate was 8 l/h.

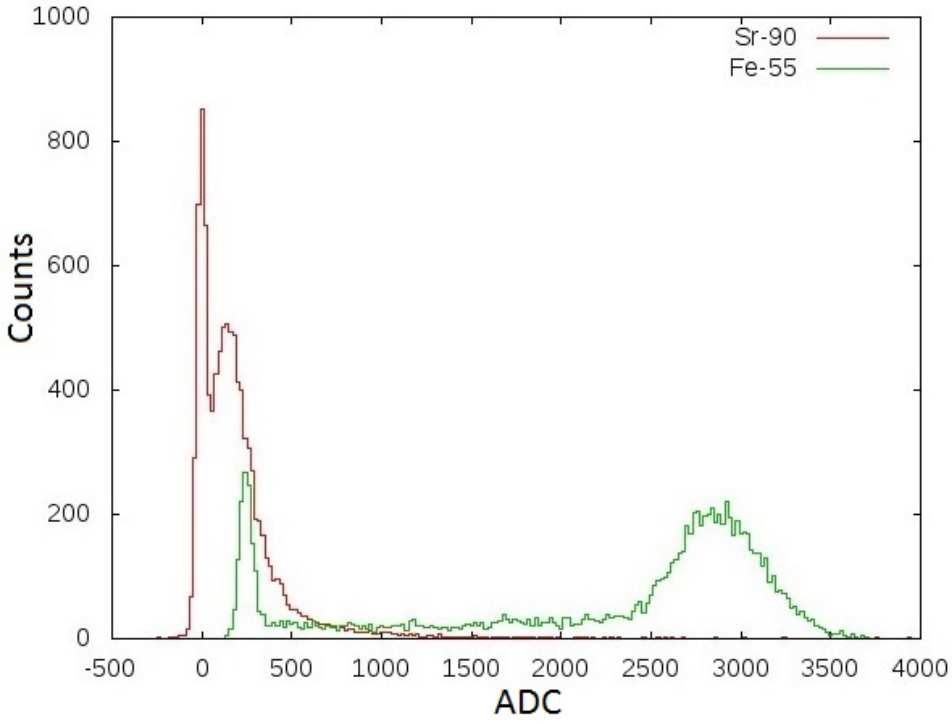

Figure 3.16: A comparison plot of the energy spectra for Sr-90 and Fe-55 in Ne-CO_2-N_2 (90-10-5). MIPs (Sr-90) create very little primary charge in the drift gap and are hard to detect.

Chapter 4

SAMPA Tests

The first prototype of the SAMPA Chip 1 is characterized for signals generated by a signal generator and a GEM detector prototype. The following equipment was used during the measurements:

- Oscilloscope: Tectronix DPO 7254 Digital Phosphor Oscilloscope
  Serial number: B033137
- ADC: CAEN Mod. V1729A
  Serial number: MAT14VS2
- Multimeter: Fluke 87 True RMS Multimeter
  Serial number: -
- Capacitance Meter: DER EE DE-5000 LCR Meter
  Serial number: L0004802
- Picoammeter: Keithley 487 Picoammeter / Votage Source
  Serial number: 0617909
- Signal generator: Agilent 33250A 80 MHz Function / Arbitrary Waveform Generator
  Serial number: 33250A
- Power supply: TDI EL302D Dual Power Supply
  Serial number: 314833

In addition, wherever possible, LEMO cables were used to connect the input and output signals to the equipment.

Four samples of the SAMPA Chip 1 (preamplifier and shaper) were available for testing, OCB1, OCB2, NCB1 and NCB2.

DC Parameters of Chip 1

It is important to regularly check the baseline parameters before any test since working conditions (e.g. temperature) affect electronics. Therefore, all DC operating parameters were checked before each test to ensure similar test conditions. The nominal DC parameters during the tests are listed below:

- V_{+5V}: +5.00 V
- V_{-5V}: -5.00 V (Only used in the new PCB layout)
- V_{DD}: 1.25 V SAMPA power supply
- V_{450}: 450 mV reference voltage
- V_{600}: 600 mV reference voltage
- V_{750}: 750 mV reference voltage

In the old carrier board design (see figure 2.4a), there are two power supply inputs, V_{+5V} and V_{DD}. This design does not utilize the V_{-5V} because it has no embedded buffer. V_{DD} powers the SAMPA chip while V_{+5V} is used to generate the reference voltages. In the new carrier board design (see figure 2.4b), a power supply of $\pm$ 5V is used. The reference voltages (450 mV, 600 mV and 750 mV) and V_{DD} of 1.25 V are derived from the V_{+5V} supply.

All the voltages made on-chip (both in the old and new PCB design) can be adjusted externally through the use of potentiometers. Test pads connected to each source give easy access while adjusting the potentiometers to the correct positions. Before each test was done all DC voltages were checked and adjusted as precisely as possible.

4.1 Pulse Shape Generator

In this section the SAMPA Chip 1 characterization tests using a pulse shape generator are reported. These tests include power consumption, gain linearity, pulse shape stability, crosstalk and noise.

4.1.1 Power Consumption

A power consumption test was done to see if the SAMPA Chip 1 fulfills the ALICE TDR requirement [10] of less than 6 mW per channel. It was done for both high (30 mV/fC) and low (20 mV/fC) gain over a supply voltage range of 1.18 V to 1.27 V in steps of 20 or 30 mV with 1.25 V being the nominal supply voltage. Because the old carrier board has a separate input for V_{DD} (the SAMPA Chip 1 power supply) it was used during the test. The new carrier board does not have a separate power input for V_{DD} and could therefore not be used.

The experimental test setup for the power consumption test is shown in figure 4.1. The multimeter was used as a current meter and was coupled in series with the power supply. The supply voltage was measured at the input of the chip so as not to include any voltage drops across the cables/meter. To see if the input signal played a role in the power consumption a charge was injected into the chip in some of the experiments.

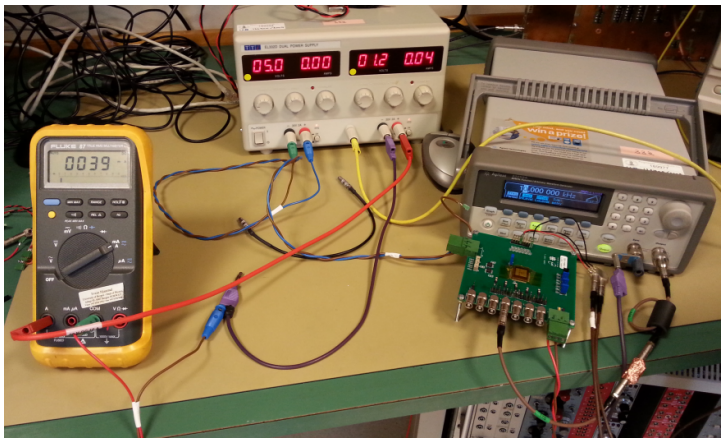

Figure 4.1: The power consumption test setup. Although the picture shows the measured current in mA, it was possible to increase the accuracy of the multimeter so that it showed an additional two decimal places. All operating voltages were measured at the power input of the chip to get accurate values.

The total power consumption was obtained by multiplying the measured current with the operating voltage. This value was divided by five (the number of channels on Chip 1) to obtain the power consumption per channel. Table 4.1 shows the total current (mA) and power (mW) consumption of the SAMPA Chip 1 for both high (30 mV/fC) and low (20 mV/fC) gain over the range of supply voltages. Injecting a signal to the input of the chip had no measurable effect on the power consumption.

The accuracy of the Fluke 87 True RMS Multimeter used for the current measurement is ± 0.2 % of the measured value plus 4 least significant digits when measuring DC current in the mA range[6].

Supply Voltage [V]	Current Consumption [mA]		Power Consumption [mW]	
	Low Gain (20 mV/fC)	High Gain (30 mV/fC)	Low Gain (20 mV/fC)	High Gain (30 mV/fC)
1.18	33.02 ± 0.10	34.14 ± 0.11	38.96 ± 0.12	40.29 ± 0.12
1.20	33.84 ± 0.11	34.94 ± 0.11	40.61 ± 0.12	41.93 ± 0.12
1.22	34.64 ± 0.11	35.77 ± 0.11	42.26 ± 0.12	43.64 ± 0.13
1.25	36.00 ± 0.11	37.12 ± 0.11	45.00 ± 0.13	46.40 ± 0.13
1.27	36.97 ± 0.11	38.05 ± 0.12	46.95 ± 0.13	48.32 ± 0.14

Table 4.1: The measured current and power consumption of the SAMPA Chip 1 over a range of different supply voltages for both low and high gain.

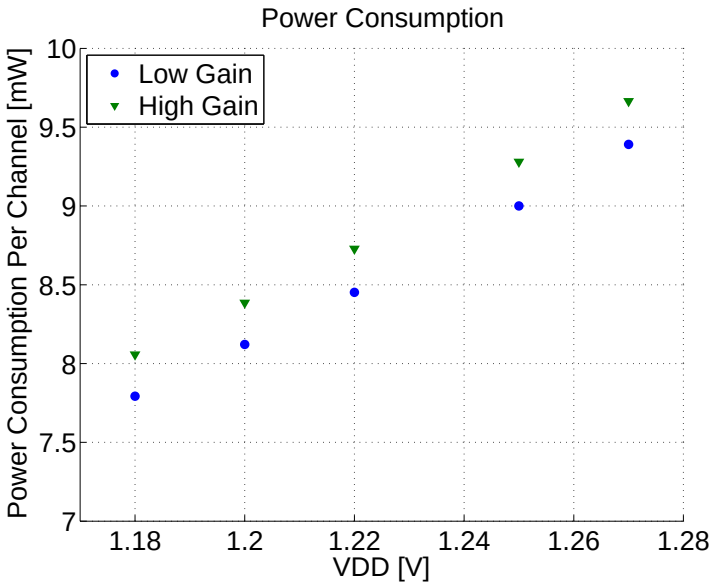

Figure 4.2: The power consumption of the SAMPA Chip 1 per channel.

The power consumption per channel is shown graphically in figure 4.2. It seems to increase linearly with the supply voltage. To meet the requirements of the TDR, the total power consumption for five channels should not exceed 35 mW for 1.25 V supply voltage. As table 4.1 shows the power consumption is 45.00 ± 0.13 mW and 46.40 ± 0.13 mV, respectively. These values correspond to 9.00 ± 0.03 mW and 9.28 ± 0.03 mW per channel for low and high gain, respectively. The power consumption requirement has not been met.

4.1.2 Gain and Pulse Shape Stability

A pulse shape stability test was done to ensure that the SAMPA chip creates identical output pulses for a given input signal. If it doesn't, this would imply that either the gain and/or the rise/fall time of the chip was not constant. Hence, using this experiment it is also possible to confirm gain linearity.

To perform this test ramp signals from the pulse shape generator were injected into the SAMPA chip through a 1 pF capacitor. The injected charge was varied from 2 to 120 fC. The output of the SAMPA chip was fed to the ADC for digitization and the ADC output samples were analyzed using LabView[7]. To reduce ambient noise, the chip was placed inside the Faraday cage. The test setup is shown in figure 4.3.

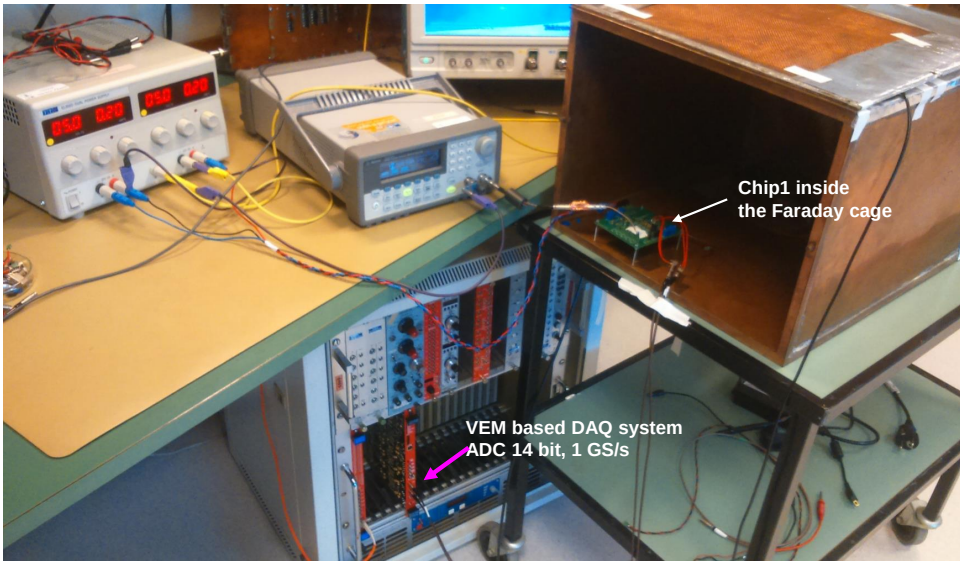

Figure 4.3: The experimental setup used during the pulse shape stability test.

The test parameters used during the pulse shape stability test are listed below.

- Input signal Low Gain: 2-120 mV_{PP} through 1 pF capacitor
- Input signal High Gain: 2-80 mV_{PP} through 1 pF capacitor
- Signal shape: Ramp with 100 % symmetry
- Frequency: 10 kHz
- 2 to 10 mV step size: 1 mV
- 10 to 120 mV step size: 10 mV
- ADC sampling rate: 1 GHz
- ADC threshold: 150

The test was done for NCB1 and NCB2 for all five channels, both high and low gain. The old PCB designs (OCB1 and OCB2) could not be used because the input of the ADC used for data acquisition was 50 Ω terminated.

Two parameters were measured and compared to each other; the pulse height (amplitude) and the integral (area) of the output pulse, as shown in figure 4.4. The peak detection and integral functions (sub-VIs[1]) of LabView were used to estimate the amplitude and area.

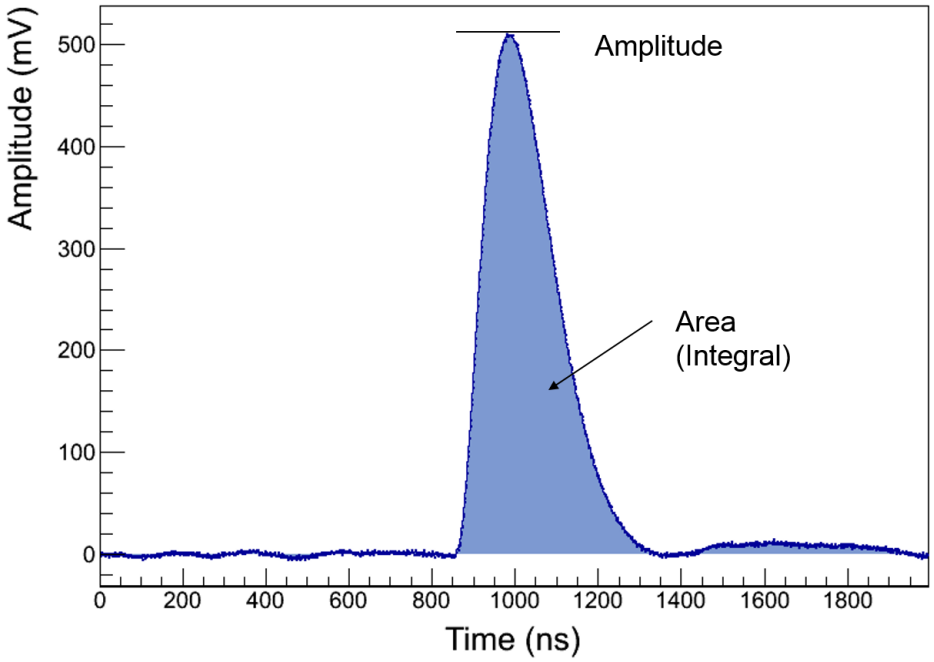

Figure 4.4: An example waveform showing the amplitude and integral used for the pulse shape stability studies. The sampling rate of the ADC was 1 GHz.

The procedure of obtaining the amplitude and integral is shown in figure 4.5. The two single-ended signals from the SAMPA chip (figure 4.5a) are subtracted from each other using LabView to get the differential output signal, shown in figure 4.5b. The amplitude is obtained using a peak detection VI of LabView. These values are filled in a histogram and plotted in figure 4.5c.

A similar approach is used to find the integral. First the integral of the differential signal is calculated and displayed using LabView (figure 4.5d). Then a peak detection VI is used to find the maximum value of the integral. To make the results readable, the integral values are divided by 10,000 before they are filled in the histogram (figure 4.5e).

[1]Virtual Instruments

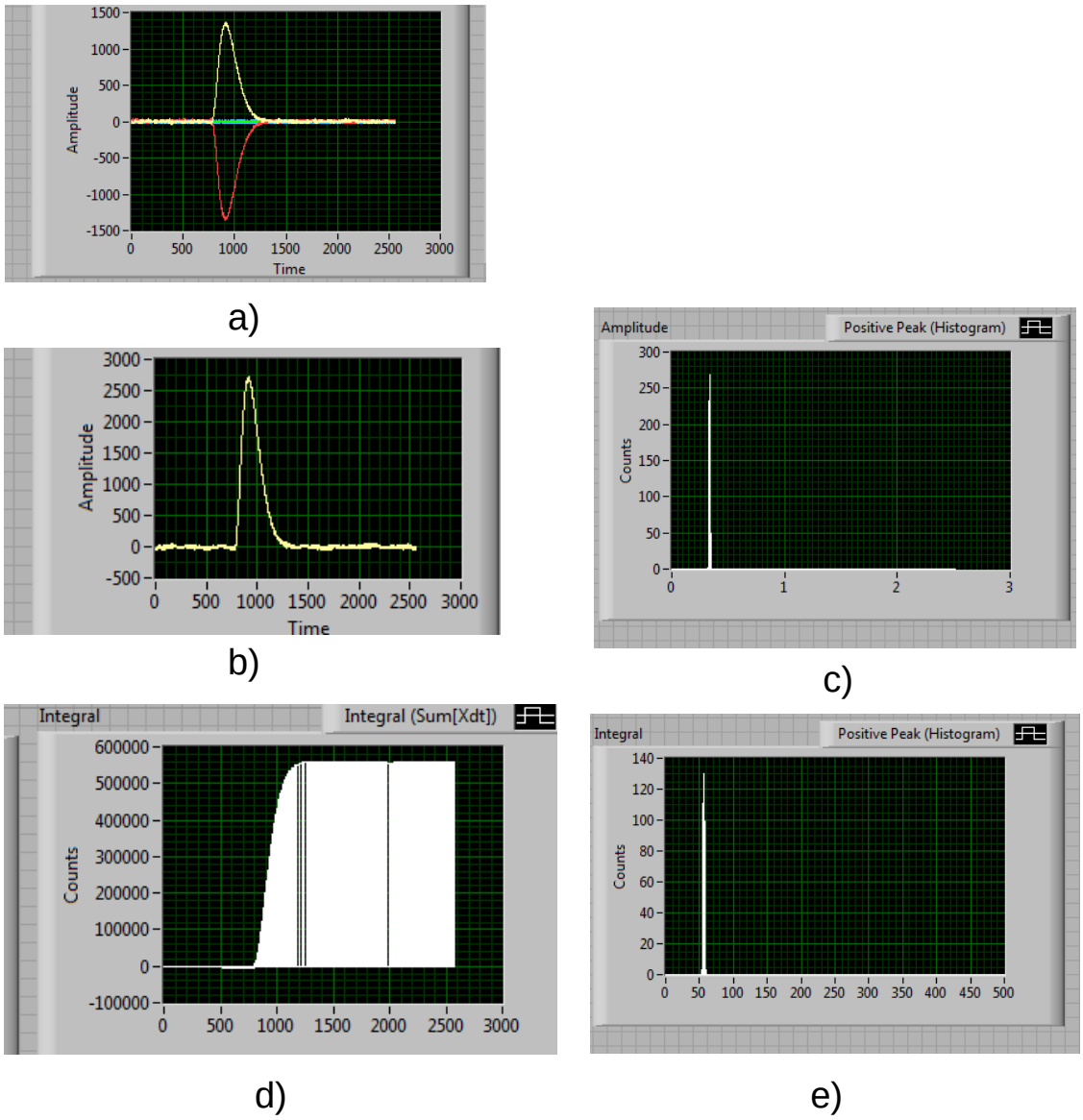

Figure 4.5: The procedure used to obtain the amplitude and integral values. a) The two single-ended signals. b) The differential signal. c) Histogram of the amplitude of the differential signal. d) Integral of the differential signal. e) Histogram of the integral.

Results and Discussion

Ideally for a given input signal, if the output pulses are identical, the bunch sizes of both the blue and green data points in figure 4.6 would be infinitesimal and all the pulses would have exactly the same amplitude and integral. Any variation in either one or both of the parameters would result in a broadening of the bunch sizes.

As the amplitude of the output signal increases (by increasing the input charge) one would expect the integral (the area of the pulse) to increase as well, otherwise it would mean that the pulse was getting narrower. If the increase is linear the gain of the amplifier is also linear. Moreover, if the ratio of area over amplitude is constant, one can confirm that the pulse shape is stable.

The pulse shape stability for channel 1 of NCB1 at low gain is illustrated in figure 4.6. All channels of all the carrier boards showed similar results, so for convenience only this one is shown here. The rest of the pulse shape stability results are shown in appendix A. The circular blue data points show the area (integral) of the output pulses, and the triangular green data points show the ratio of amplitude and area, both as a function of amplitude.

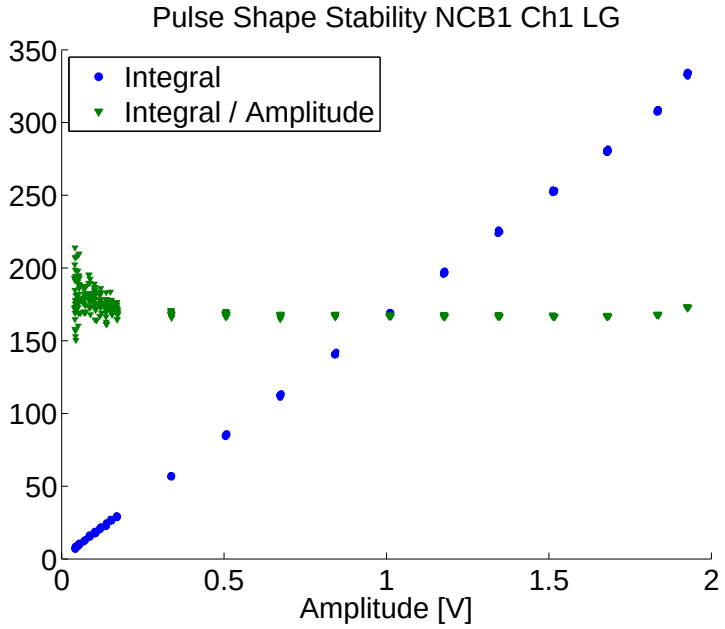

Figure 4.6: Pulse shape stability for channel 1 of NCB1 at low gain.

Compared to the ideal case described above, the results agree to some extent, having the integral increase linearly with the amplitude and having somewhat small bunch sizes over the full range input charges. Moreover, the ratio of area over amplitude is constant, which confirms a stable pulse shape and gain linearity of the chip. The bunch sizes increase at lower amplitudes as seen in figure 4.7. This is a result of the signal-to-noise ratio (SNR) being poor for small output signals. At very large amplitudes the linearity deteriorates as a result of the amplifier saturating. As an example, details regarding the integral calculation for a 40 mV and 400 mV output

signal amplitude are shown in appendix G.

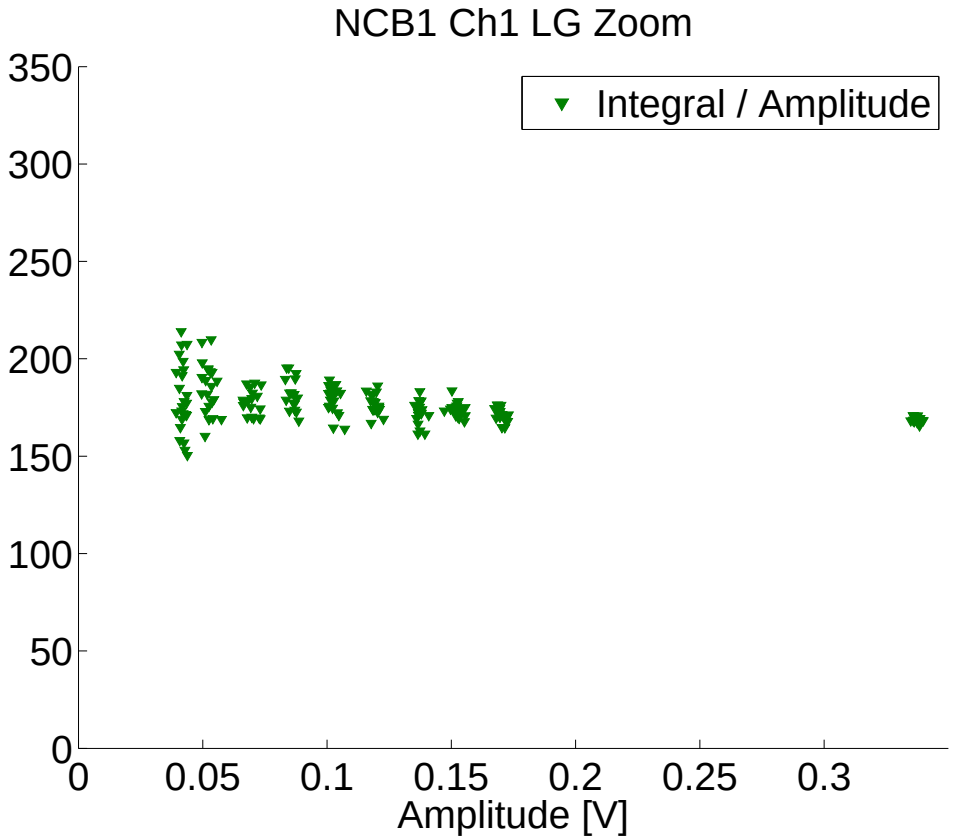

Figure 4.7: A closeup of channel 1 of NCB1 at low gain. The signal to noise ratio is low for small input signals, broadening the ratio of Integral/Amplitude. For output amplitudes above ~200 mV the noise is no longer dominant and the ratio narrows down.

4.1.3 Crosstalk

Crosstalk is a phenomenon by which a signal transmitted through one channel of a transmission system creates an undesired signal in another. It is usually caused by capacitive, inductive or conductive coupling between channels.

The ALICE TDR [11] states that the crosstalk between adjacent channels has to be kept below 0.2 %. Therefore, a crosstalk test was done to see if this requirement is met by the SAMPA Chip 1. The test was performed by injecting an input charge which produced the maximum output signal (without clipping) so the crosstalk would be at its highest and therefore easiest to measure. The test setup for the crosstalk measurement is listed below:

- Input signal: Ramp, 100% symmetry
- Signal amplitude low gain: 110 mV_{PP}
- Signal amplitude high gain: 70 mV_{PP}
- Trigger: Sync output of the signal generator
- Signal readout: Oscilloscope

The experimental test setup for the crosstalk measurement is shown in figure 4.8. Since the amplitudes of the crosstalk signals were low, the sync output of the signal generator was used as trigger, otherwise the crosstalk wasn't visible on the oscilloscope. To reduce noise the SAMPA chips were placed inside a Faraday cage. No difference in noise was measured when closing the Faraday cage, so for convenience it was left open throughout the test.

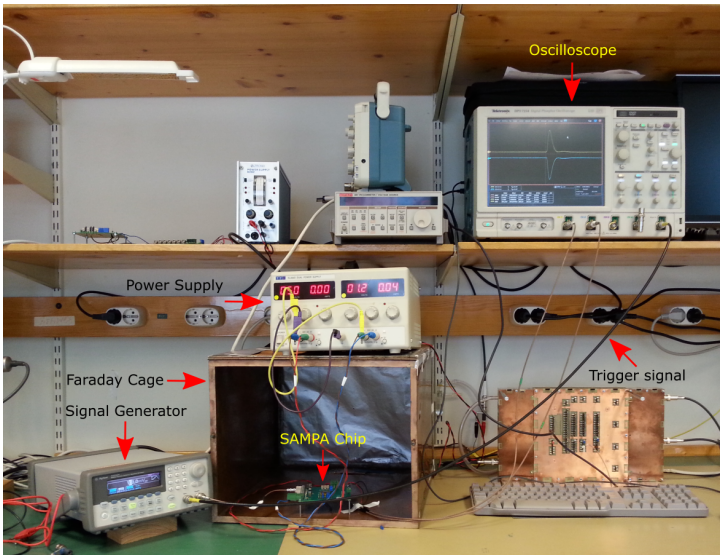

Figure 4.8: The experimental test setup used during the crosstalk measurement.

Five oscilloscope screenshots of the crosstalk test are shown in figure 4.9. In this case the input signal was injected into channel 2. The two topmost figures show the most adjacent channels, channel 1 (a) and 3 (b). Channel 2 is shown in the middle (c), and the channels furthest away, channel 4 (d) and 5 (e), are shown at the bottom.

The crosstalk test was done for all four boards (OCB1, OCB2, NCB1 and NCB2) for both low and high gain. Prior to the test, the noise of each channel was obtained by measuring the peak-to-peak output amplitude with no input signal applied. The crosstalk was obtained by injecting the input signal into one channel at a time while measuring the peak-to-peak amplitude of all five channels. The noise was quadratically subtracted and the relative crosstalk for each channel was calculated. The relative crosstalk in percent is given by equation 4.1.

$$XT_{Relative} = \frac{\sqrt{A_{CN}^2 - A_{Noise\_N}^2}}{\sqrt{A_{CI}^2 - A_{Noise\_I}^2}} \times 100\ \% \quad , \tag{4.1}$$

where A_{CN} is the peak-to-peak amplitude and A_{Noise_N} is the measured noise in the neighboring channel. A_{CI} is the peak-to-peak amplitude and A_{Noise_I} is the measured noise in the injected channel.

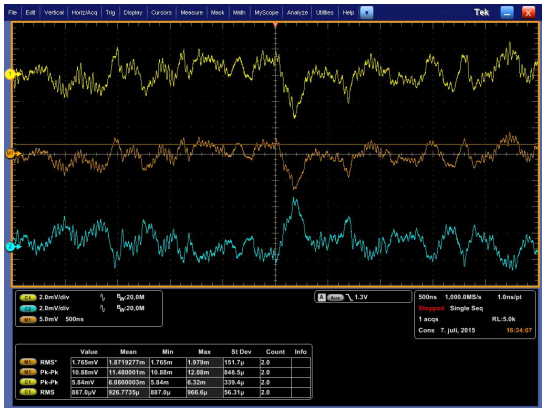

(a) Channel 1

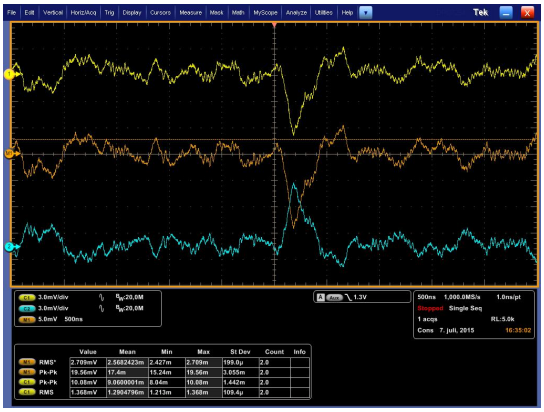

(b) Channel 3

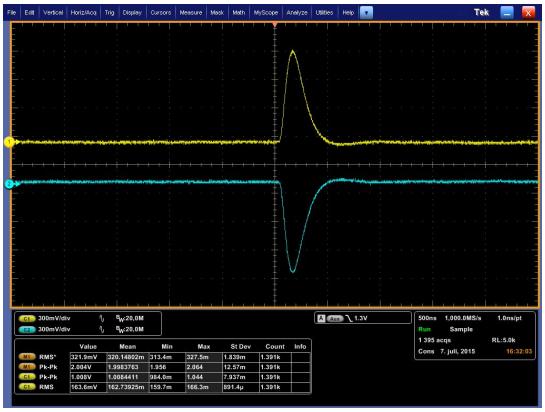

(c) Channel 2

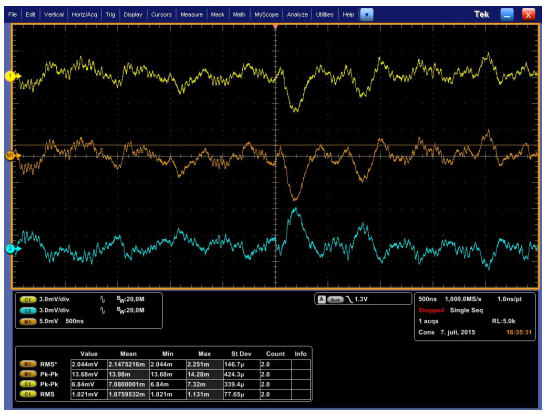

(d) Channel 4

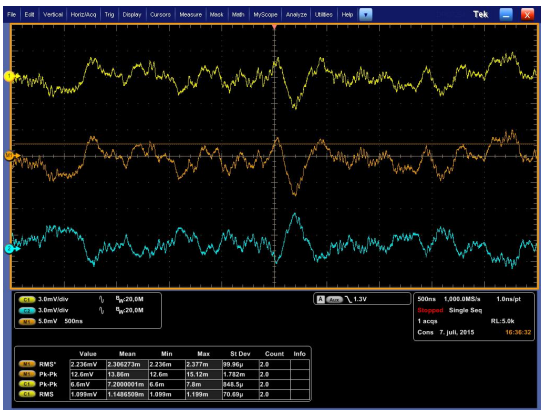

(e) Channel 5

Figure 4.9: An example of the crosstalk measurement procedure. The signal was injected into channel 2 and the peak-to-peak amplitude of the signals in the neighboring channels (top figures) as well as the next neighbors (bottom figures) were measured.

Results and Discussion

The measured relative crosstalk (%) for the four carrier boards is summarized in table 4.2. The minimum, maximum and average crosstalk values are shown for both low and high gain, as well as the standard deviation of the average. Tables containing the raw-data used to obtain these results can be found in appendix D. The crosstalk results from all channels 1 of the SAMPA have been omitted from the table as they were defective and gave very high crosstalk values. This defect is further explained in appendix D.

Crosstalk [%]	Min.	Max.	Average	Standard Dev.
OCB1 LG / HG	0.24 / 0.49	0.56 / 1.29	0.34 / 0.80	0.09 / 0.26
OCB2 LG / HG	0.28 / 0.24	0.57 / 0.67	0.38 / 0.42	0.08 / 0.15
NCB1 LG / HG	0.28 / 0.38	0.74 / 0.91	0.48 / 0.52	0.13 / 0.17
NCB2 LG / HG	0.90 / 0.77	1.38 / 1.44	1.12 / 1.05	0.14 / 0.22

Table 4.2: Crosstalk in percent for the four carrier boards.

The average crosstalk varies between roughly 0.3 % and 0.8 %, except for NCB2 where it reaches 1.12 %. Due to the deviation measured for NCB2, the test was repeated, but no improvement was measured. Despite the new carrier boards being designed to have better crosstalk performance than the old ones, they seem to perform worse. This might be a result of the increased track length on the carrier board due to the embedded differential buffer.

On average the SAMPA chips don't fulfill the requirement of less than 0.2 % crosstalk. The crosstalk performance should be taken into consideration when designing the second version of the SAMPA chip

4.1.4 Noise

A noise test was done to see if the SAMPA chip fulfills the ALICE TDR requirements shown in table 2.1. It states that the system noise[2] should be less than 670 ENC[3] and the PASA (preamplifier and shaper currently used in the ALICE TPC) noise should be less than 385 ENC for 12 pF input capacitance.

The test was done by measuring the noise at the output of the carrier boards with no input signal applied. Two carrier boards were tested, OCB1 and NCB1, at both high (30 mV/fC) and low (20 mV/fC) gain. They were placed inside the Faraday cage to reduce ambient noise. The test setup is shown in figure 4.10.

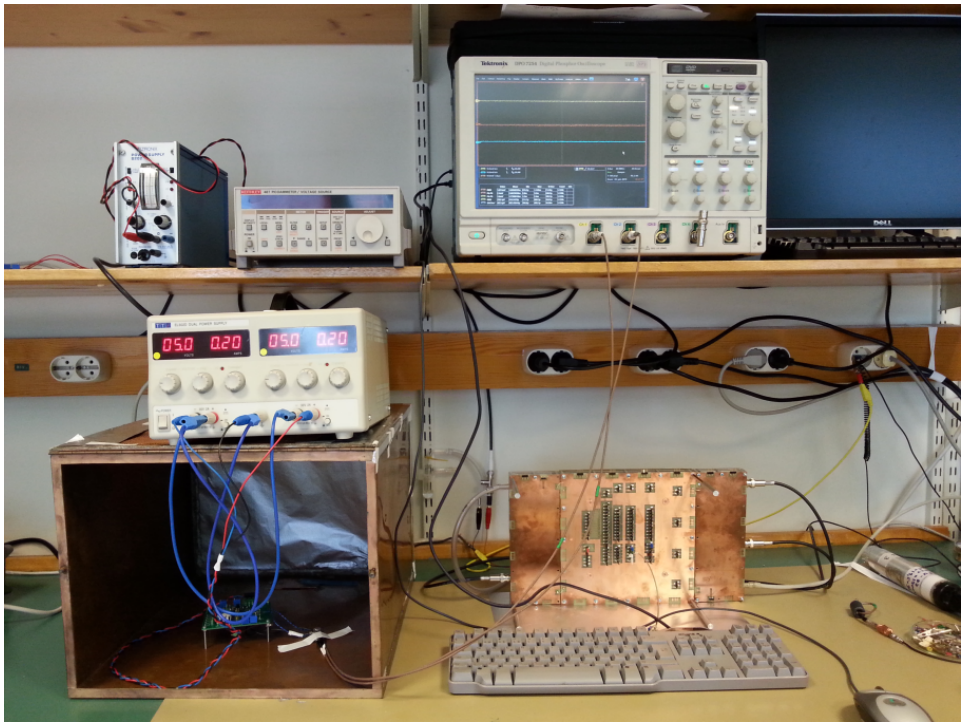

Figure 4.10: The setup used during the noise measurement test.

The SAMPA noise is a function of the input capacitance of the chip; increasing the input capacitance increases the noise (see appendix B). Therefore, the input of the chip was loaded with eight different capacitor values while measuring the noise. The values used were: 1, 4.7, 10, 18, 22, 33, 47 and 68 pF.

The background noise of the system (oscilloscope, cables and carrier board) was obtained by turning off the carrier board's power supply and measuring the noise at the output of the board. All cables were connected while measuring the background noise to include all noise contributions. To calculate the actual chip noise the back-

[2] The system noise includes the preamplifier, shaper, ADC, effects of input capacitance and contributions from the PCB design.

[3] Equivalent Noise Charge. The noise calculated at the input of the amplifier in units of the electron charge (1.6×10^{-19} C).

ground noise was quadratically subtracted from the noise measured while the carrier boards were powered on but without any capacitors connected.

The positive and negative outputs of the carrier boards were connected to the oscilloscope for noise readout. A math function of the oscilloscope was used to calculate the differential signal by subtracting the two inputs from each other. Then the RMS (Root Mean Square) value of the differential signal was measured, and the mean value of this gave the noise.

The SAMPA chip was tested at different facilities (Bergen, Oslo, Dubna and São Paulo) at the same time. To be able to compare results it was agreed upon to have a standard set of oscilloscope settings for noise testing. These are listed below:

- Sampling rate: 50 MS/s
- Time division scale: 5 µs
- Voltage division scale: 10 mV
- Bandwidth: 20 MHz

A screenshot of the oscilloscope during the noise test is shown in figure 4.11. It illustrates the settings used and the parameters measured. The mean value of the RMS noise is the counting average of the measured RMS value. The number of counts in the average is shown in the second to last column at the bottom in the figure. Before the noise values were noted down, the number of counts in the average was allowed to reach a few hundred. This was done to ensure that the measured noise values were accurate. A Gaussian distribution of the differential noise was plotted using an embedded function of the oscilloscope. It is shown to the left in the figure by the differential signal.

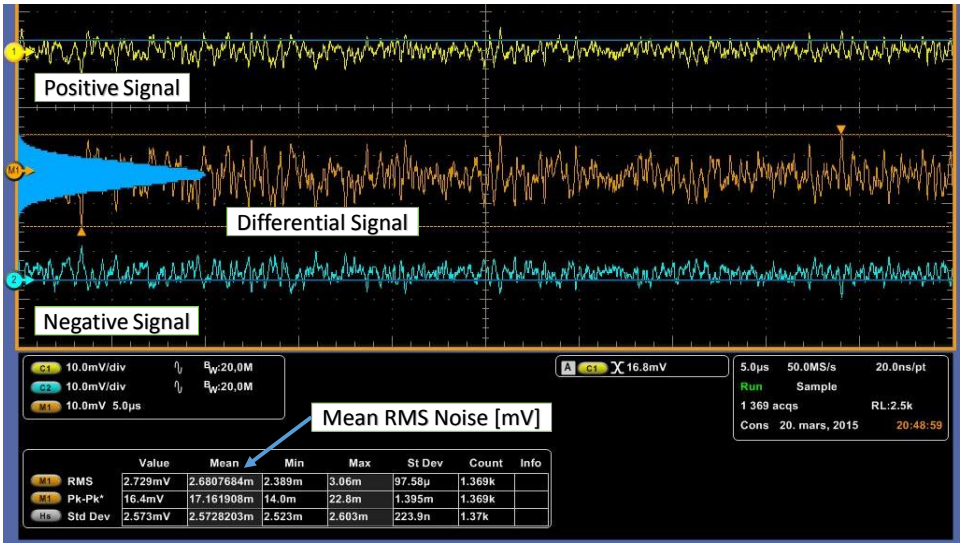

Figure 4.11: An oscilloscope screenshot showing the settings and the procedure used to measure the noise.

Results and Discussion

The noise measurement results are shown in figures 4.12 and 4.13. The horizontal axises are given in units of capacitance (pF) and the vertical in units of ENC (Equivalent Noise Charge). The ENC value of the noise is calculated using equation 4.2

$$ENC = \frac{RMS\ Noise\ [mV]}{Gain\ [mV/fC] \times e\ [C]} \tag{4.2}$$

where e is the electron charge ($1.6 \times 10^{-19}\ C$) and *RMS Noise* is the measured noise using the oscilloscope.

The plus-signed data points with a continuous line (black) and the dashed curve (also black) show simulated noise results for the SAMPA ASIC. The dashed line includes 500 µV of power supply noise (V_{DD}). The simulations were done by the chip designer in Brazil. The other five curves (colored) show the measured noise results for all five channels of the chip.

From the figures to the left it is seen that the measured data does not match the simulation. A possible reason for this discrepancy could be that the stray capacitances of the carrier board (input connectors, tracks, etc.) had not been considered. Because of these capacitances, the noise values do not correspond to the capacitance of the applied capacitors, but rather to the sum of the applied capacitor and the stray capacitance of the board. The stray capacitances were measured using a capacitance meter and are shown in table 4.3. The SAMPA chips were not connected to the boards during the measurement, hence the package capacitance of the SAMPA IC was not included in the results. The capacitance contribution from the IC package is unknown. Since OCB1 has LEMO connectors at the input (see figure 2.4a) the input capacitance is greater than for NCB1 which uses pin-type connectors.

Channel	1	2	3	4	5
OCB1 [pF]	15.3	14.2	12.0	13.1	12.8
NCB1 [pF]	4.80	4.00	3.53	4.09	4.80

Table 4.3: The input capacitance of the five channels of OCB1 and NCB1.

The plots to the right are corrected for the stray capacitance using the values shown in table 4.3. After implementing this correction the difference between the measured and simulated curves was reduced significantly.

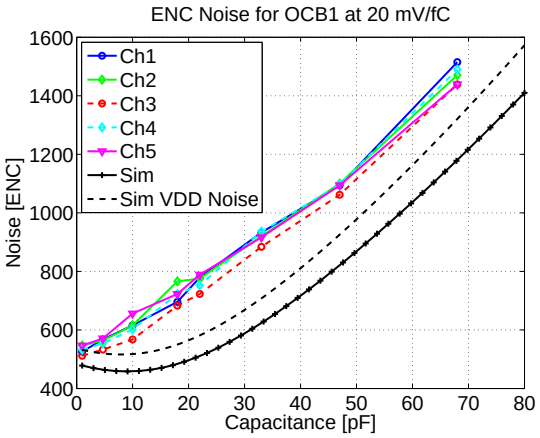

(a) Uncorrected noise OCB1 at low gain.

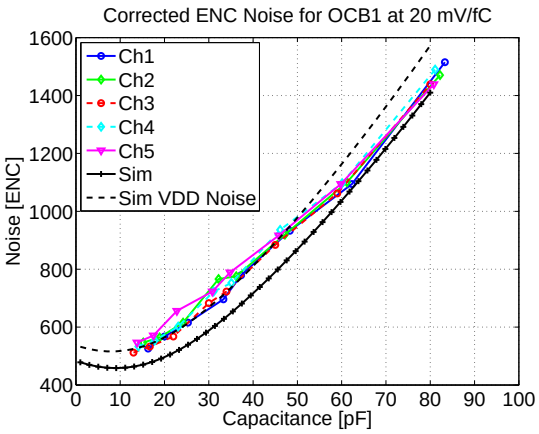

(b) Corrected noise OCB1 at low gain.

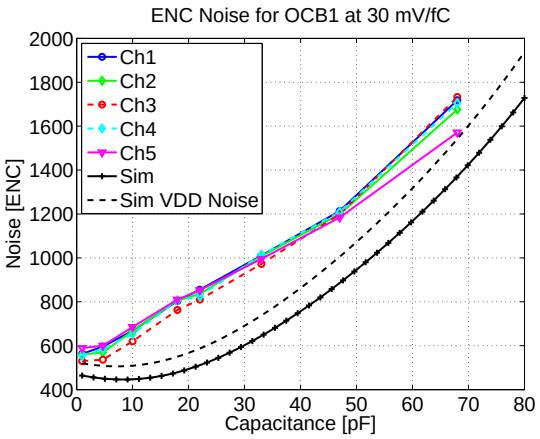

(c) Uncorrected noise OCB1 at high gain.

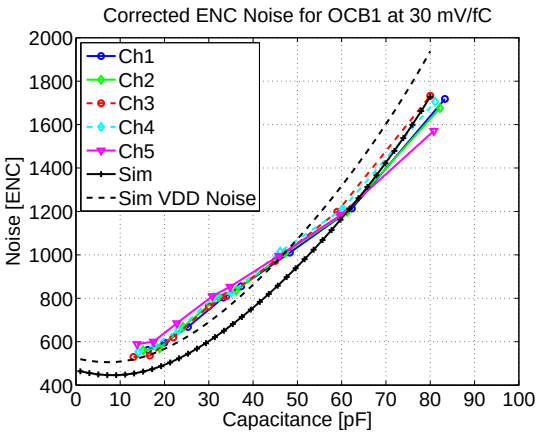

(d) Corrected noise OCB1 at high gain.

Figure 4.12: Noise results for Old Carrier Board 1 (OCB1).

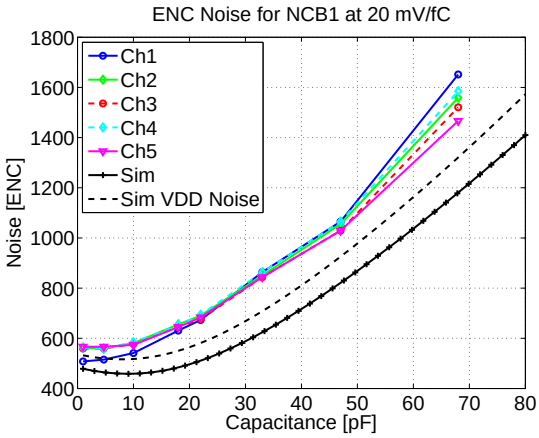

(a) Uncorrected noise NCB1 at low gain.

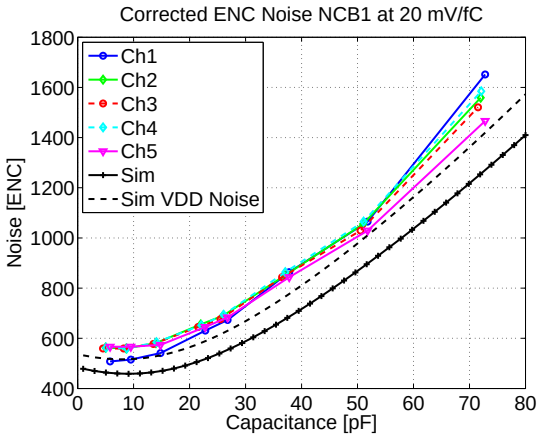

(b) Corrected noise NCB1 at low gain.

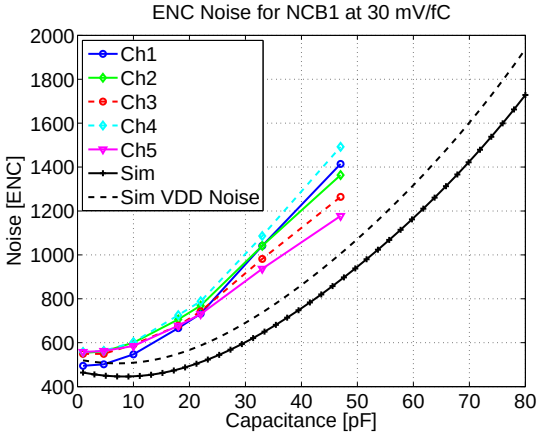

(c) Uncorrected noise NCB1 at high gain.

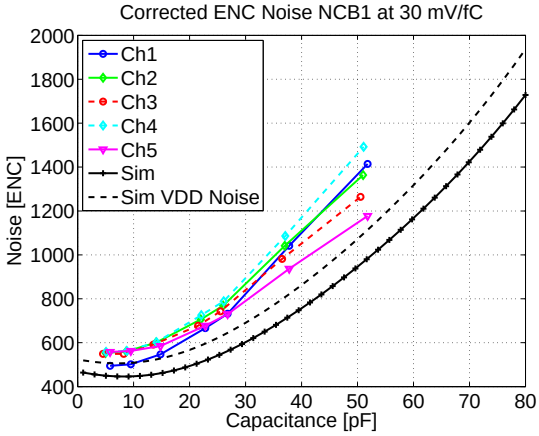

(d) Corrected noise NCB1 at high gain.

Figure 4.13: Noise results for New Carrier Board 1 (NCB1).

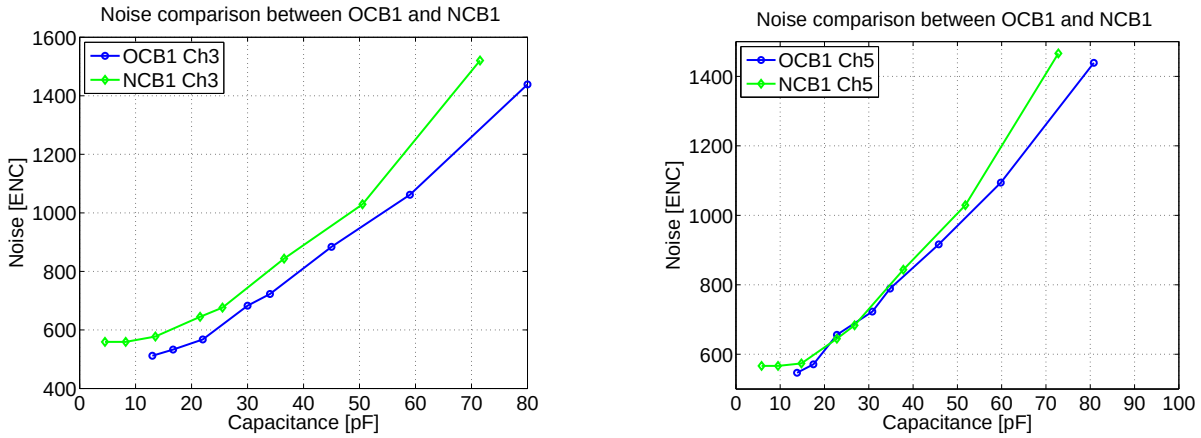

(a) (b)

Figure 4.14: Noise comparisons between channel 3 (a) and 5 (b) of OCB1 and NCB1.

The noise measurements agree to some extent with the simulated values, especially when the stray capacitances of the carrier boards are taken into account. A noise comparison for OCB1 and NCB1 is shown in figure 4.14. (a) shows the worst case scenario (channel 3) where the noise performance of the two carrier boards differs the most, while (b) shows the best case (channel 5) where they are the most similar. This illustrates that for some channels the two carrier boards perform equally well, while for others they do not.

According to table 2.1 the measured noise of the PASA chip currently being used in the ALICE TPC is 385 ENC at 12 pF input capacitance. This is also the requirement for the analog part of the SAMPA chip (Chip 1) during LHC Run 3. At 12 pF capacitance the simulated noise is 460 ENC, which suggests that the noise performance of the SAMPA chip has to be improved on the transistor level.

The simulated noise at low gain of the SAMPA Chip 1 with 15 pF input capacitance is 470 ENC (533 with 500µV V_{DD}. The best case measurement of OCB1 at low gain with the same capacitance is 512 ENC, while it is 541 ENC for NCB1. Even with the improvements made to the layout of the new carrier board (shorter leads, etc.) the noise performance wasn't improved. This further suggests that the SAMPA ASIC itself is the source of the noise, and that improvements have to be made on it to achieve the goal of 385 ENC at 12 pF.

4.2 SAMPA Tests With GEM Detector Prototype

In this section the SAMPA Chip 1 test results using the GEM detector prototype are discussed, see section 3.8. The tests are done to verify the performance of SAMPA Chip 1 under similar conditions to which it will face in the upgraded ALICE TPC during LHC Run 3 / Run 4 beyond year 2018.

Fe-55 and Sr-90 were used to initiate the processes of excitation and ionization inside the GEM detector. As described in section 3.3 the photons emitted by the Fe-55 interact with the detector gas through the photoelectric effect, while the electrons emitted by the Sr-90 interact as MIPs through inelastic scattering from atomic electrons. The experimental setup for the test is shown in figure 4.15.

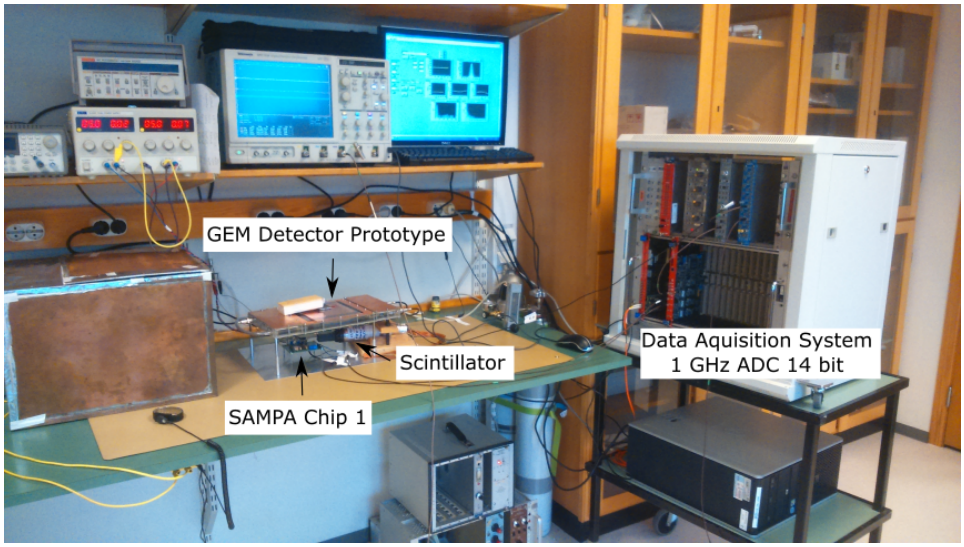

Figure 4.15: The GEM detector test setup.

The output of the SAMPA Chip was connected to the ADC input and the digital data was analyzed and stored using LabView. During the experiment channel two of the SAMPA chip at low gain was used. The GEM detector settings were as follows:

- GEM Voltages: 297 V
- Gain: ~2000
- Gas Type: Ne-CO_2-N_2 (90-10-5)
- Gas Flow Rate: 3 *l/h*

4.2.1 Gain Calibration Using Fe-55

The upgraded GEM based ALICE TPC will be operated at a detector gain of 2000. The following procedure is used to reach this gain in the GEM detector prototype.

According to equation 3.2 the gain of the detector can be obtained using three parameters, namely the anode current (I_{Anode}), the pulse rate (R) and the number of primary ionizations (N_{Prim}). The calculation to obtain the number of primary ionizations (165) in Ne-CO_2-N_2 (90-10-5) is reviewed in appendix F. The gain for the GEM detector prototype is:

$$G_{Eff} = \frac{60\ pA}{1.6 \times 10^{-19}\ C * 165 * 1.1\ kHz} \approx 2000\ mV/fC \tag{4.3}$$

The anode current and pulse rate have to be measured at the same time to get a correct gain calculation. To find the Fe-55 pulse rate the SAMPA chip was connected to the GEM detector ($30 \times 30\ mm^2$ pad), and the output pulse frequency (1.1 kHz) of the chip was measured using the oscilloscope. At the same time a picoammeter was connected to the anode pad through a capacitor to measure the anode current (60 pA.).

4.2.2 Energy Resolution Using Fe-55

The energy resolution is one of the most important properties of a detector. It quantifies how well the detector can resolve particle energies.

The Fe-55 source emits photons of energies 6.50 keV (K_α), 5.9 keV (K_β) with 24.4 % and 2.86 % probability, respectively [8]. These low energy photons give a very clear energy spectrum (see figure 4.17b), hence the Fe-55 source is used to verify the energy resolution of the detector. For Fe-55 self-triggering had to be used because the photons emitted by the source lose all their energy inside the detector.

A screenshot of the LabView setup used during an Fe-55 spectrum measurement is shown in figure 4.16. The signals coming from the ADC are shown in the window labeled "Raw Signals". They have an offset which is subtracted using a LabView VI and the resulting signals are displayed in the two topmost windows to the right. Then these two signals are subtracted from each other, and the differential signal is shown in the bottom right window.

The noise distribution is obtained by filling the baseline fluctuations of the differential signal in a histogram. Similarly, the pulse height spectrum is obtained by filling the pulse amplitudes of the differential signal in a histogram. The Data Acquisition (DAQ) settings (thresholds, offset values, sampling frequency, etc.) are shown in the windows marked by "DAQ settings".

The pulse height distribution shown in figure 4.17 is used to obtain the energy resolution of the detector. The relative energy resolution is defined as the ratio of sigma (σ) and the mean value (E) of the distribution. These two parameters are obtained by fitting a Gaussion function (red curve) to the pulse height distribution. The mean value corresponds to the maximum energy of the photon, and σ is the full-width-half-maximum (FWHM) multiplied by 2.35.

Figure 4.17a shows a pulse height distribution for Fe-55 using a discrete component preamplifier designed at the Wigner institute in Budapest. The DAQ settings for this particular measurement are discussed in appendix C. For comparison, a distribu-

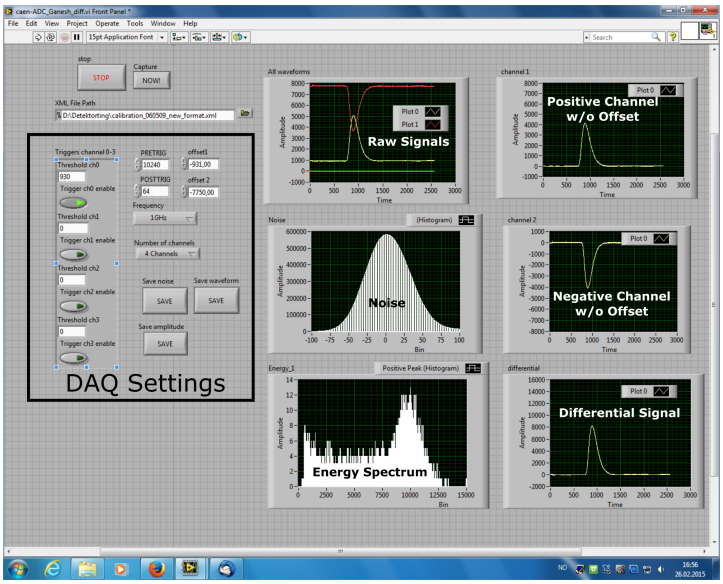

Figure 4.16: A screenshot of the LabView setup.

tion using the SAMPA Chip 1 is shown in figure 4.17b. The relative resolutions of the two plots are 7.95 % and 8.76 % for the discrete and SAMPA preamplifiers, respectively. Both measurements were done for the large (30×30 mm^2) anode pad of the detector.

Figure 4.17c shows a pulse height spectrum using the SAMPA chip for the 6×15 mm^2 pad. Compared to the large pad the resolution is worse. This is probably because of the signal amplitude from the small pad is lower than from the large pad (because less of the electron avalanche cloud is collected), resulting in a lower signal-to-noise ratio. It is commonly said that if the GEM detector resolution is less than 12 % for Fe-55 then the performance is satisfactory.

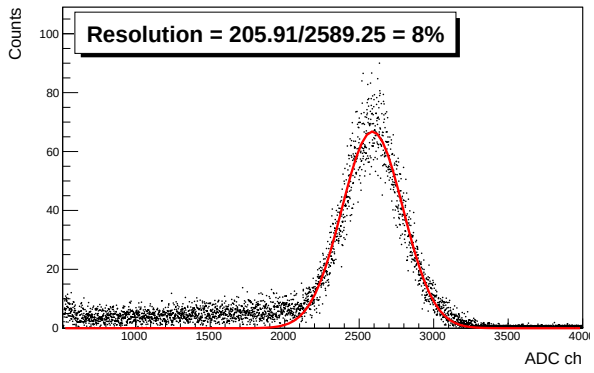

(a) 30 × 30 mm^2 pad.

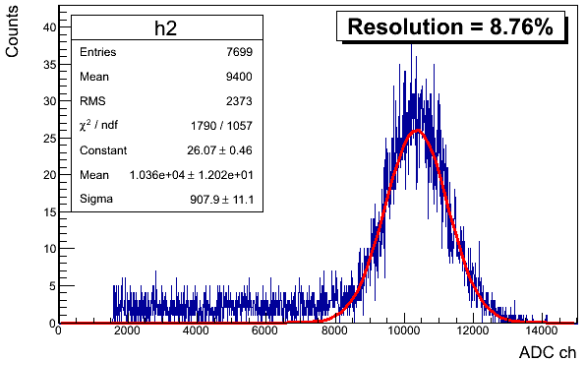

(b) 30 × 30 mm^2 pad.

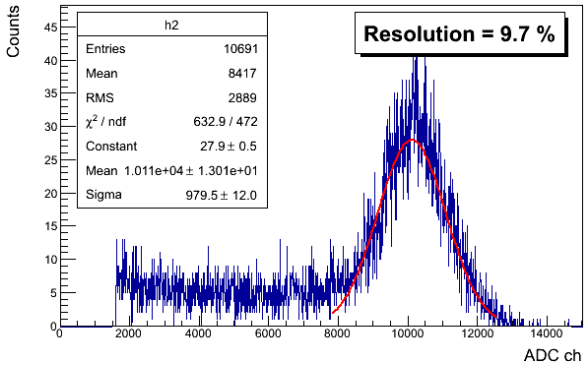

(c) 6 × 15 mm^2 pad.

Figure 4.17: a) An Fe-55 energy spectrum read out from the large pad (30 × 30 mm^2) using a discrete component preamplifier designed in Budapest. b) A comparison spectrum from the same pad as in a) using the SAMPA chip as amplifier. c) An energy spectrum using the SAMPA chip for the medium pad (6 × 15 mm^2)

4.2.3 Signal-To-Noise Ratio Using Sr-90

According to the ALICE TPC TDR the SNR requirement for MIPs (see table 2.1) is 30:1 for Outer Readout Chamber (OROC) pad sizes ($6 \times 10\ mm^2$ and $6 \times 15\ mm^2$) and 20:1 for Inner Readout Chamber (IROC) pad sizes ($4 \times 7.4\ mm^2$), both at 2000 gain and for 670 ENC system noise at 18.5 pF input capacitance.

To verify the above mentioned SNR requirement for MIPs, the Sr-90 source was used. The decay product of Sr-90 (Y-90) emits 2.28 MeV electrons. Since this energy is high the β-particles pass through the detector by minimum ionization. Therefore, Sr-90 was used for verification of signal-to-noise ratio (SNR) for Minimum Ionizing Particles (see section 3.3.3).

The experimental setup for the test is similar to the one used in the Fe-55 measurement (figure 4.15), except the triggering system. The electrons emitted by Sr-90 are MIPs and penetrate through the GEM detector. Therefore, a plastic scintillator was placed beneath the GEM detector (see figure 4.18, left) and its signals were used to trigger the DAQ (right).

The scintillator signal was fed through a discriminator with a threshold of ~0.5 MeV. The procedure of obtaining the threshold of ~0.5 MeV is as follows: The Sr-90 source was placed directly on top of the scintillator and the amplitude of the signal (mV) was measured. This signal amplitude corresponds to the maximum β-energy of ~2.28 MeV, and 25 % of this value was used to set the discriminator threshold by assuming an energy loss of ~0.5 MeV through the detector. During the experiment channel two of the SAMPA chip at low gain was used and the GEM settings were the same as for the Fe-55 tests.

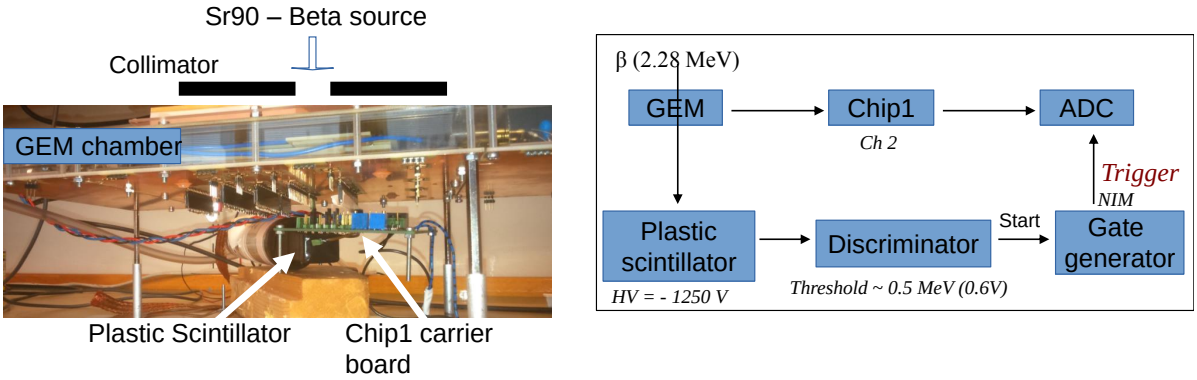

Figure 4.18: Left: The GEM detector output is connected to Chip 1 and the scintillator is placed beneath it. Right: Trigger schematic. The scintillator signal was fed through a discriminator with a threshold of 0.5 MeV.

A collimator of 3 mm diameter was used to focus the Sr-90 beam onto the segmented pads of the anode (see figure 3.11) There are four different pad sizes: (1) large pad - $30 \times 30\ mm^2$, (2) medium pad - $6 \times 15\ mm^2$, (3) small pad - $6 \times 10\ mm^2$ and (4) tiny pad - $4 \times 7.5\ mm^2$. The energy distribution of MIPs has been obtained for three different pad sizes, namely large, medium, and the sum of three medium

pads as shown in figure 4.19. To obtain the signal information the pulse height distributions were fitted using a Landau function (red curve). The Maximum Probable Values (MPV) obtained using the fit are in ADC channels. They are converted into voltage by multiplication with the quantization value of the ADC (0.125 mV)[4] and can be further converted into ENC: MPV divided by the gain of the chip.

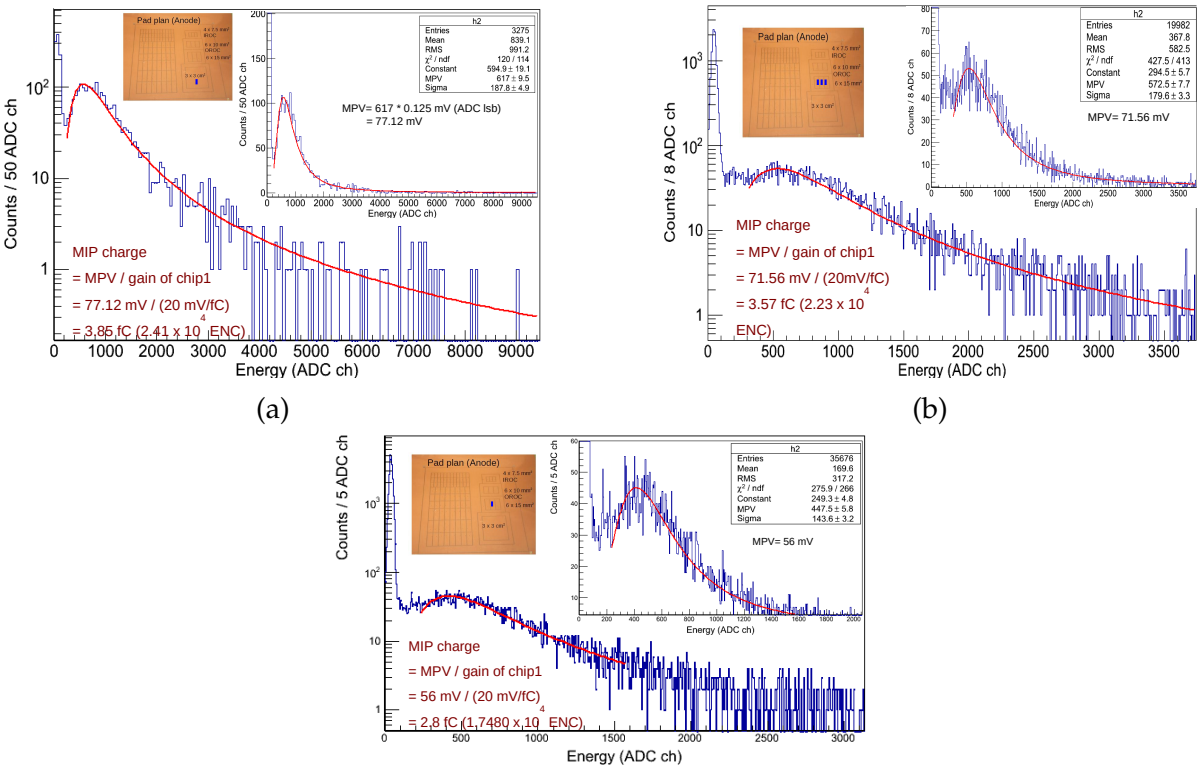

Figure 4.19: Sr-90 pulse height distributions. a) Large pad 30×30 mm^2. b) Sum of three medium pads 6×15 mm^2. c) One medium pad 6×15 mm^2. The distribution shown in the inset of the figures are plotted in linear scale and the position of the Sr-90 source during the measurements (marked with the blue rectangle) is shown with the inset picture of the anode plane. The red solid curves show the Landau fitted functions.

[4] The ADC has a dynamic range of 2 V and 14 bit resolution, which equates to 0.125 mV per ADC channel.

Signal

The signal-to-noise ratio for MIPs using the medium pad shown in figure 4.19c is calculated below as an example. Two values are needed for this calculation, the signal amplitude and the noise of the SAMPA chip. The amplitude is simply the MPV of the Landau distribution, which is approximately 450 ADC channels. This value is calculated in terms of voltage in equation 4.4.

$$MPV_{mV} = \sim 450\ ADC\ channels * 0.125\ mV/channel \approx 56\ mV \tag{4.4}$$

Then the equivalent input charge this voltage corresponds to is calculated in equation 4.5.

$$MPV_C = \frac{\sim 56\ mV}{20\ mV/fC} \approx 2.8\ fC \tag{4.5}$$

Finally, the MPV is calculated in terms of ENC by division og the electron charge, shown in equation 4.6.

$$MPV_{ENC} = \frac{20\ mV/fC}{1.6 \times 10^{-19}} = 17480\ ENC \tag{4.6}$$

Noise

To find the noise of the SAMPA chip, two measurements were done, one to obtain the total system noise (SAMPA chip, ADC and buffer) and the other to obtain the ADC-with-buffer noise. The latter is subtracted from the total system noise to get the actual noise of the SAMPA chip. From the measurements reported in section 4.1.4 it was concluded that the noise of the SAMPA chip increases with capacitance at the input. Therefore, to measure the total system noise the prototype detector was operational (HV powered on) and connected to the SAMPA chip, but without any radioactive source present to create signals. This included all the parasitic capacitances (GEM pad, readout pin, chip package and traces) measured to be ~12 pF. However, in the final ALICE TPC the SAMPA chips will be connected to the detector pad via kapton cables (see figure 1.4). These cables were not used during the experiment, and therefore the noise obtained in this test can be considered a best case measurement because the capacitance of the kapton cable will increase the chip noise.

The total noise was measured by connecting the second channel of the SAMPA chip to the buffer. Again a Gaussian function was fitted, and the total system noise is shown in figure 4.20a.

The noise of the ADC-with-buffer was measured by removing all jumpers connecting the SAMPA chip to the buffer. In this way only the noise generated by the buffer and ADC would be measured. The noise values were filled in a histogram and fitted with a Gaussian function, shown in figure 4.20b.

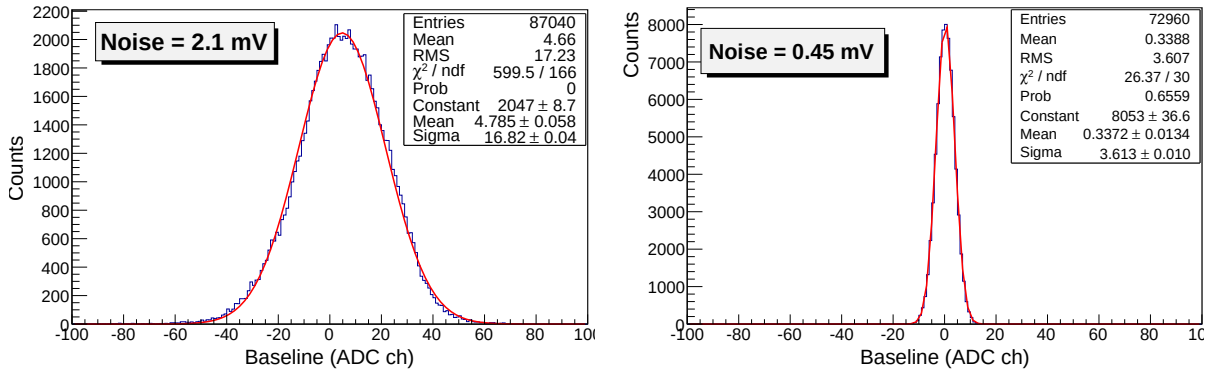

(a) (b)

Figure 4.20: Noise measurements for the signal-to-noise ratio calculations. (a) The total noise measured with the GEM detector prototype connected to the SAMPA Chip 1, including the ADC and buffer noise. (b) The measured noise from only the buffer and ADC without the SAMPA Chip 1 or detector connected.

The noise of the chip is obtained by quadratically subtracting the noise values found in figures 4.20a and 4.20b, shown in equation 4.7.

$$\begin{aligned} Noise_{SAMPA} &= \sqrt{\left(Noise_{System}\right)^2 - \left(Noise_{ADC+Buffer}\right)^2} \\ &= \sqrt{2.1^2 - 0.45^2} = 2.051\ mV = 641\ ENC \end{aligned} \tag{4.7}$$

Signal-to-Noise Ratio for MIPs (7 mm Drift Gap)

The noise requirement from the TDR of 670 ENC is for the entire data readout circuitry (Chip 3), including the preamplifier/shaper, ADC and data acquisition. In this section the signal-to-noise ratio (SNR) calculation is done only for the preamplifier/shaper circuitry. Therefore, it is fair to compare the SNR with the simulated noise of Chip 1 (see section 4.1.4) and not the system noise of 670 ENC. The values obtained by simulation are based on the requirement from the ALICE TPC TDR. The SAMPA Chip 1 simulated noise of 460 ENC is used in equation 4.8 to find the SNR requirement without ADC noise.

$$\begin{aligned} SNR_{Simulated} &= \frac{MPV_{ENC}}{Noise_{Simulation}} \\ &= \frac{17480}{460} = 38\ (33\ with\ V_{DD}\ noise\ of\ 500\ \mu V) \end{aligned} \tag{4.8}$$

Therefore, the SNR goal of this measurement should be 38:1 and not 30:1.

The SNR for MIPs measured in a 7 mm drift gap is obtained by dividing the MIP signal amplitude in equation 4.6 by the SAMPA chip noise in equation 4.7, as shown

in equation 4.9.

$$SNR_{Measured} = \frac{MPV_{ENC}}{Noise_{SAMPA}} = \frac{17480}{641} \approx 27 \tag{4.9}$$

By comparing equation 4.8 and 4.9 one can conclude that the SNR for the SAMPA Chip 1 doesn't meet the requirement. Moreover, by increasing the drift gap the signal-to-noise ratio would increase because the electrons would dissipate more of their energy in the sensitive part of the detector.

4.3 Conclusion

The SAMPA Chip 1 has been tested with a pulse shape generator and a GEM detector prototype. In the pulse shape generator several parameters of the chip were tested, including power consumption, gain and pulse shape stability, crosstalk and noise.

The power consumption varies with V_{DD}. At 1.25 V it is measured to be ~9 mW per channel and the requirement is less than 6 mW per channel. The gain and pulse shape stability was confirmed by obtaining the linear relation between the area and amplitude over different input charges (1 pF to 120 pF). At lower amplitudes (low input charges) the linearity deteriorated due to low signal-to-noise ratio. Four samples of the SAMPA Chip 1 were tested for crosstalk. Three of them show crosstalk between roughly 0.3 % and 0.8 %, while it reaches nearly 1.5% for the fourth. The requirement is less than 0.2 %. The noise is measured by loading the input with different capacitances (1 pF to 68 pF). The measured noise agrees to some extent with the simulated values, in particular when the stray capacitances of the carrier board are considered together with the load capacitance at the input of the chip. Most of the parameters discussed above don't meet the requirements mentioned in the ALICE TPC TDR for the SAMPA Chip 1. However, the pulse shape is stable and the gain is linear.

The chip is also tested using a GEM detector prototype to generate the input signals. These tests include energy resolution using Fe-55 and signal-to-noise ratio using Sr-90. An energy resolution of less than 12 % is said to be satisfactory, and the GEM detector resolution is measured to roughly 8 % The signal-to-noise ratio requirement for the analog part of the SAMPA chip (Chip 1) is 38:1. It has been measured to be 27:1. The requirement has not been met as a result of the noise performance of the Chip 1 being poor. Improving the noise performance of Chip 1 will increase the signal-to-noise ratio. A larger drift gap will also result in a better signal-to-noise ratio, since it results in a larger output signal.

Chapter 5

Summary and Conclusion

The Large Hadron Collider is the world's largest and most powerful particle accelerator. The ALICE detector, which is located at a point along its circumference, studies heavy-ion collisions to characterize strongly interacting matter at extreme energy densities. To accommodate the increased collision rates and -energies during Run 3 of the LHC in 2018 the signal readout of the ALICE TPC will be upgraded to a GEM based system, replacing the currently employed wire-chambers. This requires new front-end electronics, therefore a prototype SAMPA chip has been produced in 2014.

The first objective of this thesis has been to characterize the analog part of the SAMPA chip. This included testing the power consumption, gain and pulse shape stability, crosstalk and noise performance. The second objective was to test the SAMPA Chip 1 under realistic conditions using signals from a prototype GEM chamber.

A differential buffer was constructed to facilitate Chip 1 signal readout using an ADC, since the SAMPA cannot drive a 50 Ω load. The buffer did not negatively affect the performance of the SAMPA Chip 1, and signal readout through the ADC proved to be successful.

The power consumption test was conducted on the old carrier board (OCB1), since these have a separate power supply input for the SAMPA chip. The power consumption was measured to ~9 mW per channel at the nominal supply voltage of 1.25 V, which is roughly 50 % higher than the 6 mW requirement. Even for supply voltages as low as 1.18 V the power consumption was above the requirement, at ~8 mV per channel.

The gain and pulse shape stability test was done for all five channels of the two new carrier boards (NCB 1 and 2), at both low and high gain. Since the test required ADC readout, the old carrier boards could not be used. The results showed a stable pulse shape and linear gain across all channels/gain settings, except at very low and high input charges. The spreading of the cluster sizes at low input charges came as a result of the signal-to-noise ratio being poor for such small values. At high input charges the linearity deteriorated as a result of the Chip 1 saturating.

The crosstalk measurement showed scattered results, with the new carrier boards performing worse than the old ones, despite the emphasis that was made to improve their crosstalk performance. Especially NCB2 performed badly, having measured

crosstalk values in the 1 % range. The test was repeated for NCB2 to check the credibility of the test, but no improvement was measured. The overall average crosstalk ranged from roughly 0.3 % to 0.8 %, except for the NCB2 discrepancy of 1.1 %. None of the carrier boards fulfilled the crosstalk requirement of 0.2 %, the closest being OCB1 at low gain, achieving an average minimum of 0.24 %.

The noise measurement was conducted on all five channels of OCB1 and NCB1 at both low and high gain. The test results coincided to some extent to the simulated noise values when corrected for the stray capacitances of the carrier boards, especially when 500 µV of V_{DD} noise was added to the simulation. However, the simulated noise of the chip does not fulfill the requirement of 385 ENC at 12 pF capacitance, which suggests that the SAMPA design has to be improved on the transistor level to improve noise performance. The improvements made to the layout of the new carrier board failed to improve noise performance, further underlining that the problem stems from the SAMPA ASIC design itself.

A prototype GEM chamber was constructed in collaboration with the Hungarian research team stationed at the Wigner Institute in Budapest, Hungary. Two radioactive sources were used in conjunction with the GEM chamber to conduct measurements. Fe-55 was used for gain calibration and to measure the detector's energy resolution, while Sr-90 was used to obtain the signal-to-noise ratio of the SAMPA Chip 1. The gain was set to ~2000 by adjusting the GEM voltages while measuring the anode current and pulse rate. The energy resolution of the GEM detector has been measured to be ~8 %, which is considered satisfactory.

The signal-to-noise ratio for MIPs was measured using the Sr-90 source and a plastic scintillator as trigger. The requirement for Chip 1 is 38:1, and it was measured to be 27:1. The requirement has not been met as a result of the noise performance of the Chip 1 being poor. Improving the noise performance of Chip 1 will increase the signal-to-noise ratio. Increasing the drift gap of the detector will also increase the signal-to-noise ratio, since more of the particle's energy will be deposited in the sensitive part of the detector, creating a greater output signal.

There are a few issues with the current SAMPA chip which unfortunately limit its performance. These should be addressed in future designs.

- The noise performance of the Chip 1 is inadequate. Tests suggest that the problem stems from the internal design of the SAMPA ASIC. Improving noise performance will also increase the signal-to-noise ratio.
- The crosstalk performance fails to meet the requirement of less than 0.2 %. Altering the PCB layout of the SAMPA carrier board failed to improve crosstalk performance, suggesting that the problem comes from inside the SAMPA ASIC.
- The power consumption of the Chip 1 is currently 50 % above the requirement of 6 mW per channel. Again, the problem stems from the internal SAMPA ASIC.

Appendix A

Pulse Shape Stability

The pulse shape stability measurements for all channels of NCB1 and NCB2 at both low and high gain are shown in figures A.1 through A.3. All plots show similar trends, and the pulse shape is stable throughout.

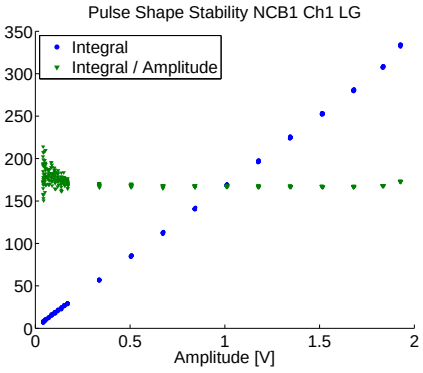

(a)

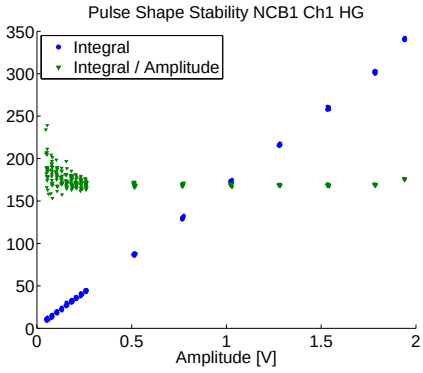

(b)

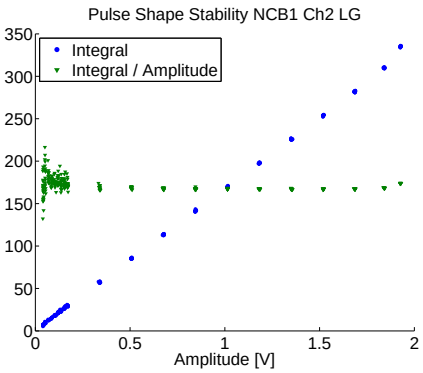

(c)

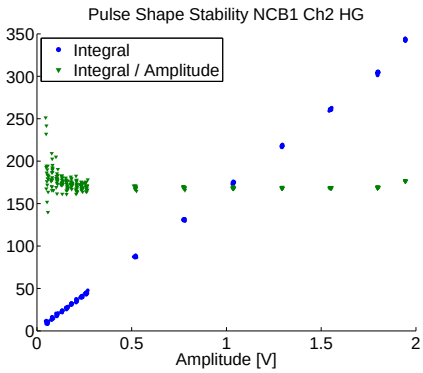

(d)

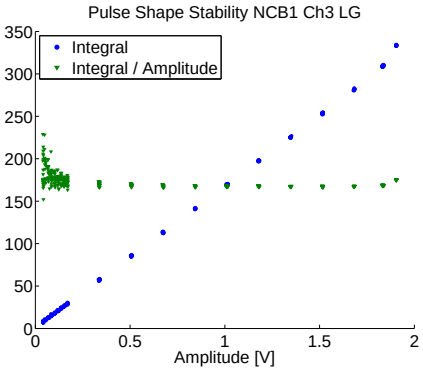

(e)

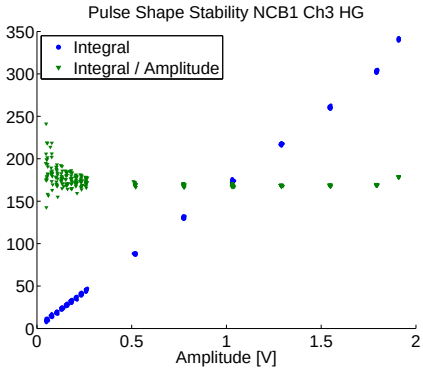

(f)

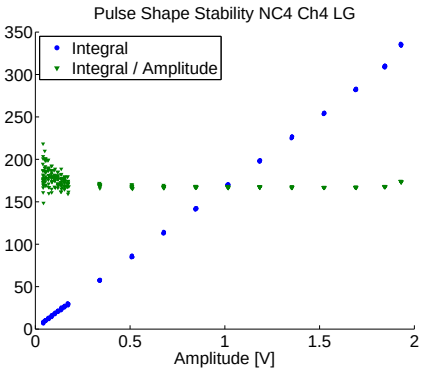

(g)

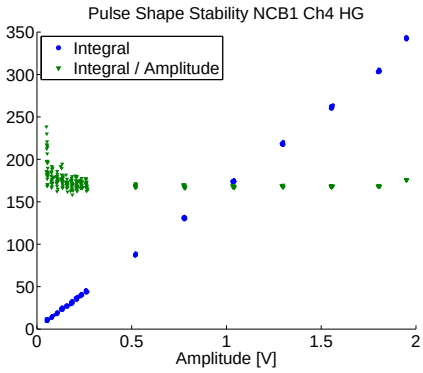

(h)

Figure A.1: Pulse shape stability measurement for NCB1 Channel 1 through 4 for low and high gain.

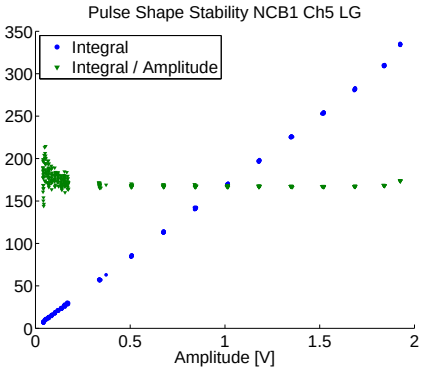

(a)

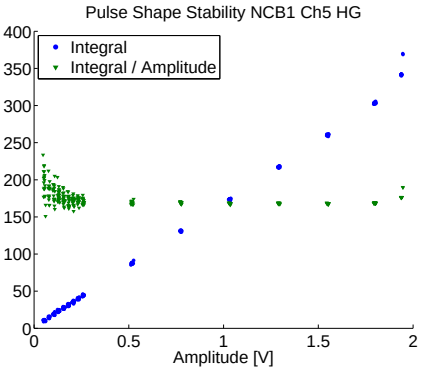

(b)

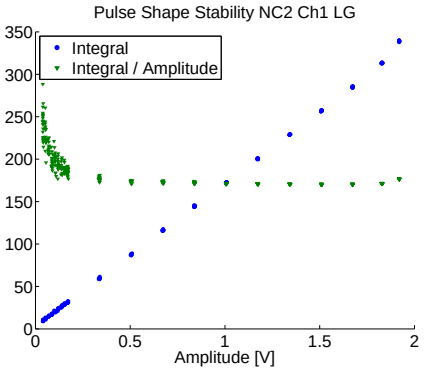

(c)

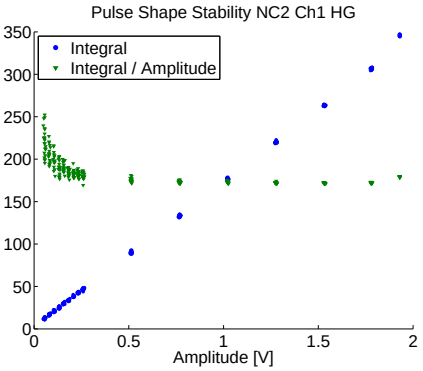

(d)

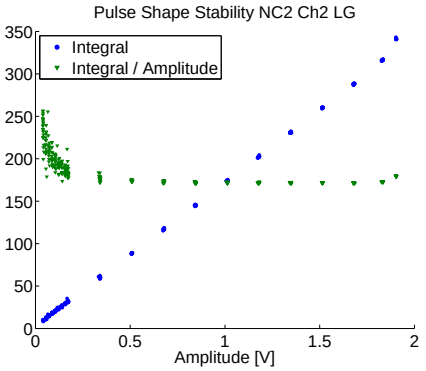

(e)

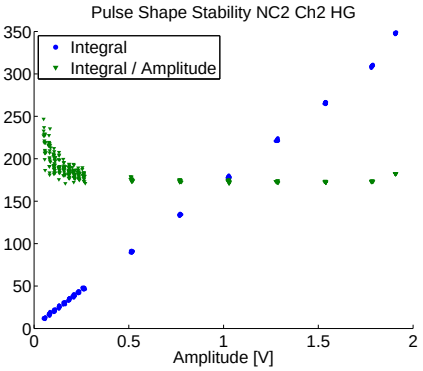

(f)

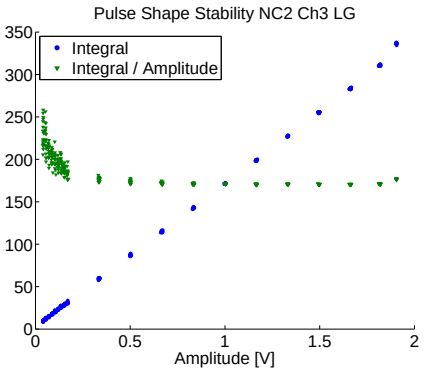

(g)

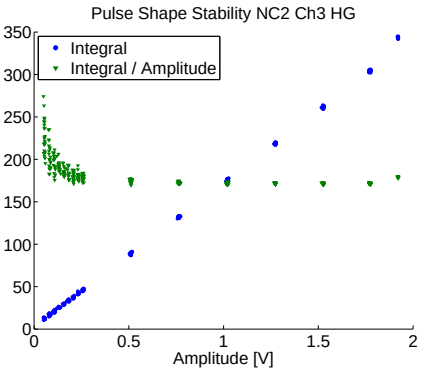

(h)

Figure A.2: Pulse shape stability measurement for NCB1 Channel 5 and NCB2 channel 1 through 3 for low and high gain.

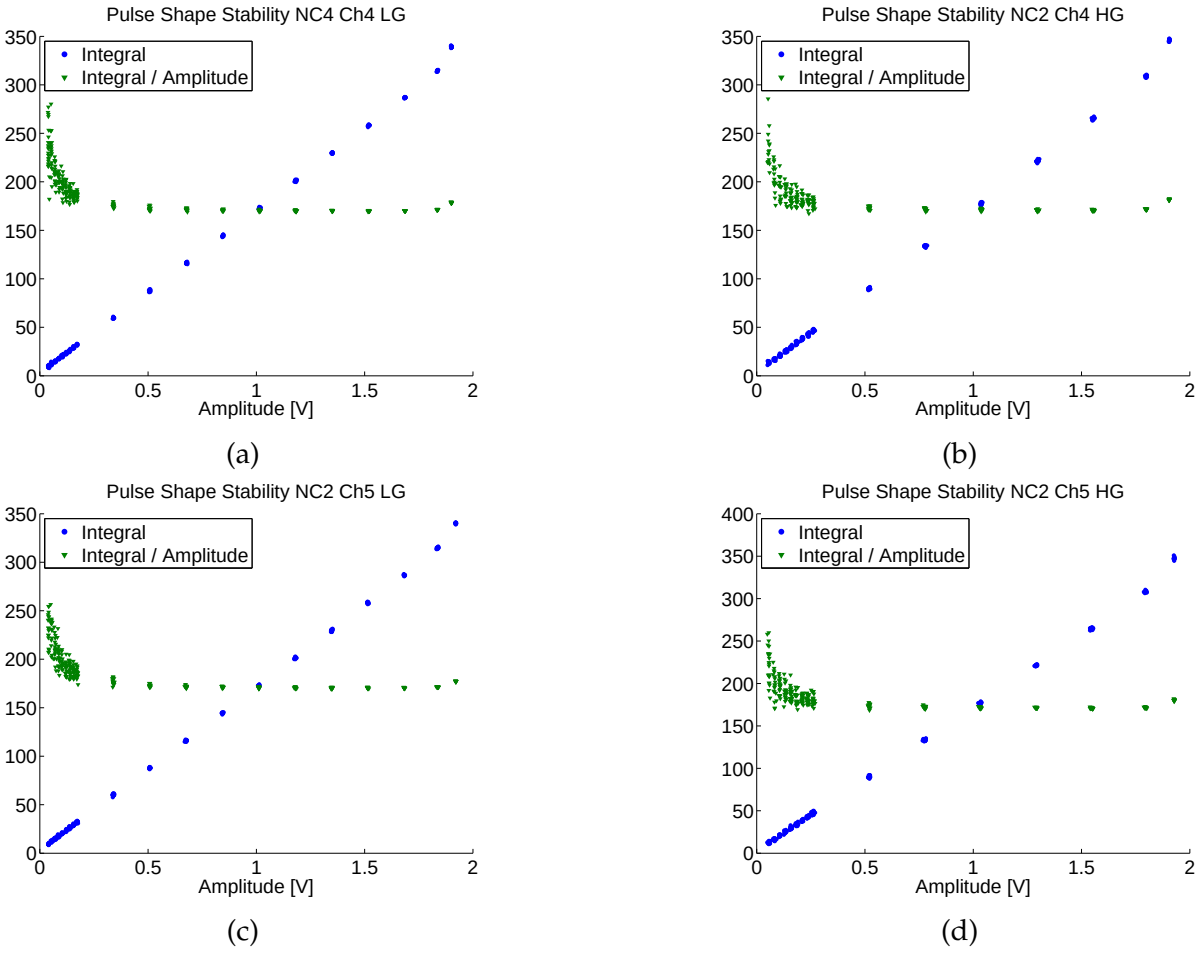

Figure A.3: Pulse shape stability measurement for NCB2 Channel 4 and 5 for low and high gain.

Appendix B

Noise in Charge-Sensitive Preamplifiers

Dr. Helmuth Spieler[17] shows how the noise in charge-sensitive preamplifiers can be calculated. The calculation takes base in an output noise voltage v_{no}, which is fed back to the input through the capacitive voltage divider between C_f and C_d, as shown in figure B.1.

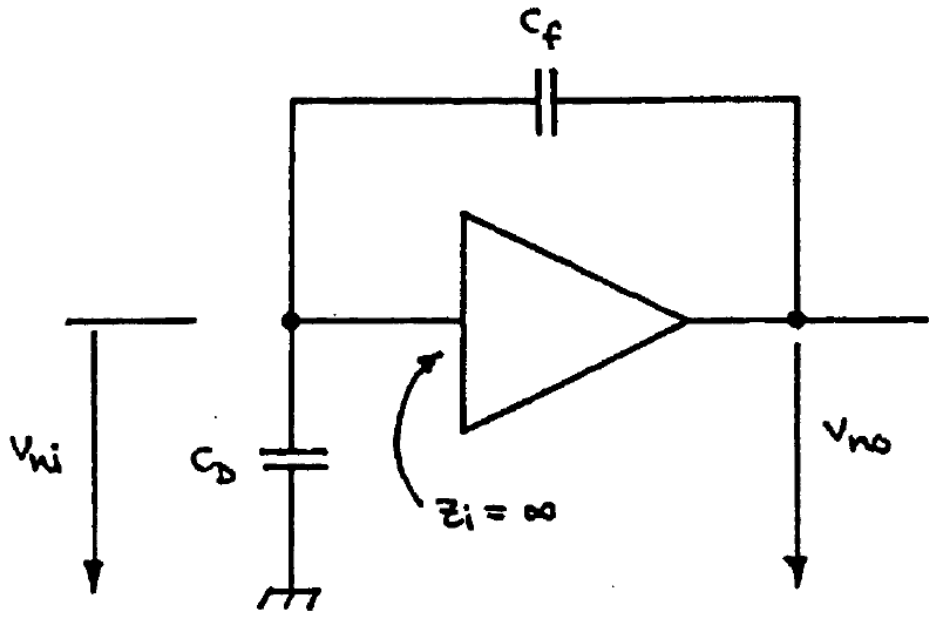

Figure B.1: A charge-sensitive amplifier.

$$v_{no} = v_{ni}\frac{X_{C_f} + X_{C_D}}{X_{C_D}} = v_{ni}\frac{\frac{1}{\omega C_f} + \frac{1}{\omega C_D}}{\frac{1}{\omega C_D}}$$
$$\Rightarrow v_{no} = v_{ni}\left(1 + \frac{C_D}{C_f}\right) \tag{B.1}$$

The equivalent input noise charge Q_{ni}, is given by equation B.2

$$Q_{ni} = \frac{v_{no}}{A_Q} = v_{no}C_f, \tag{B.2}$$

where A_Q is the gain of the charge-sensitive amplifier. Inserting equation B.1 into equation B.2 gives a new expression for the equivalent noise charge, shown in equation B.3.

$$Q_{ni} = v_{ni}\left(C_D + C_f\right) \tag{B.3}$$

The signal-to-noise ratio is given by equation B.4

$$\frac{Q_s}{Q_{ni}} = \frac{Q_s}{v_{ni}\left(C_D + C_f\right)} = \frac{1}{C}\frac{Q_s}{v_{ni}}, \tag{B.4}$$

where Q_s is the signal charge and $C = C_D + C_f$. As can be seen from the equation the noise grows with increasing C.

Appendix C

DAQ Settings for the Discrete Component Preamplifier

The data acquisition settings used for the discrete component preamplifier while measuring the Fe-55 pulse height distribution shown in figure 4.17a. The preamplifier is non-inverting and outputs negative pulses when connected to the GEM detector (since the collected charge is negative). The pulse height distribution is shown in the window labeled ”Histogram”.

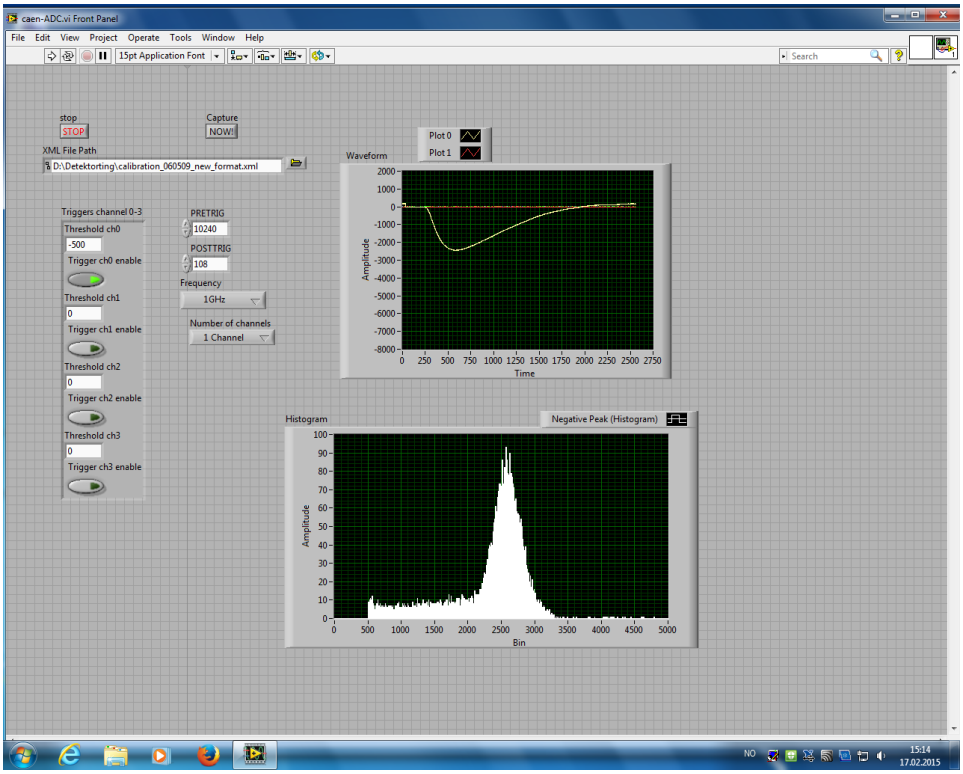

Figure C.1: The DAQ setup used for the discrete component preamplifier.

Appendix D

Crosstalk Results

During the crosstalk test it was discovered that channel 1 on all the carrier boards was malfunctioning. When applying the input signal to channel 1, the crosstalk values at all other channels skyrocketed compared to when the signal was injected in any other channel. This was not, however, reciprocal - when the signal was injected to any of the other channels (2-5), the crosstalk values at channel 1 were quite low and often barely above noise levels. This phenomenon is illustrated in figure D.1 for NCB2 at low gain. The crosstalk was quite significant (73.3 mV) in channel 2 when the signal was injected into channel 1 (D.1a), but only roughly one third as high (21.6 mV) in the opposite case (D.1b).

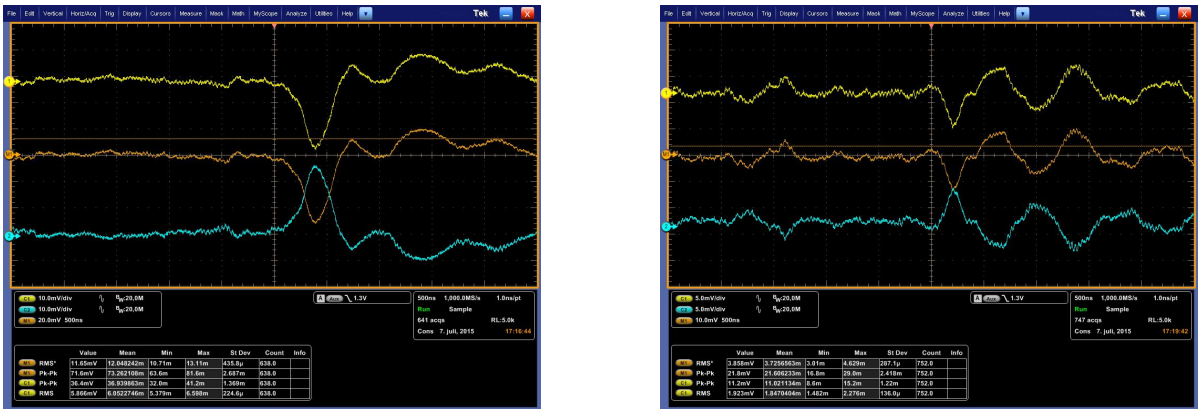

(a) (b)

Figure D.1: a) Channel 2 of NCB2 at low gain. The input signal is injected into channel 1. b) Channel 1 of NCB2 at low gain. The input signal is injected into channel 2. In the former case the crosstalk is quite significant, while it is only one third as great in the latter.

The measured crosstalk values in millivolts are shown for OCB1 and OCB2 in table D.1 and for NCB1 and NCB2 in table D.2. The measured peak-to-peak noise for each channel is also included. The input signal is injected into the channels of the first column, and the output of the channels is subsequently read out in columns 2 through

6. The crosstalk when the signal is injected into channel 1 is very high compared to the other channels, therefore these values were omitted from the results (see section 4.1.3).

OCB1 LG [mV]					
	Ch 1	Ch 2	Ch 3	Ch 4	Ch 5
In Ch 1	1480	64.2	52.8	56.2	71.3
In Ch 2	8.7	2160	11.1	10.6	11.5
In Ch 3	6.5	10.4	2200	12.1	12.6
In Ch 4	6.3	10.9	12.1	2200	15.2
In Ch 5	6.9	10.6	10.8	11.6	2190
Noise	5.7	8.9	8.8	8.7	8.8
OCB1 HG [mV]					
	Ch 1	Ch 2	Ch 3	Ch 4	Ch 5
In Ch 1	-	151.0	108.0	120.0	125.0
In Ch 2	13.3	2200	20.0	24.2	25.4
In Ch 3	10.6	19.7	2210	31.4	27.5
In Ch 4	10.9	17.0	21.3	2200	26.4
In Ch 5	11.9	17.3	17.2	18.1	2200
Noise	8.2	13.1	12.8	13.1	13.4
OCB2 LG [mV]					
	Ch 1	Ch 2	Ch 3	Ch 4	Ch 5
In Ch 1	2180	92.3	88.5	92.3	99.5
In Ch 2	10.3	2180	12.3	11.3	12.5
In Ch 3	9.9	10.8	2160	11.2	13.1
In Ch 4	10.1	11.5	12.1	2190	15.5
In Ch 5	11.3	11.3	11.6	12.6	2160
Noise	8.8	8.9	8.5	9.0	9.2
OCB2 HG [mV]					
	Ch 1	Ch 2	Ch 3	Ch 4	Ch 5
In Ch 1	2190	148.0	142.0	152.0	156.0
In Ch 2	15.7	2200	14.8	15.0	16.4
In Ch 3	14.6	14.7	2200	17.0	15.6
In Ch 4	14.3	15.1	15.2	2220	17.6
In Ch 5	20.3	19.2	11.6	20.1	2180
Noise	13.8	13.7	13.1	13.8	14.0

Table D.1: Measured peak-to-peak amplitudes caused by crosstalk for OCB1 and OCB2, including the noise of each channel.

NCB1 LG [mV]					
	Ch 1	Ch 2	Ch 3	Ch 4	Ch 5
In Ch 1	2000	68.2	69.1	69.3	69.2
In Ch 2	10.7	2000	16.8	13.3	13.7
In Ch 3	10.8	14.1	1980	13.1	13.7
In Ch 4	10.4	12.9	14.7	2000	17.7
In Ch 5	10.7	11.2	11.5	12.6	1980
Noise	9.1	9.7	9.9	9.8	9.6
NCB1 HG [mV]					
	Ch 1	Ch 2	Ch 3	Ch 4	Ch 5
In Ch 1	2020	102.0	102.0	105.0	103.0
In Ch 2	14.1	2050	23.4	16.6	17.3
In Ch 3	13.7	17.5	2020	16.1	16.4
In Ch 4	13.9	16.4	17.8	2090	21.7
In Ch 5	17.0	16.7	16.4	16.3	2000
Noise	12.5	13.7	14.2	14.2	13.8
NCB2 LG [mV]					
	Ch 1	Ch 2	Ch 3	Ch 4	Ch 5
In Ch 1	2000	72.0	72.0	74.0	72.0
In Ch 2	21.2	1970	27.6	24.0	24.4
In Ch 3	22.6	26.5	1970	24.3	24.8
In Ch 4	20.6	22.9	23.7	1980	29.1
In Ch 5	18.5	20.4	21.2	23.5	1970
Noise	9.1	10.1	9.7	10.3	10.2
NCB2 HG [mV]					
	Ch 1	Ch 2	Ch 3	Ch 4	Ch 5
In Ch 1	2070	107.0	106.0	111.0	107.0
In Ch 2	22.7	1980	31.8	24.8	26.1
In Ch 3	24.4	32.3	2050	24.2	25.5
In Ch 4	21.2	23.7	24.2	2000	30.2
In Ch 5	18.9	21.6	20.8	24.7	1980
Noise	13.6	14.8	14.2	15.3	15.1

Table D.2: Measured peak-to-peak amplitudes caused by crosstalk for NCB1 and NCB2, including the noise of each channel.

The relative crosstalk values (in percent) are calculated using equation 4.1 and are listed in tables D.3 and D.4. Channel 1 has been omitted from all tables since it was defective.

OCB1 LG [%]				
	Out Ch 2	Out Ch 3	Out Ch 4	Out Ch 5
In Ch 2	-	0.31	0.28	0.34
In Ch 3	0.24	-	0.38	0.41
In Ch 4	0.29	0.38	-	0.56
In Ch 5	0.26	0.29	0.35	-
OCB1 HG [%]				
	Out Ch 2	Out Ch 3	Out Ch 4	Out Ch 5
In Ch 2	-	0.70	0.92	0.98
In Ch 3	0.67	-	1.29	1.09
In Ch 4	0.49	0.77	-	1.03
In Ch 5	0.51	0.52	0.57	-
OCB2 LG [%]				
	Out Ch 2	Out Ch 3	Out Ch 4	Out Ch 5
In Ch 2	-	0.41	0.31	0.39
In Ch 3	0.28	-	0.31	0.43
In Ch 4	0.33	0.39	-	0.57
In Ch 5	0.32	0.37	0.41	-
OCB2 HG [%]				
	Out Ch 2	Out Ch 3	Out Ch 4	Out Ch 5
In Ch 2	-	0.31	0.27	0.39
In Ch 3	0.24	-	0.45	0.31
In Ch 4	0.29	0.35	-	0.48
In Ch 5	0.62	0.62	0.67	-

Table D.3: Relative crosstalk for OCB1 and OCB2.

NCB1 LG [%]				
	Out Ch 2	Out Ch 3	Out Ch 4	Out Ch 5
In Ch 2	-	0.68	0.45	0.49
In Ch 3	0.52	-	0.44	0.49
In Ch 4	0.43	0.54	-	0.74
In Ch 5	0.28	0.30	0.40	-
NCB1 HG [%]				
	Out Ch 2	Out Ch 3	Out Ch 4	Out Ch 5
In Ch 2	-	0.91	0.42	0.51
In Ch 3	0.54	-	0.38	0.44
In Ch 4	0.43	0.51	-	0.80
In Ch 5	0.48	0.41	0.40	-
NCB2 LG [%]				
	Out Ch 2	Out Ch 3	Out Ch 4	Out Ch 5
In Ch 2	-	1.31	1.10	1.13
In Ch 3	1.24	-	1.12	1.15
In Ch 4	1.04	1.09	-	1.38
In Ch 5	0.90	0.96	1.07	-
NCB2 HG [%]				
	Out Ch 2	Out Ch 3	Out Ch 4	Out Ch 5
In Ch 2	-	1.44	0.99	1.08
In Ch 3	1.40	-	0.91	1.00
In Ch 4	0.93	0.98	-	1.31
In Ch 5	0.79	0.77	0.98	-

Table D.4: Relative crosstalk for NCB1 and NCB2.

The relative crosstalk results are plotted as a function of channel number in figure D.2 (a-h) for all four carrier boards at both low and high gain. The channel where the charge was injected is shown in the legend box. For example the blue circles represent the input signal being injected into channel 2 of the SAMPA chips, the green squares represent the signal being injected into channel 3, and so forth. Hence there will be only three markers of one type on each plot (e.g. three blue circles), since the fourth one represents the channel where the charge is injected.

In an ideal case with wires running in parallel next to each other, one would expect the crosstalk between the wires to decrease with the distance between them; the wires closest to the one being injected with a signal should have greater crosstalk values than the ones further away. In most of the plots, however, this trend is not visible.

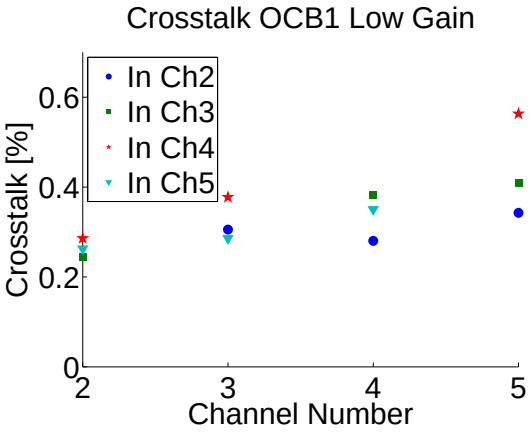
Crosstalk OCB1 Low Gain
In Ch2
In Ch3
In Ch4
In Ch5
Crosstalk [%]
Channel Number

(a)

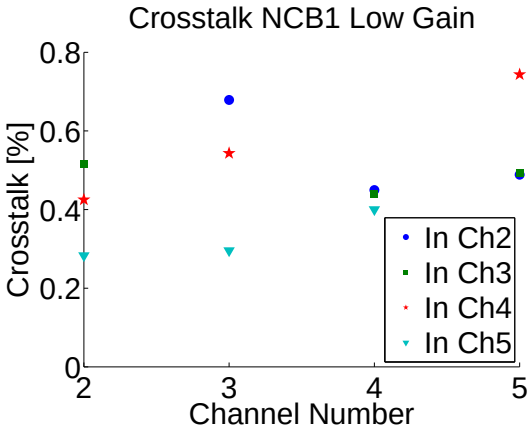
Crosstalk NCB1 Low Gain
In Ch2
In Ch3
In Ch4
In Ch5
Crosstalk [%]
Channel Number

(b)

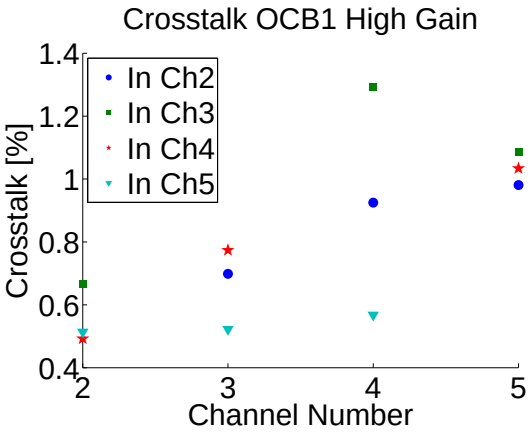
Crosstalk OCB1 High Gain
In Ch2
In Ch3
In Ch4
In Ch5
Crosstalk [%]
Channel Number

(c)

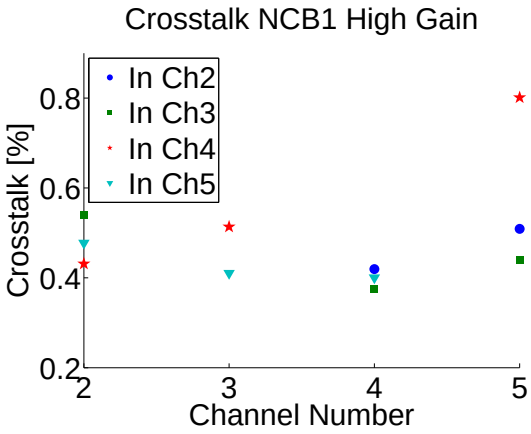
Crosstalk NCB1 High Gain
In Ch2
In Ch3
In Ch4
In Ch5
Crosstalk [%]
Channel Number

(d)

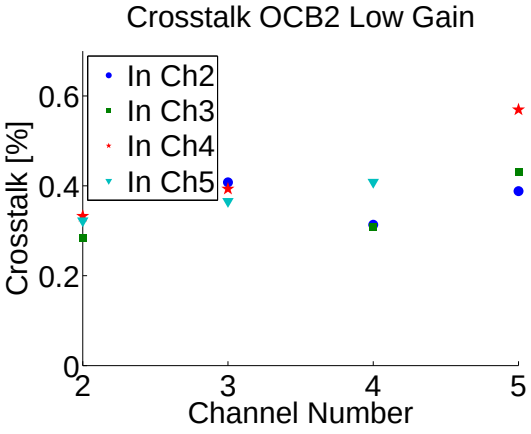
Crosstalk OCB2 Low Gain
In Ch2
In Ch3
In Ch4
In Ch5
Crosstalk [%]
Channel Number

(e)

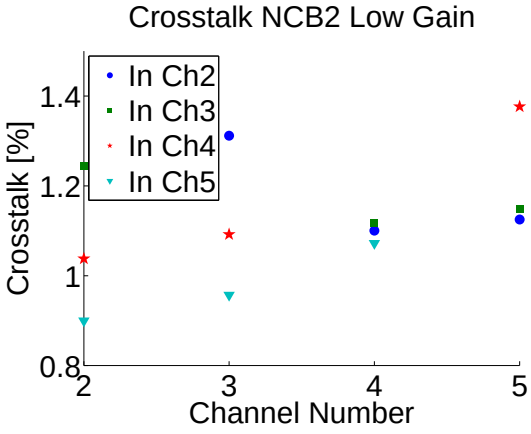
Crosstalk NCB2 Low Gain
In Ch2
In Ch3
In Ch4
In Ch5
Crosstalk [%]
Channel Number

(f)

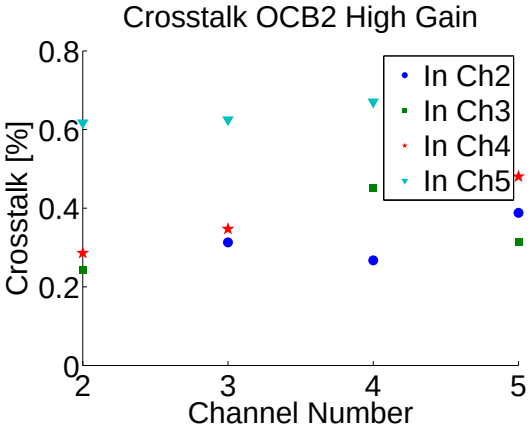
Crosstalk OCB2 High Gain
In Ch2
In Ch3
In Ch4
In Ch5
Crosstalk [%]
Channel Number

(g)

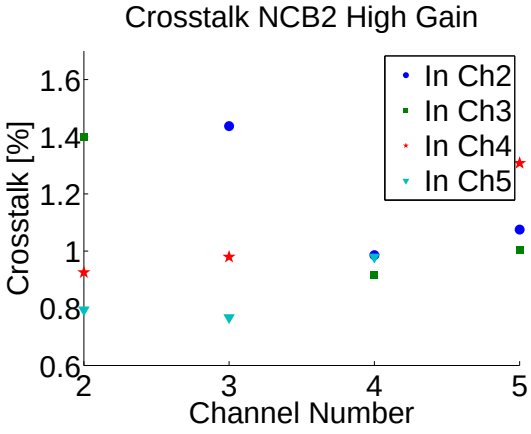
Crosstalk NCB2 High Gain
In Ch2
In Ch3
In Ch4
In Ch5
Crosstalk [%]
Channel Number

(h)

Appendix E

Schematic and PCB Design

The schematic of the new carrier board (NCB) is shown in figures E.1 through E.3. Figure E.1 shows the SAMPA Chip 1 and its accompanying components (voltage reference, jumpers, etc.). Figure E.2 is the differential buffer, the decoupling capacitors and the jumpers to select which channel of the SAMPA Chip 1 goes through the buffer. Figure E.3 illustrates how the voltage references (V450, V600 and V750) are obtained using buffers and voltage dividers.

The PCB layout is shown in figure E.4. Red wires run on top of the PCB while the blue ones run on the bottom.

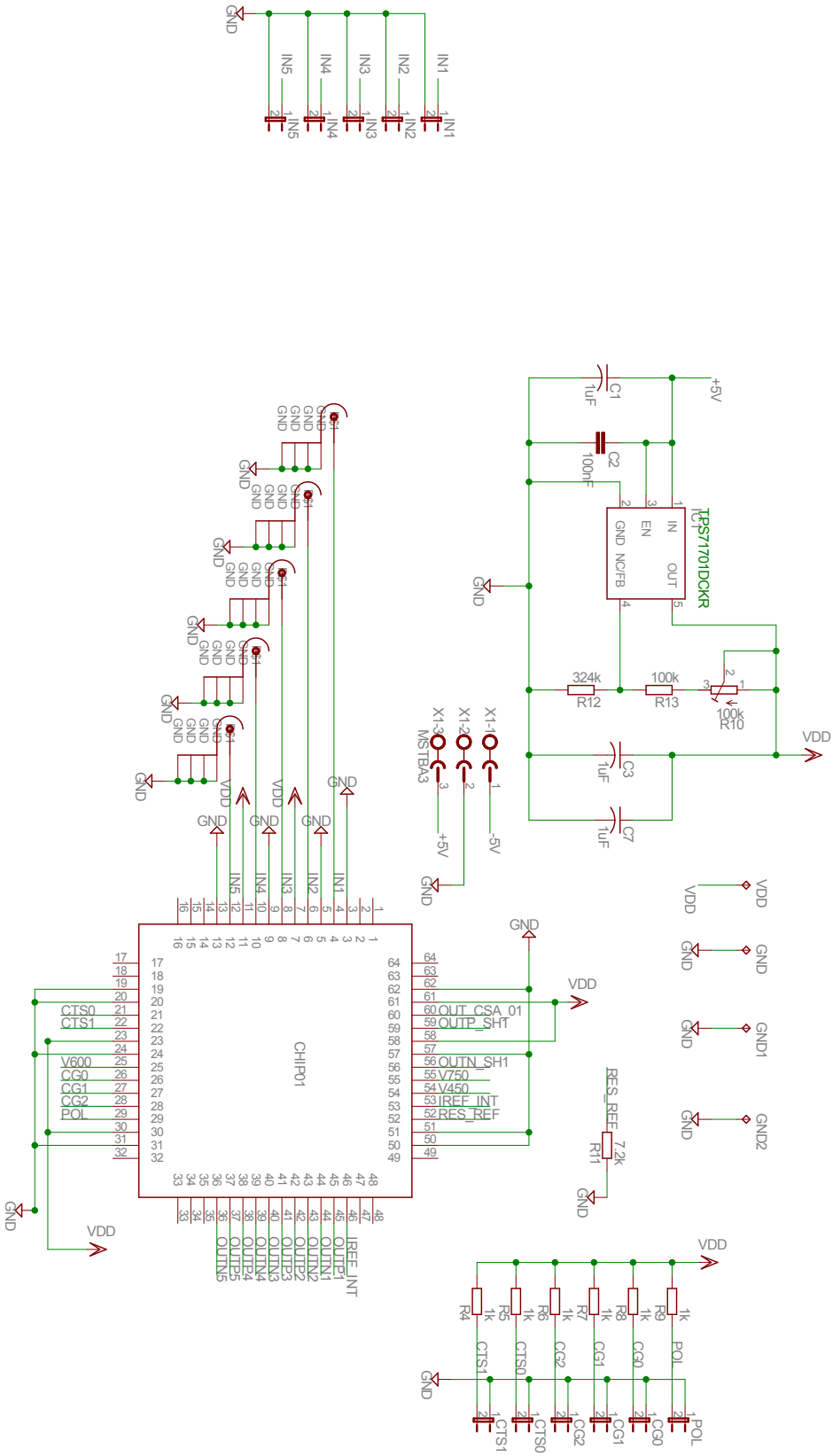

Figure E.1: The schematic of the new carrier board (1 of 3).

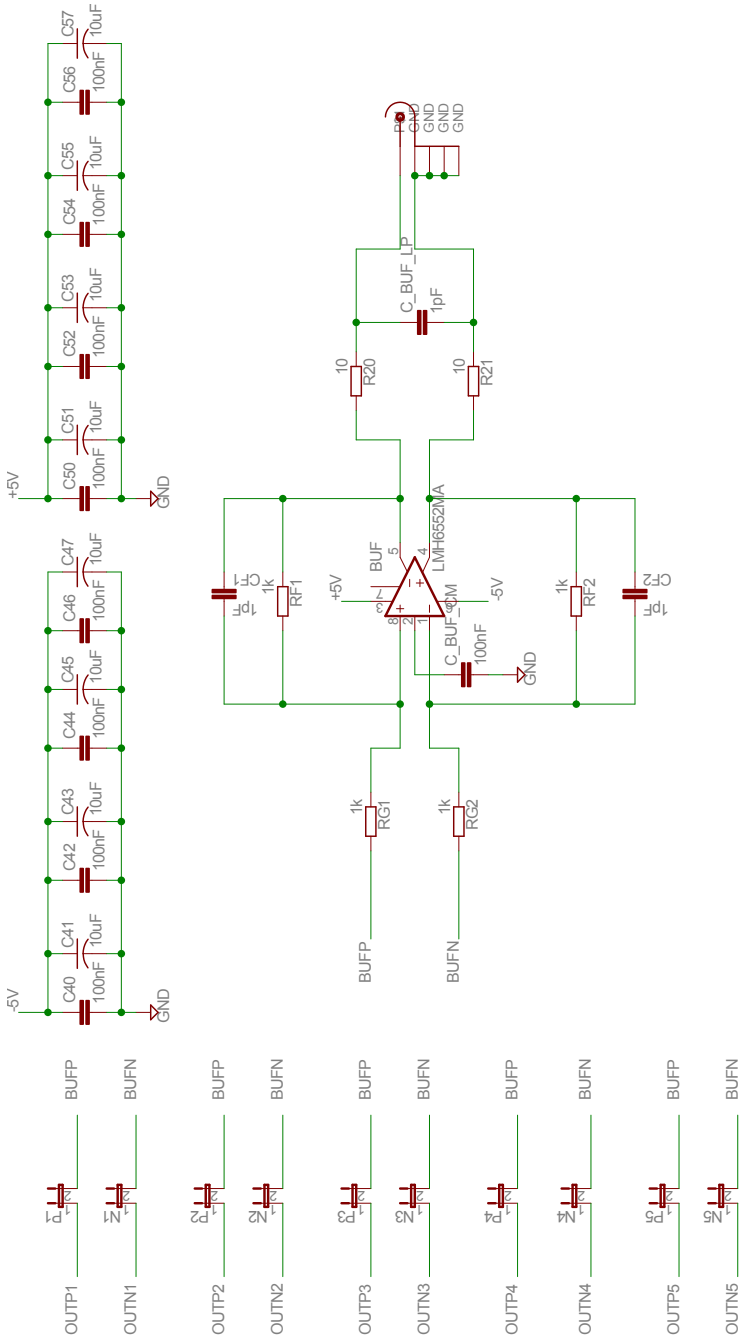

Figure E.2: The schematic of the new carrier board (2 of 3).

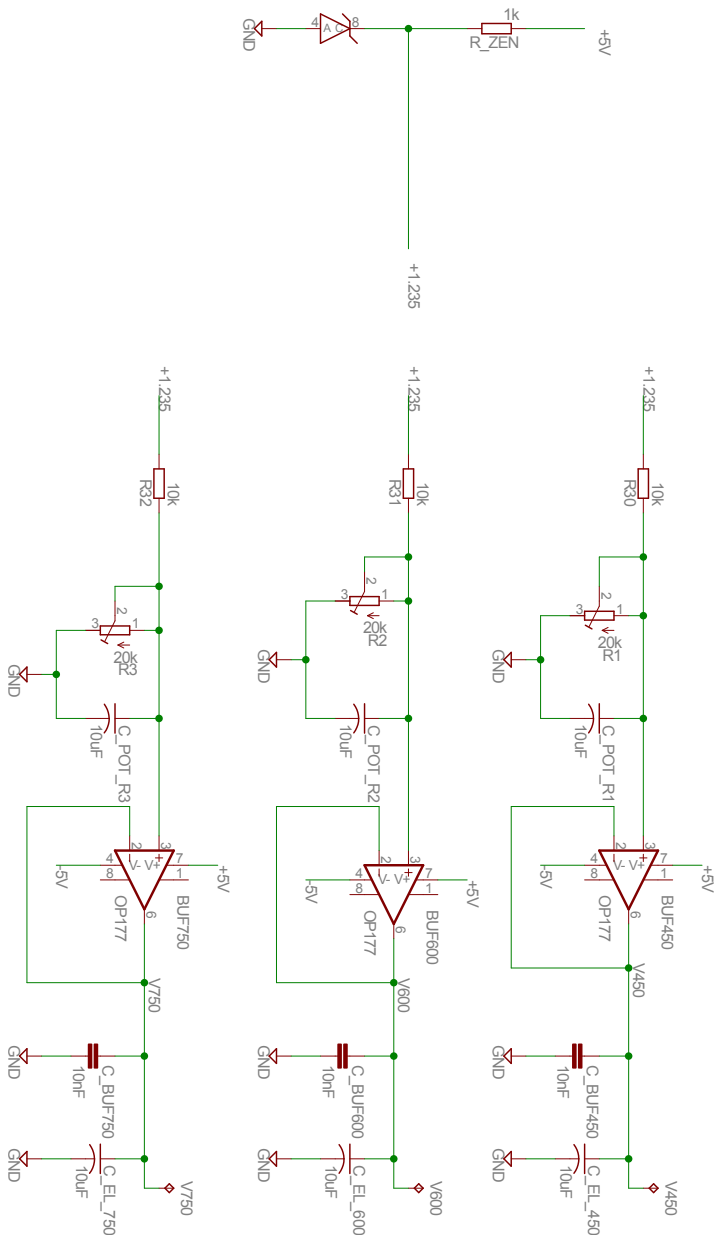

Figure E.3: The schematic of the new carrier board (3 of 3).

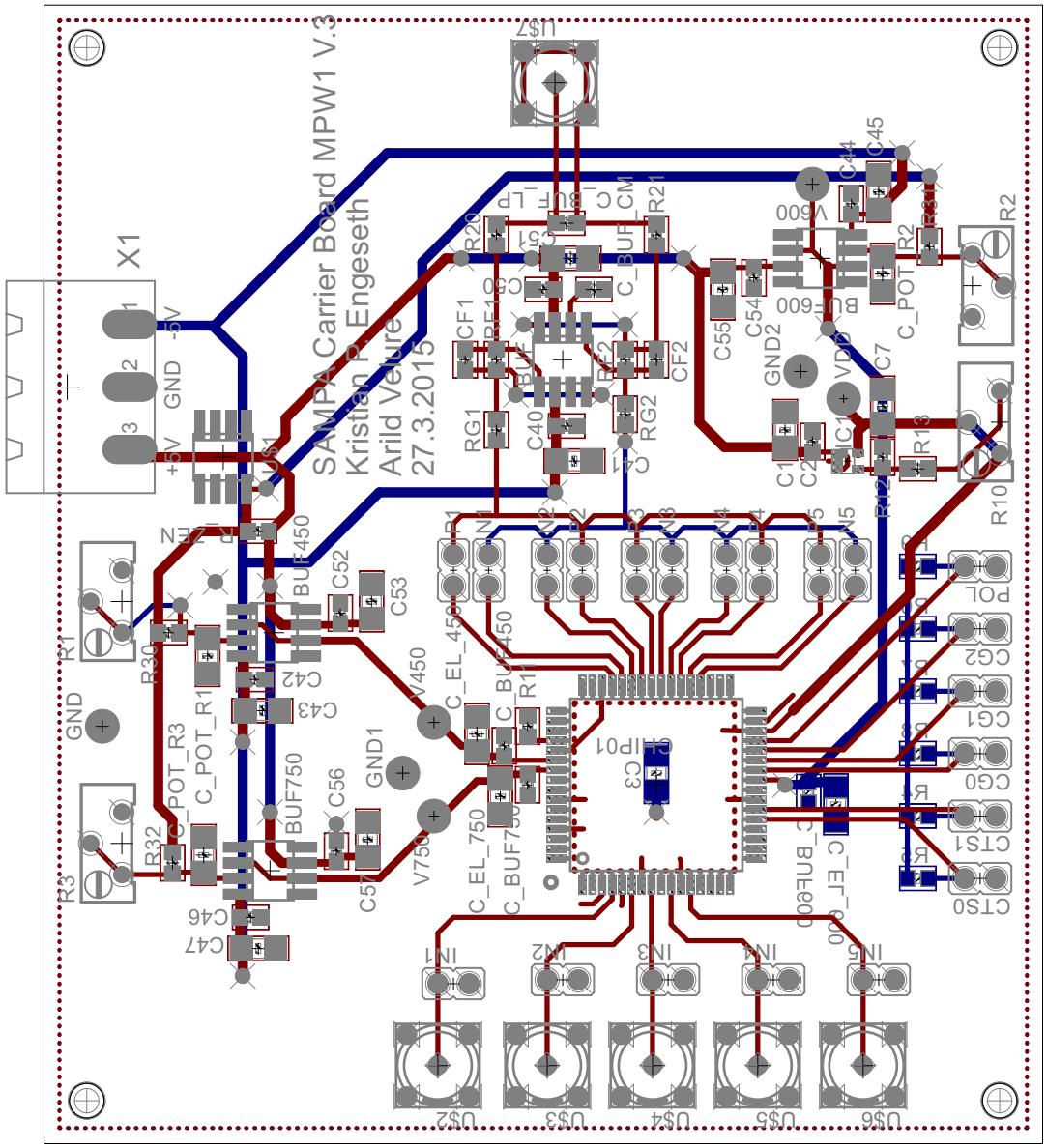

Figure E.4: The PCB layout of the new carrier board.

Appendix F

Number of Primary Ionizations in Ne-CO_2-N_2 (90-10-5)

In the ALICE TPC upgrade a mixture of Ne-CO_2-N_2 will be used. To find the ionization energy the ratios of the gases used have to be known. The ratios of the gases in Ne-CO_2-N_2 (90-10-5) don't add up to 100 %, so the correct ratios have to be calculated. The prerequisite for doing this calculation is knowing what the notation (90-10-5) means. It means that 5 % of N_2 is added to a (90-10) mixture of Ne-CO_2. The calculation to find the correct gas ratios is done in equation F.1.

$$\begin{aligned} & 0.95 * 0.90 + 0.95 * 0.10 + 0.05 \\ & = 0.855 + 0.095 + 0.05 \\ & \rightarrow (85.5 - 9.5 - 5) \end{aligned} \tag{F.1}$$

Gas	Ionization energy [eV]
Argon	26
CO_2	33
N_2	35
Ne	36

Table F.1: Ionization energies for a few gases [13].

The ionization energies for a few gases commonly used in gas detectors are listed in table F.1. Together with the correct gas ratios obtained above (85.5 - 9.5 - 5), these energies are used to calculate the ionization energy, as shown in equation F.2.

$$E_{Ionization} = (0.855 * 36 + 0.095 * 33 + 0.05 * 35)\ eV = 35.67\ eV \tag{F.2}$$

To find the number of primary ionizations in the gas, the energy of the incoming particles is needed. For Fe-55 the photon energy is 5.9 keV, and the calculation for

obtaining the number of primary ionizations is shown in equation F.3.

$$N_{Prim} = \frac{E_{Particle}}{E_{Ionization}} = \frac{5.9\ keV}{35.67\ eV} \approx 165 \tag{F.3}$$

Appendix G

Pulse Area Calculation

The procedure for obtaining the pulse amplitude and integral for a 40 mV and a 400 mV output signal is shown in figures G.1 and G.2, respectively. The 40 mV output signal shows a lot of noise and its integral isn't very well defined because of the noise fluctuations. The 400 mV output signal (figure G.2) shows very clear amplitude and integral values, since the noise is low compared to the signal. The noise dominance at low signal amplitudes results in the broadening of the bunch sizes in figure 4.7 in section 4.1.2.

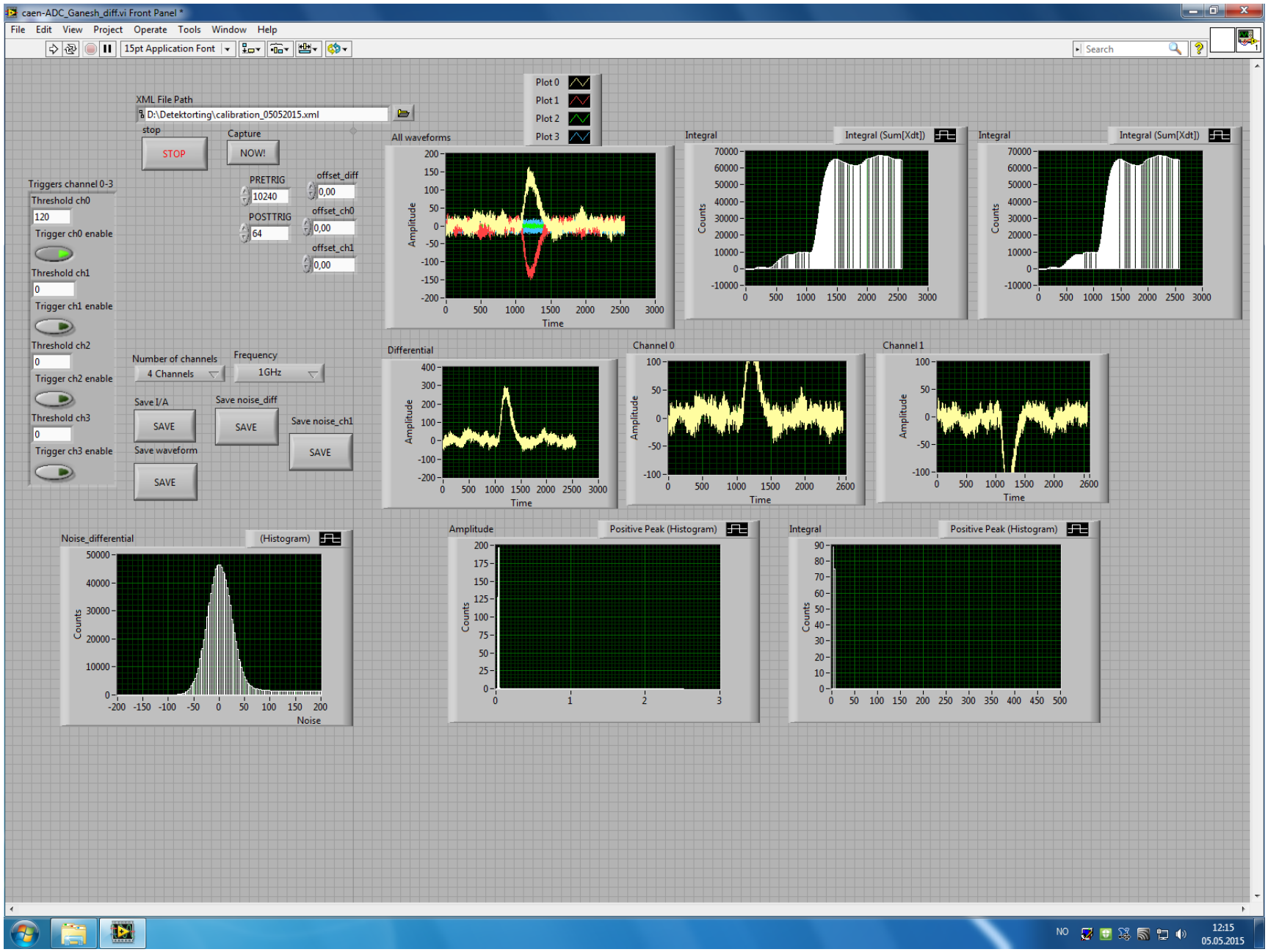

Figure G.1: A LabView setup screenshot of a 40 mV output signal.

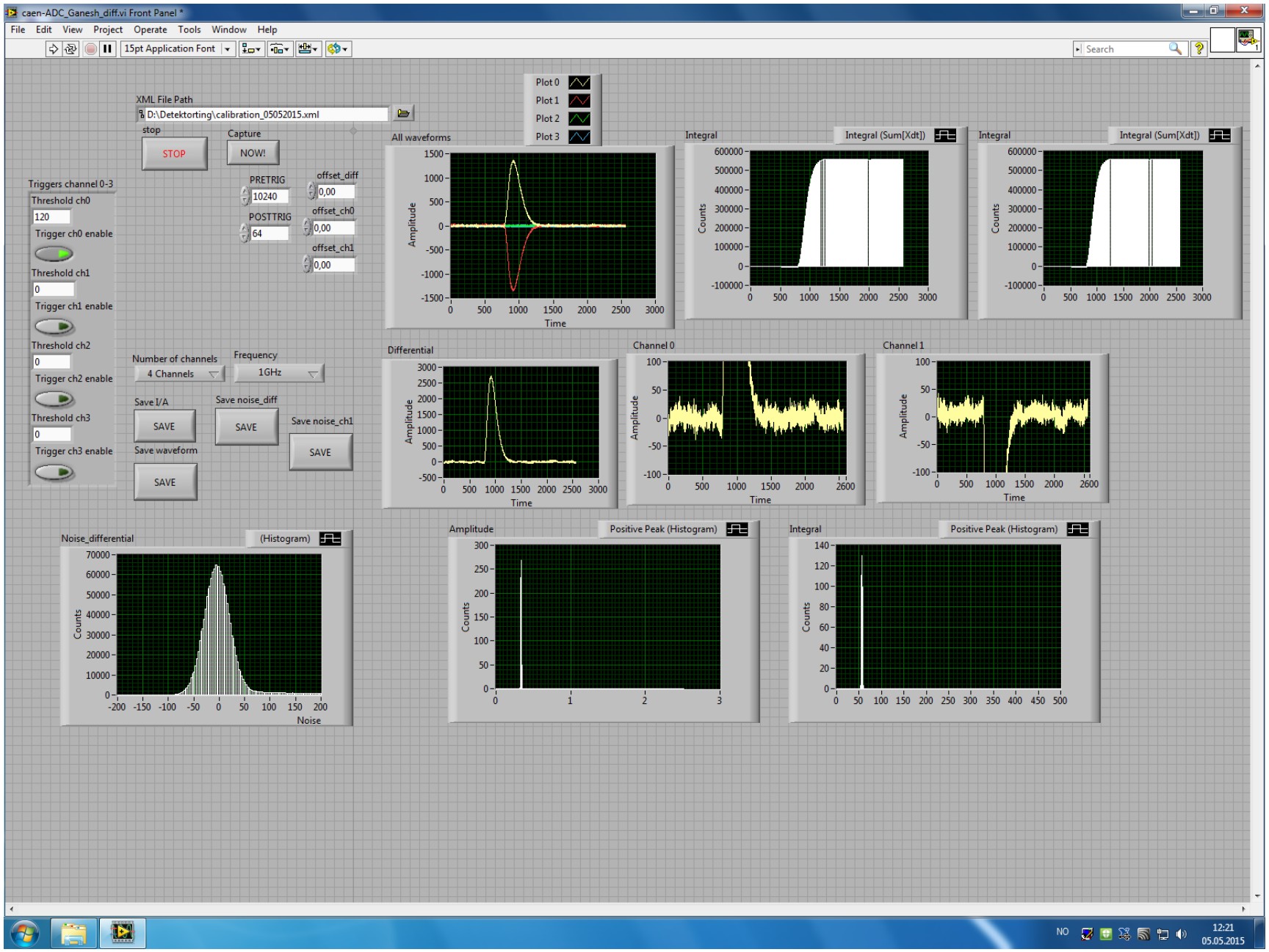

Figure G.2: A LabView setup screenshot of a 400 mV output signal.

Bibliography

[1] Fig: Alice. http://aliceinfo.cern.ch/Public/Objects/Chapter2/DetectorComponents/alice2.jpg.

[2] Fig: Bethe-bloch. http://physik.wikia.com/wiki/Datei:Bethe.jpg.

[3] Fig: Discharge probability. https://gdd.web.cern.ch/GDD/gemperformances.html.

[4] Fig: Lhc. http://www.atlas.ch/photos/atlas_photos/selected-photos/detector-site/surface/9906026-A4-at-144-dpi.jpg.

[5] Fig: Photoelectric effect. http://www.laradioactivite.com/en/site/pages/PhotoElectric_Effect.htm.

[6] Fluke accuracy. https://www.atecorp.com/ATECorp/media/pdfs/data-sheets/Fluke-87V_Specs.pdf.

[7] Labview. http://norway.ni.com/labview.

[8] Review of particle physics. *Chinese Physics C*, 38(9):1676, 2014.

[9] Fig: Big bang. http://www.particleadventure.org/images/history-universe-2013.jpg, 2015.

[10] The ALICE Collaboration. Technical design report for the upgrade of the ALICE read-out and trigger system. 2014.

[11] The ALICE Collaboration. Technical design report for the upgrade of the ALICE time projection chamber. 2014.

[12] Hege Austrheim Erdal. *D0-electron correlation in pp collisions at center of mass energy 7 TeV*. PhD thesis, University of Bergen, 2014. ISBN 978-82-308-2874-8.

[13] F. Sauli. Principles of operation of multiwire proportional and drift chambers. 1977.

[14] F. Sauli. GEM a new concept for electron amplification in gas detectors. *Nuclear Instruments and Methods in Physics Research Section A: Accelerators, Spectrometers, Detectors and Associated Equipment*, 386(2-3):531 – 534, 1997.

[15] Fabio Sauli. Gas Electron Multiplier Detectors: Performances and Applications. 2006.

[16] Frank Simon. Commissioning of the GEM detectors in the COMPASS experiment. 2001.

[17] Dr. Helmuth Spieler. Silicon detectors: Basic concepts ii. 1998.